High Bit-rate Digital Communication through Metal Channels

A Thesis

Submitted to the Faculty

of

Drexel University

by

Richard A Primerano

in partial fulfillment of the

requirements for the degree

of

Doctor of Philosophy

July 2010

Table of Contents

List of Figures

List of Tables

List of Acronyms

A/D analog-to-digital converter

D/A digital-to-analog converter

DFE decision feedback equalizer

DSP digital signal processor

FIR finite impulse response

IIR infinite impulse response

ISI intersymbol interference

MAC multiply-accumulate

NDT non-destructive testing

PAM pulse amplitude modulation

RC raised-cosine

RRCF root raised-cosine filter

SNR signal-to-noise ratio

TDOA time difference of arrival

TTBR through the bulkhead repeater

Abstract

High Bit-rate Digital Communication through Metal Channels

Richard A Primerano

Advisor: Moshe Kam, Ph.D.

The need to transmit digital information across metallic barriers arises frequently in industrial control applications. In some applications, the barrier can be penetrated with wiring, while in others this may not be possible. For example, metal bulkheads, pressure vessels, or pipelines may require a level of mechanical integrity that prohibits mechanical penetration. This study investigates the use of ultrasonic signaling for data transmission across metallic barriers, discusses the associated challenges, and analyzes several alternative communication system implementations.

Several recent efforts have been made to develop through-metal ultrasonic communication systems, with approaches ranging widely in bitrate, complexity, and power requirements. The transceiver designs presented here are intended to cover a range of target applications. In systems having low data rate requirements, simple transceivers with low hardware/software complexity can be used. At high data rates, however, severe echoing in the ultrasonic channel leads to intersymbol interference. Reliable high speed communication therefore requires the use of channel equalizers, and results in a transceiver with higher hardware/software complexity.

In this thesis, issues related to the design of reliable through-metal ultrasonic communication systems are discussed. These include (1) the development of mathematical models used to characterize the channel, (2) application of equalization techniques needed to achieve high-speed communication, and (3) analysis of hardware/software complexity for alternative transceiver designs.

Several groups have developed through-metal ultrasonic communication systems in the recent past, though none has produced a mathematical model that accurately

describes the phenomena found within the channel. The channel model developed in this thesis can be used at several stages of the transceiver design process, from transducer selection through channel equalizer design and ultimately system performance simulation.

Using this channel model, we go on to develop and test several ultrasonic through-metal transceiver designs. Ultrasonic through-metal communication systems are finding use in a wide variety of applications. Some require high throughput, while others require low power consumption. The motivation for developing several designs – ranging from low complexity, low power to high complexity, high throughput – is so that the best design can be matched to each application.

After these transceiver designs are developed, we present an analysis of their computational requirements so that the most appropriate transceiver can be chosen for a given application.

1. Introduction

The need to transmit digital information across metallic barriers arises frequently in industrial control applications. For example, radio frequency sensing and control networks deployed on naval vessels must maintain connectivity across multiple watertight bulkheads [1,2]. Since radio signals can not pass through the metal bulkhead, an alternate method is needed to move data across it. Because the bulkhead is designed to be watertight, penetrating it to install wires or cables is undesirable.

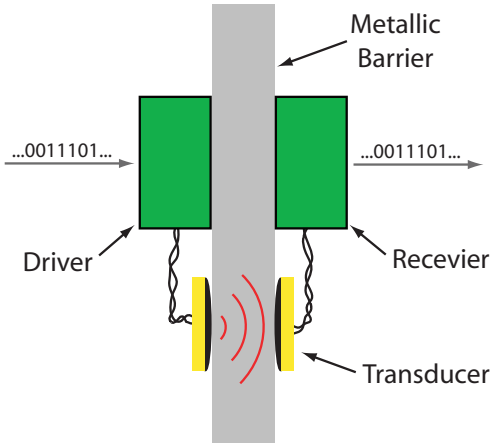

Figure 1.1: Ultrasonic through-metal transceiver

The use of ultrasonic signaling to transmit digital information across metallic barriers has been demonstrated by several groups [3–7]. Figure 1.1 illustrates the concept of a *through-metal ultrasonic transceiver*, which is at the core of most existing efforts. Data entering a *driver* on the transmitting side of the system (left side of the barrier) is encoded and used to drive a transmitting transducer transducer that sends ultrasonic energy into the metallic barrier. The energy that reaches the

receiving transducer (right side of the barrier) is amplified by a *receiver* and from it, the transmitted data sequence is recovered. In this thesis, issues related to the design of reliable through-metal ultrasonic communication systems are discussed. These include (1) the development of mathematical models used to characterize the channel, (2) application of equalization techniques needed to achieve high-speed communication, and (3) analysis of hardware/software complexity for alternative transceiver designs.

This work originated as a means of providing connectivity to radio frequency control networks on naval vessels, where ultrasonic through-metal transceivers would ensure reliable communication across water tight (and RF shielding) bulkheads. Additional applications of this technology include data transmission through pressure vessels, pipe walls, and cargo containers. Recently, several efforts have been made to transmit both data *and power* through metal using ultrasonic energy, allowing on side of the transceiver to operate without battery power [8–10]. NASA has shown interest in using this technology to monitor the contents of a sealed sample transport container in its upcoming *Mars Sample Return Mission* [10]. As expected, in these applications, low power consumption (and therefor low hardware/software complexity) is important. In the remainder of this thesis, several ultrasonic transceiver designs are presented that range in complexity and achievable data rate. In general, the designs exhibiting lower complexity are best for low power, low data rate applications. Higher complexity designs can support higher data rates at the expense of increased power consumption. While this thesis does not address wireless power transmission, it does develop the low complexity (low power consumption) transceiver designs that are needed in such "batteryless" designs.

1.1 Objectives

This work provides a suite of digital communication algorithms, along with a hardware testbed, that defines the tradeoffs between hardware/software complexity and data rate in ultrasonic through-metal communication systems. The main components are:

End-to-end Channel Model The through-metal communication system consists of an interconnection of electrical and acoustic components. To understand the behavior of the system, these components have been individually modeled, and used to form an end-to-end channel simulation. These models and simulation results are useful in assessing the impact of transducer-barrier material mismatch and barrier thickness variations, as well as determining the effect of different pulse shaping filters and channel equalizers.

Application of Equalization Techniques Numerous channel equalization techniques have been developed for use in telecommunications applications. These include linear equalizers based on transversal filters [11], and nonlinear equalizers such as the decision feedback equalizer [12]. Furthermore, these equalizers can be made adaptive to cope with time-varying channel conditions [13]. One of the key differences between the ultrasonic channel and most other telecommunications channels is that the interference present in the through-metal channel is well structured – a function of the bulkhead's material properties and dimensions. These properties of the ultrasonic channel can be exploited to reduce equalizer complexity.

In addition to the commonly encountered equalization techniques, we present an equalizer design method that uses a single training pulse to construct a model of the ultrasonic channel, then uses that model to directly build an equalizing filter. We show that in some applications this approach provides a low complexity solution

whose performance is equivalent to that of more complex, existing techniques.

Transceiver Complexity Analysis At the conclusion of this study, a summary of relevant transceiver designs is presented, including details regarding the computational and hardware requirements of each solution. Since the through-metal communication techniques presented here may be deployed in a variety of applications with differing throughput, cost, and power constraints, this analysis of throughput verses transceiver complexity can help designers of through-metal communication systems.

1.2 Organization

This thesis is organized into seven chapters discussing the state-of-the-art in ultrasonic data communication, ultrasonic channel model development, transceiver design, and hardware implementation issues. Chapters 2 through 7 provide the following information.

Chapter 2. Motivating Example An example application of the ultrasonic through-metal transceiver is given, and an experimental laboratory test setup is described. Experimental data gathered in the laboratory demonstrates the interference issues present in the through-metal channel, and shows the origin of this interference. Channel characteristics including signal-to-noise ratio (SNR) and bandwidth place bounds on the channel's achievable data rate.

Chapter 3. Review of Related Technologies Several past efforts toward the development of through-metal ultrasonic communication systems are reviewed. Additional topics related to ultrasonic communication system modeling and design are reviewed as well. These include ultrasonic non-destructive testing and telecommunications channel equalizer design. This chapter summarizes the related technologies,

indicating how they apply the the present problem.

Chapter 4. Ultrasonic System Model A complete mathematical model of the ultrasonic communication channel is developed. Variations in transducer bandwidth, bulkhead thickness and makeup, and driving pulse shape can all be assessed through a simulation of this model. The model is used in subsequent chapters to determine the performance of different transceiver designs.

Chapter 5. Basic Transceiver Designs Ultrasonic transceivers designed for low speed applications are presented. The echo characteristics of the channel are analyzed and an upper bound is placed on the intersymbol interference caused by echoes. Using these results, a pulse-amplitude modulated (PAM) transceiver is designed and its maximum achievable bitrate is determined.

Chapter 6. Advanced Transceiver Designs At high bitrates, equalization is needed to combat intersymbol interference in the ultrasonic channel. In this chapter, several equalizer structures are developed and applied. Adaptive filtering techniques are implemented so that the equalizer can cope with time-varying channel characteristics.

Chapter 7. Transceiver Hardware Implementation The transceiver designs presented in prior chapters are compared in terms of hardware/software complexity and achievable data rate. Based on throughput and power consumption requirements of a particular application, the most appropriate transceiver design can be chosen.

2. Motivating Example

In recent years, the US Navy has expressed interest in deploying wireless sensing and control networks on their vessels [14, 15]. These networks promise to decrease the installation cost of machinery on ships while increasing survivability. The main issue that has limited the use of wireless networks in the naval setting is their reliability, namely, the difficulty in achieving reliable radio coverage throughout the vessel. In this chapter, the use of *ultrasonic through-metal transceivers* is introduced as a means of augmenting radio frequency wireless networks to increase their reliability. Using a laboratory ultrasonic through-metal channel testbed, experimental results are provided that illustrate the issues encountered in ultrasonic transceiver design.

2.1 On-Ship Wireless Communication

Figure 2.1 shows an example of a wireless temperature control system, consisting of a controller, sensors, and actuators distributed across three RF isolated compartments. In this closed-loop system, it is desired to keep the temperature of the water exiting the heat exchanger constant. To accomplish this goal, a process controller

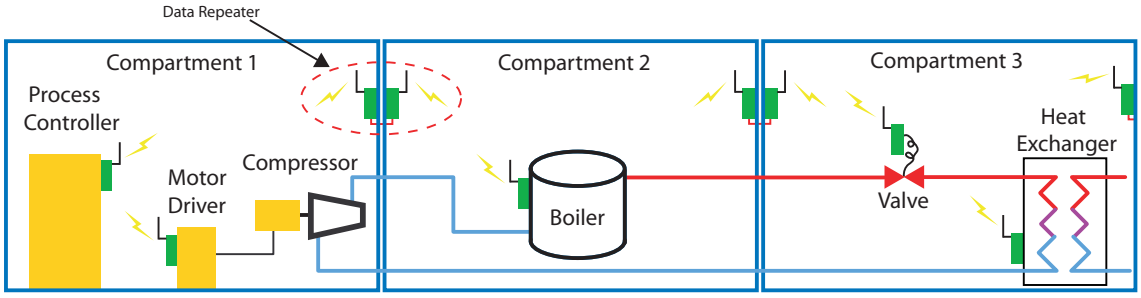

Figure 2.1: A wireless sensing network spanning multiple RF isolated compartments

reads the water temperature at the output of the heat exchanger and actuates the control valve as needed. Each of these components communicates with other devices *within* its compartments using radio frequency transceivers. Since the compartments themselves are electromagnetically isolated from one another, a method of moving data *across* them – to and from the process controller – is needed.

The *through the bulkhead repeater (TTBR)*, shown in Figure 2.2, provides a bridge between two wireless networks separated by an RF isolating bulkhead by passing data ultrasonically across the bulkhead. This system requires no mechanical penetration of the barrier.

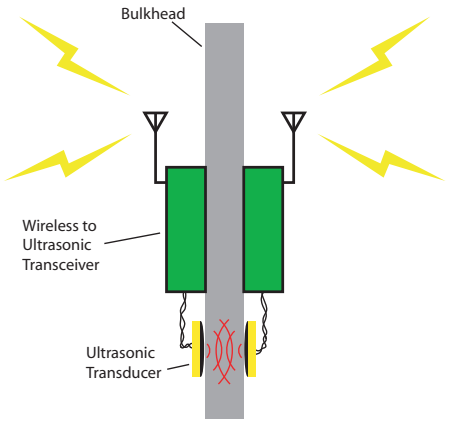

Figure 2.2: Through metal data repeater

Figure 2.3 shows the experimental setup used to study the through-metal ultrasonic channel. It consists of two 6 MHz, 0.25 inch contact transducers[1] separated by a 0.25 inch thick steel plate. Between each of the transducers and the metal plate is a layer of couplant gel[2] designed to maximize the acoustic power transfer between the two components. In this setup, the transmitting transducer is connected to a func-

[1]Panametrics NDT A112s non-destructive testing contact transducer [16, 17].
[2]Panametrics NDT D-12 gel type Couplant D.

tion generator and the receiving transducer is connected to an oscilloscope. Signal generation and analysis are performed in MATLAB®.

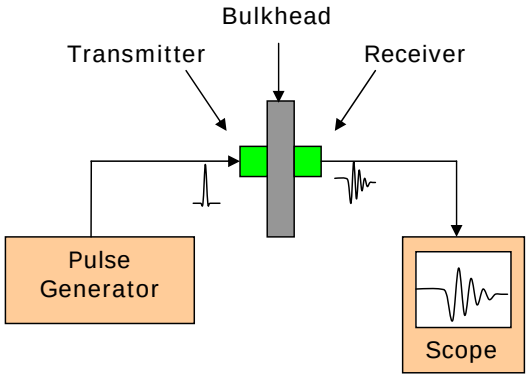

Figure 2.3: Experimental setup demonstrating echoing in ultrasonic channel

The simplest method of transmitting data through the metal channel is by pulse amplitude modulation (PAM) [18], where baseband symbols are encoded into pulses of varying amplitude. The top plot of Figure 2.4 shows a 5 volt pulse used to excite the transmitting transducer during testing. This pulse represents one data symbol being sent through the channel. The bottom plot of Figure 2.4 shows the signal at the receiving transducer. It consists of a *primary received pulse* (Primary RX) followed by a series of *echo* pulses. The primary received pulse corresponds to the transmitted data symbol, and the echoes may cause intersymbol interference (ISI) with subsequent transmissions. At low symbol rates (tens of kilosymbols/second), the echoes from successive symbols decay sufficiently fast so that ISI is not a concern. As symbol rate increases (and pulses become more closely spaced), the echoes from neighboring pulses cause ISI, which if uncorrected, may lead to symbol errors.

Under the assumption that the channel is linear and that the echoes in Figure 2.4

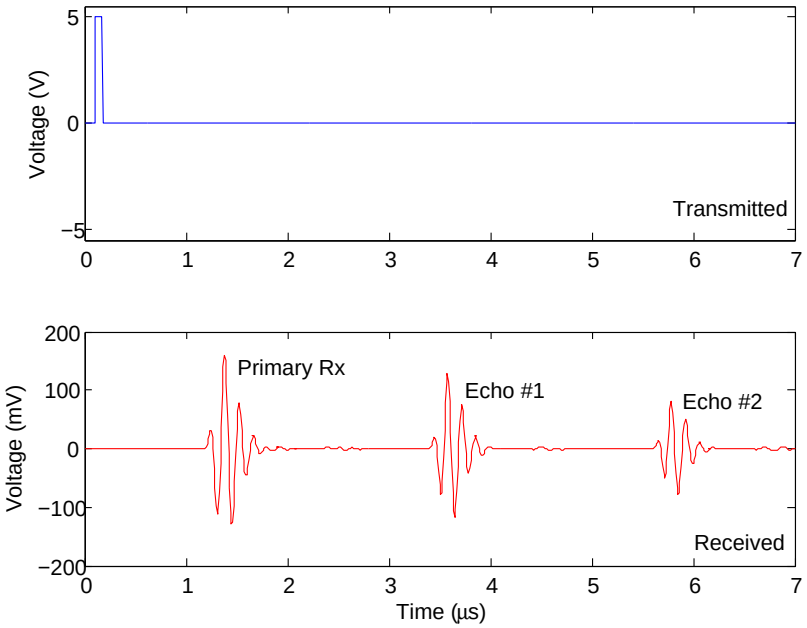

Figure 2.4: Initial investigation of channel behavior. a) Excitation of channel by single pulse. b) Response showing primary response and echoes

are time shifted, amplitude scaled versions of the primary received pulse, introducing a *cancelation pulse* with corresponding time shift and amplitude scale should cause complete suppression of echoes. Figure 2.5 shows the result of using this approach. The echo amplitude is now about 4.5 dB below its original level, approximately 10 dB below the primary. Residual echo energy remains because the amplitude response and group delay of the channel are not flat.

2.2 Channel Echoes

We hypothesize that echoes observed in the ultrasonic channel's transient response are due to two effects. The first is *impedance mismatch* between the transducer and bulkhead. As the impedance mismatch increases, the reflection coefficient magnitude at the junction between the transducer and bulkhead also increases. Figure 2.6(a) illustrates a rough contacting surface between the transducer and bulkhead,

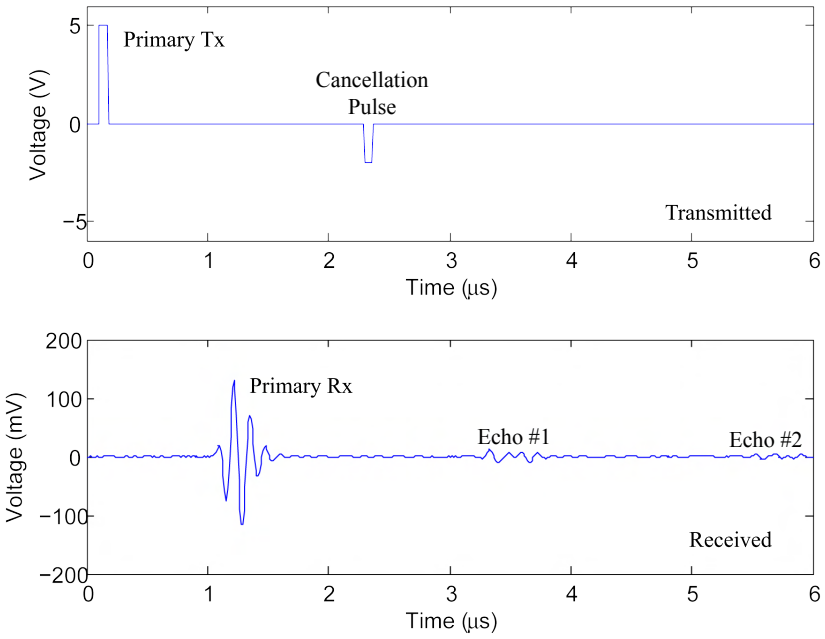

Figure 2.5: Partial suppression of echoes by *echo cancelation*. a) "Basic" excitation signal. b) Resulting output with echoes still visible.

and the reflection coefficient (Γ) looking into the bulkhead. The second effect that contributes to channel echoes is *diffraction* of the acoustic pulse as it passes from the transducer to the bulkhead. The diffractive effect means that even a perfectly matched transducer-bulkhead system will exhibit echoing. Figure 2.6(b) illustrates the diffraction experienced by the ultrasonic wave as it passes from the transducer to the bulkhead. In the transducer, the the wave is approximately planar. As it enters the bulkhead, the wavefront becomes approximately spherical.

2.2.1 Impedance Mismatch

Ideally, the acoustic pulse that emanates from the transmitting transducer passes fully into the bulkhead, and all acoustic energy incident upon the receiving transducer from within the bulkhead is absorbed by that transducer. This ideal case is achievable when the transducer and bulkhead and are perfectly impedance matched. Due to

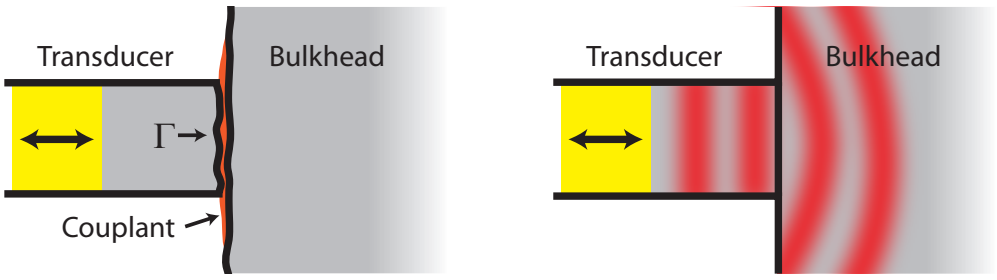

(a) Impedance mismatch (b) Diffraction

Figure 2.6: Sources of echoing in the ultrasonic channel

material mismatch and surface roughness, an impedance mismatch (and reflection) will always be present at the junction between transducer and bulkhead (Γ looking into the bulkhead in Figure 2.6(a)).

While impedance mismatch can be reduced by carefully matching the transducer to the bulkhead material and ensuring that the mating surfaces are very smooth, in some applications neither step is practical. Matching the transducer to the material properties of the bulkhead would require stocking a variety of transducer types (one for steel, one for aluminum, ...), while grinding or lapping the mating surfaces to ensure close contact would require special equipment that may not be available in most installations.

2.2.2 Diffraction

The transmitting ultrasonic transducer is modeled as a *piston source* [19], since the acoustic wave that emanates from its face is approximately planar. Figure 2.7 illustrates what happens as this wave enters the bulkhead (ignoring the impedance mismatch between the two components). According to Huygens principle [20], the acoustic wavefront at any time instant can be considered as a summation of point sources, each giving rise to a spherical wavefront. The summation of these wavefronts then describes the overall wavefront at some future time instant. For example, in

Figure 2.7, a plane wave emanating from the left hand transducer can be considered an infinite series of point sources along the transducer's face (only six are shown here). The wavefront from each point source expands, and the overall wavefront is given by their superposition. Diffraction causes the transmitted planar wavefront to become approximately spherical (although the exact shape is dependant on the signal wavelength relative to the transducer diameter) and as a result, not all of the transmitted energy impinges on the receiving transducer's face, even under perfect impedance matching. The shape of the wavefront is determined by the ratio of transducer diameter to bulkhead thickness. For $d/t \gg 1$ (thin bulkhead/wide transducer), the wave is approximately planar. For $d/t \ll 1$ (thick bulkhead/narrow transducer), the wave is approximately spherical.

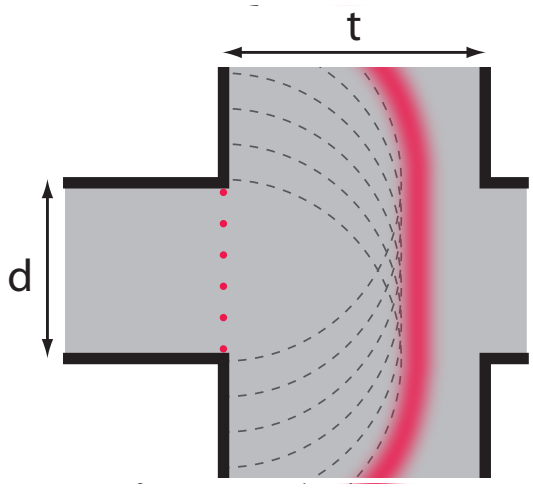

Figure 2.7: The acoustic wavefront as it travels through the bulkhead, as explained by Huygens principle

Several approaches have been developed to model ultrasonic transducers and wave propagation in ultrasonic imaging/NDT applications [21–24]. Many models treat ultrasonic propagation as a one-dimensional effect, modeled with lumped element com-

ponents and transmission lines [21–23]. Other approaches model acoustic propagation as a two or three-dimensional phenomenon [24]. We will show in Chapter 4 that while impedance mismatch effects are captured by the one dimensional models, diffraction effects are not.

2.3 Channel Capacity

Figure 2.4 shows that the ultrasonic channel's transient response consists of a series of echo pulses that result from acoustic energy being reflected within the bulkhead. To develop an upper bound on channel data capacity, we first consider the capacity supported by the channel *with the bulkhead removed*. This represents the presence of an ideal equalizer (which eliminates the acoustic echoes) inserted into the system. The channel's capacity is a function of two quantities, *signal-to-noise ratio* and *bandwidth*[3].

Signal-to-Noise Ratio (SNR) The channel's signal-to-noise ratio at the ultrasonic receiver was calculated for the rectangular transmission pulse shown in Figure 2.4 – 70 ns width and 5 volts amplitude. The receiver output was first sampled with no input signal applied to the channel, then with the rectangular pulse applied. The two recorded waveforms were used to calculate *noise power* and *signal plus noise power*, respectively,

$$P_n = \frac{1}{T}\int_T |r_n(t)|^2 dt \qquad P_{s+n} = \frac{1}{T}\int_T |r_{s+n}(t)|^2 dt, \tag{2.1}$$

where $r_n(t)$ is the noise only received signal, $r_{s+n}(t)$ is noisy received symbol, and T is the symbol period. In our testing, P_{s+n}/P_n ratios of $30 - 40$ dB $(1000 - 10000)$ have been measured.

[3]The signal-to-noise ratio, bandwidth and bitrate values presented here are based on the physical parameters of the test setup described in Figure 2.3.

Channel Bandwidth With the bulkhead removed and transmitting and receiving transducers placed in direct contact, the magnitude response of the channel was measured by transmitting a swept sinusoid and measuring the RMS value of the received signal. Figure 2.8 shows the result of this test performed over the 3-16 MHz range. This test reveals a 3 dB bandwidth of 2.9 MHz.

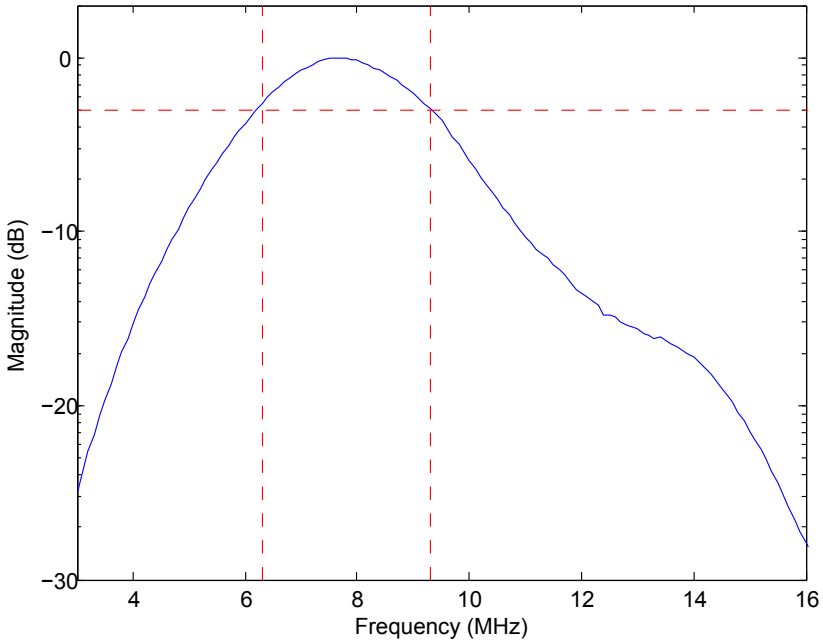

Figure 2.8: Channel frequency response – without bulkhead

Capacity With the channel bandwidth, signal power, and noise power, an upper limit on channel capacity can be calculated as

$$\begin{aligned} C &= B \log_2\left(1 + \frac{P_s}{P_n}\right) = B \log_2\left(\frac{P_{s+n}}{P_n}\right) \\ &= 2.9 \log_2(1000) \approx 29 \text{ Mbps.} \end{aligned} \tag{2.2}$$

Note that this channel capacity is a function of transducer choice (effecting bandwidth) and transmission pulse shape (effecting SNR). In the following investigation, we will continue to use the same transducer (the Panametrics NDT A112s 1/4" contact transducer) but investigate alternate pulse shaping techniques, using the channel capacity (Equation 2.2) as a benchmark.

2.4 Conclusion

The example in this chapter introduces the main impairment present in the ultrasonic channel – acoustic echoes. At high symbol rates, these echoes cause inter-symbol interference. When no equalization is performed, the symbol rate of the channel presented in this chapter is limited to approximately 200K samples/second. When the bulkhead is removed (eliminating echoes), the achievable symbol rate is on the order of 2.9M samples/second (commensurate with the channel's bandwidth). A properly designed channel equalized can effectively remove the effect of the bulkhead (i.e. suppress echoes) allowing ISI free communication at this higher symbol rate.

3. Review of Related Technologies

The ultrasonic communication system combines new modeling and equalization techniques with results from several existing research areas. This chapter provides an overview of the existing body of work that has been applied to the through-metal ultrasonic communication problem. This work includes topics from the fields of non-destructive testing and telecommunications. We identify how the reviewed work was extended to fit the unique requirements of our application.

3.1 Ultrasonic Communications

Ultrasonic signaling for digital communications has found widespread use in several technological areas. The most common use has been in underwater communication systems. The severe multipath impairments that exist in this environment have spurred the development of a host of new equalization techniques [25, 26]. Ultrasonic communication techniques have also been applied, to a lesser extent, to over-the-air channels [27]. While similar multipath impairments exist in this environment, this environment also suffers from high attenuation, limiting the usable range of such communication systems [28]. Over the last several years, ultrasonic through-metal communication systems have seen increasing interest [4]. Like the focus of the present study, these systems are targeted at non-invasive data transmission across metallic barriers whose structural integrity must be maintained.

3.1.1 Through-metal Communications

Beginning in the late 1990s, several groups have proposed using ultrasonic signaling for data transmission through metal barriers [3,4,6,7,29–31]. These include several

patent award [29–31]. The systems presented in the literature can be differentiated based on their bit rate and power consumption. The applications cited include data transmission through metal tanks and other "conductive envelopes" with thickness of up to six (6) inches.

One of the first proposed through-metal data transmission systems appeared in R. Welle's 1999 patent [29]. The system claimed communication between an external controller and an embedded sensor/actuator through an acoustic coupling medium, though the patent makes no mention of modulation scheme, achievable data rate, or implementation details.

One of the first peer-reviewed publications on the topic appeared in Saulnier et al., 2006 [4]. This study focused on transmission of data across steel barriers up to six inches thick. In the scenario presented, sensor data was conveyed from a sealed metallic container to an outside relay. The main objective was to produce a low complexity data repeater on the sensing side of the system so that power requirements on the sensing side would be minimized, making battery powered operation possible. A continuous wave was transmitted from the external transducer to the internal (sensor side) transducer, and a change in the receiver side transducer's load impedance was used to modulate data on the reflected signal. This passive sensor-side modulation can be accomplished with a relatively simple circuit as no transducer driver amplifier is needed; a transistor placed across the sensor-side transducer acts as the variable load impedance that will modulate reflected energy. The sensor-side hardware simplicity adds complexity in the driver-side hardware. Several design implementations were presented, using both pulse modulation and continuous wave modulation of data between transmitter and receiver. In all cases, the main limiting factor in system performance was acoustic echoing in the metal. The approach taken was to limit data rate so that the ISI due to channel echoes was negligible. In the very thick

specimens used in [4], this approach resulted in a data rate limitation of 450 bps. The authors conclude by suggested that performance can be enhanced by using some form of equalization.

One of the main contributions of [4] is the idea of moving transceiver complexity to one side of the metal barrier. The low complexity side of the system being the sensor side or the "interior," and the high complexity side being the "exterior." While the system in [4] provides electrical power to both the internal and external transceivers, the low hardware and computation complexity (and resulting low power requirement) of the interior transceiver suggests that it may be supplied using a power harvesting technique. The work presented in [5, 6] lays the groundwork for such techniques. Extracting power from the ultrasonic signal generated from the exterior transceiver, the interior transceiver can operate without battery power. Such systems are ideal for sensing within sealed containers, where the sensor may remain inaccessible for extended periods of time. Experimental results have shown a data rate of 55 kbps and power transfer of 0.25 W in [5] and 1 kHz, 30 mW operation in [6].

The concept of ultrasonic power transmission predates any of the published work in ultrasonic through-metal communication. One of the first published descriptions of a system for recovering and storing electrical energy from ultrasonic energy appeared in a 1997 patent [8]. Since this initial presentation of the concept, a more thorough analysis of ultrasonic power transmission system performance has been conducted [9, 32]. This technique, coupled with the data transmission techniques discussed previously, is being investigated for wireless monitoring in sample transport container for NASA's upcoming *Mars Sample Return Mission* [10].

Though the majority of the current research focuses on the use of *piezoelectric transducers* for through-metal applications [4–6], at least one group has studied the use of *electromagnetic acoustic transducers (EMATs)* instead [7]. These devices work

on a completely different operating principle than piezoelectric transducers; they induce a time varying Lorentz force in the metal specimen, that in turn sets up an acoustic wave. However, as a communication channel this system functions identically to its ultrasonic counterpart. Since EMATs induce an ultrasonic wave directly into the specimen, they do not require the tight binding that piezoelectrics need. Their main disadvantage is low conversion efficiency [33]. Their low efficiency translates into lower power transmission capabilities, and lower SNR in data transmission applications. Due to these limitations, the present study will focus exclusively on the use of lead zirconate titanate (PZT) piezoelectric transducers.

3.1.2 Summary of Capabilities

Table 3.1 summarizes the capabilities of the ultrasonic data transmission systems present in the literature. The table includes work done by our group as well, which is be elaborated on throughout the remainder of this thesis.

Paper	Bitrate	Application	Design Features
Saulnier, 2006	435 bps	Low power/complexity	Passive sensor-side modulation
Primerano, 2007	1 Mbps	High speed/low complexity	Echo cancellation
Shoudy, 2007	55 kbps	Power harvesting	Power harvesting, 250 mW
Kluge, 2008	1 kbps	Sealed containers	Power harvesting, 30 mW
Primerano, 2009	5 Mbps	High speed	Improved echo cancellation
Graham, 2009	2 Mbps	High speed	Uses EMATs and equalization

Table 3.1: Comparison of ultrasonic communication systems found in the literature

Though channel echoing is recognized as the most significant impairment to high-speed communication, most studies have not effectively dealt with the resulting ISI. Beyond our initial work in echo cancelation and channel modeling, Graham [7] is the only other source to have implemented any type of channel equalization for through-metal ultrasonic communication.

3.2 Non-destructive Testing

The ultrasonic through-metal communication channel is very similar to the axially aligned pitch-catch test configuration commonly used in non-destructive testing (NDT) [21]. In this arrangement, two transducers are placed in an immersion tank and directed toward one another, with the specimen under test placed between them. Several authors have constructed end-to-end models of this type of ultrasonic test setup [21, 22], and these results are applicable to the present work. By combining these models, which account for transmitter and receiver amplifiers, cabling, transducers, and acoustic channel, with models of acoustic echoing, an end-to-end simulation of our system can be constructed and used to design channel equalization filters. In this section, we review the relevant literature in the area of ultrasonic transducer, channel, and echo modeling.

3.2.1 Transducer Modeling

An ultrasonic transducer can be modeled as a two-port device; one port is electrical and the other acoustic. The mathematical models discussed in this section relate the voltage and current at the electrical port with the force and velocity at the acoustic port. Several techniques are presented in the literature to derive these transducer models, and they are briefly reviewed here.

Lumped-element Models The transducer's physical construction can be used as the basis for building an *equivalent circuit model* of the device. Several equivalent circuit models have been proposed over the years, including Mason's model [34] and the KLM model [35]. Redwood's version of Mason's equivalent circuit [36] is one of the most commonly used models, due to the ease with which it can be simulated using PSpice [37]. Figure 3.1 shows the Redwood equivalent circuit. It consists

of an electrical side and a mechanical side, coupled through a transformer. The transmission line on the acoustic side accounts for the propagation delay of acoustic signals through the transducer's thickness. While the circuit is drawn as a three port device (the voltage V, and two acoustic forces $F1$ and $F2$), one of the acoustic terminals is generally matched to a permanently bonded backing material, allowing the model to be treated as a two port device.

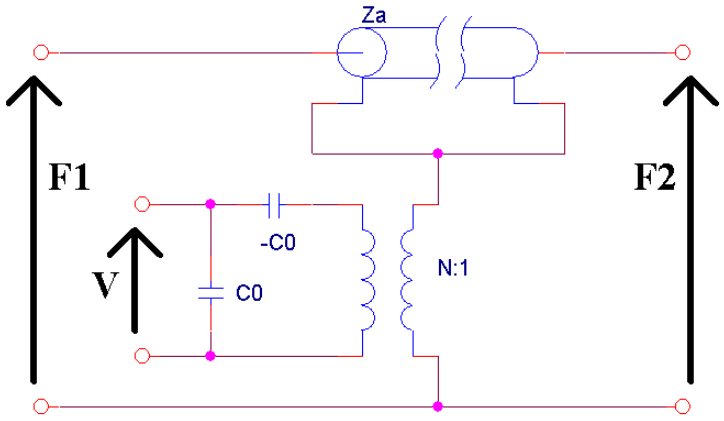

Figure 3.1: Redwood's equivalent transducer model represented in PSpice

To apply the Redwood model requires that we map the *physical* parameters of the transducer into the *electrical* parameters of the equivalent circuit. The model's electrical parameters are related to the transducer's physical parameters through the following relations [38–40].

$$Z_a = A\sqrt{c^D \rho_o} \tag{3.1}$$

$$C_0 = A\epsilon^s / l \tag{3.2}$$

$$N = 1/C_0 h_{33} \tag{3.3}$$

where the following are properties of the piezoelectric ceramic; A - cross-sectional area, c^D - elastic stiffness constant, ρ_o - density, ϵ^s - dielectric constant, l - thickness, h_{33} - piezoelectricity constant. The transducer's physical parameters are available from device manufacturers, or can be obtained through measurement. With these electrical properties determined, the model is complete.

The presence of an unrealizable negative capacitance is perceived as a disadvantage of this model, so several attempts have been made to simplify it. The Leach equivalent model [23], based on the Redwood model, replaces the transformer with two current-controlled current sources. The effect is to simultaneously eliminate the transformer and the negative capacitance. Since its introduction, the Leach model has been widely studied and simulated [41].

While other methods of transducer modeling have been developed, equivalent circuit models have the advantage that they directly reflect the transducer's physical construction. The piezoelectric crystal's capacitance, the acoustic transmission time through the crystal, and the presence of matching layers can all be modeled directly using lumped or distributed circuit components. System level models, consisting of transmitter and receiver electronics, cables, and transducers, can all be directly simulated in PSpice. Circuit based models are especially useful in transducer design. Since variables such as crystal thickness and diameter, and matching layer material are modeled explicitly, the circuit model provides insight into how changes in these quantities affect transducer operation.

Black Box Models Equivalent circuit models directly model many of the internal elements of an ultrasonic transducer. While such a representation is useful for transducer designers, the level of detail provided is often more than is required in many applications. Furthermore, when working with commercial transducers, the equivalent circuit component values are sometimes not available, as some manufacturers do

not supply sufficient information to calculate them.

Several modeling techniques have been developed that use experimental data to characterize the transducer. These "black box" models represent the transducer as a transfer function or transmission matrix, abstracting the details found in the equivalent circuit representation. In [21] the transducer is represented using the transfer matrix in Equation 3.4, which relates acoustic force and velocity at the transducer's face to voltage and current at its terminals. The parameters of this transfer matrix can be determined experimentally through electrical measurements using common NDT test setups [42].

$$\begin{bmatrix} V \\ I \end{bmatrix} = \begin{bmatrix} T_{11}^{A} & T_{12}^{A} \\ T_{21}^{A} & T_{22}^{A} \end{bmatrix} \begin{bmatrix} F \\ v \end{bmatrix} \tag{3.4}$$

In many NDT applications, users are interested only in determining the output acoustic signal for a given excitation voltage. In [43], a method of recovering the acoustic transfer function of the transducer using system identification is presented. By applying an voltage signal to the transducer and measuring its response with a hydrophone, system identification techniques can be used to approximate the transfer function.

3.2.2 Acoustic Echo Modeling

We have shown in Chapter 2 that the transient behavior of the ultrasonic through-metal communication channel consists of a series of echoes, corresponding to acoustic energy reflected within the channel. In order to build an effective equalizer for this channel, accurate estimation of the location and amplitude of these echoes must be made. The accurate estimation of received pulse parameters (arrival time, amplitude, spreading) is central to many ultrasonic imaging techniques, and many methods have

been proposed to achieve high resolution time difference of arrival (TDOA) estimation [44–46]. In this section, several of those methods are reviewed.

In ultrasonic TDOA estimation, the time difference between the transmission of a *reference* pulse, and the reception of a *reflected* pulse is the quantity of interest. It is common to assume that the reflected signal is identical to the reference signal, except for a time delay, i.e. the reflected signal $s(t) = r(t - \tau)$ where $r(t)$ is the reference signals, and τ is the time delay between the two [45]. The simplest method of time delay estimation is by locating a peak in the cross-correlation of the two signals. Due to the computational complexity of this approach, however, researchers have developed more efficient techniques that work well with high SNR signals [44]. In ultrasonic time delay estimation, the relatively slow variations in echo characteristic allow averaging of multiple consecutive echoes to be used to increase estimate accuracy [45].

In many situations, the assumption that reflected signals are time shifted version of the reference signal is not valid. Non-flat attenuation and group delay in the acoustic medium will generally distort the reference signal causing the reflected signal to be significantly different. Furthermore, the attenuation and delay properties of the medium may be of interest, in addition to the the reflected signal's time delay. In medical imaging, for example, these properties may indicate the type of tissue through which the signal passes [46]. Using a *Gaussian echo model* (Equation 3.5), the reflected signal's time delay and dispersion properties can be estimated.

$$\begin{aligned} s[\theta; n] &= \beta\, e^{-\alpha\,(nT-\tau)^2} \cos\left(2\,\pi\, f_c\,(nT-\tau) + \phi\right) \\ \theta &= [\,\alpha \quad \tau \quad f_c \quad \phi \quad \beta\,] \end{aligned} \tag{3.5}$$

The Gaussian pulse, shown in Figure 3.2, is defined by five parameters: band-

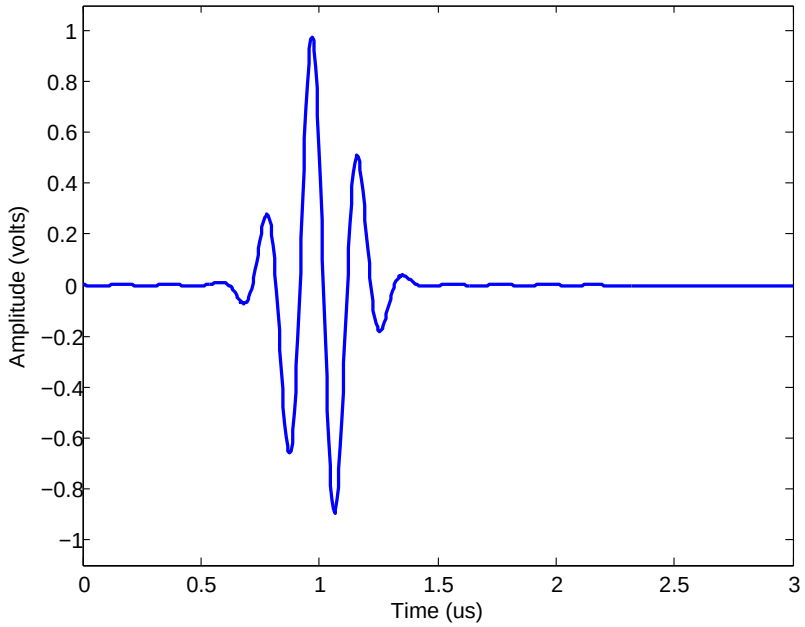

Figure 3.2: Gaussian pulse representing ultrasonic reflection

width factor (α), time delay (τ), center frequency (f_c), phase (ϕ), and amplitude (β). Estimation of these parameters amounts to fitting the model to experientially gathered echo data [46]. In general, the reflected signal will contain multiple echo components, each corresponding to a separate defect/discontinuity in the specimen under test. This estimation technique has been extended to simultaneous estimation of multiple echoes, and estimation of periodic echo trains [47]. Since the transient response of the ultrasonic channel is characterized by an exponentially decaying (equally spaced) pulse train, simultaneous estimation of multiple echoes is especially important.

3.3 Communication Channel Equalization

The ultrasonic communication channel suffers from several impairments that are commonly encountered in many other telecommunication systems. Acoustic echoes in

the metal barrier lead to *inter-symbol interference* (ISI) while the resonant behavior of the transducers results in a *band limited* channel. These phenomena were discussed in Sections 2.2 and 2.3, respectively. The most common way of dealing with these impairments is to construct an equalization filter placed in cascade with the channel.

Linear Equalizers The earliest channel equalizers for digital communication were designed for data transmission over voice channels [18], and took the form of transversal (tapped delay line) filters. The filter design problem amounts to proper selection of filter taps so as to minimize some performance metric. The most common method of choosing the tap coefficients of a transversal equalizers is to use the minimum mean-square-error (MMSE) criterion [48]. Using this approach, tap coefficients are selected to minimize the error criterion

$$J(\mathbf{c}) = E|I_k - \hat{I}_k|^2, \tag{3.6}$$

where I_k is the transmitted symbol, and $\hat{I}_k$ is the received symbol at the output of the equalizer. It can be shown that J is a quadratic function of the tap coefficient vector $\mathbf{c}$ [18], and therefore can be minimized using a variety of search methods – the stochastic gradient method being one of the most popular. The MSE approach is widely used in practice because it is robust in the face of high noise and large ISI [49].

Decision Feedback Equalizers Many communication channels containing strong multipath components exhibit deep spectral nulls [18]. A linear equalizer combats channel impairments by forming an approximate inverse of the channel's response. As a result, a channel with a spectra null at f_0 will result in an equalizer having high gain at that frequency. This high gain causes the equalizer to degrade SNR (referred to as *noise enhancement*). To overcome this limitation, non-linear equalizer architectures

have been developed. One of the most popular is the *decision feedback equalizer (DFE)*. A DFE tracks the last N symbols received, and uses that information to cancel ISI from the symbol currently being received [50, 51].

The structure of the DFE is shown in Figure 3.3. It consists of two filters, a feedforward filter and a feedback filter. The feedforward filter is designed to compensate for *precursor ISI*, while a feedback filter compensates for *postcursor ISI*. Noise enhancement is avoided in the DFE because this equalizer does not attempt to invert the *entire* channel response, only the portion that corresponds to postcursor ISI (which is accomplished with the feedforward filter). Precursor ISI is canceled using *noiseless* symbol decisions feed back from the slicer output.

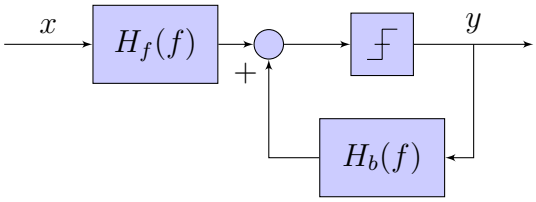

Figure 3.3: The Decision Feedback Equalizer

The two filters that form the DFE are usually implemented as tapped delay lines, just as with the linear equalizer. The optimization of its filter coefficients can be accomplished using the same procedures used for linear equalizer design. While decision feedback equalizers outperforms linear equalizers in many applications, DFE performance can quickly degrade in high noise channels. When the DFE feeds back an incorrect symbol decision, *error propagation* can result. Basically, an incorrect decision made on the *currently received* symbol increases the likelihood that the *next* symbol will be interpreted incorrectly as well. It has been shown that error propagation leads to burst errors in the DFE's output, which are generally self correcting [52].

Adaptation Before an equalizer can function properly, it must be calibrated to the channel over which it is to operate. The simplest method of calculating the proper equalizer coefficients for a given channel is to send a known *training sequence* through the channel, and measuring the error between the received symbol's value and the transmitted value [13]. The resulting error vector is then used to train the equalizer.

Using this approach, the equalizer can be retrained periodically by resenting the training sequence at some interval. Alternatively, for channels that are slowly time varying, the equalizer may implement an *decision directed* approach to continually adapt [53] to the channel. A common approach to adaptive equalizer design is to first train the equalizer using a training sequence, then switch to a decision directed mode to provide on-line adaptation.

In some systems, the need to transmit a training sequence (which contains no useful data) to tune the equalizer can add substantial overhead. As an alternative, *blind equalization* techniques have been developed. An example of a blind equalization technique is the *constant modulus algorithm (CMA)* [54]. Phase-shift keyed modulation generates a carrier signal that has constant modulus (envelop). The CMA seeks to adjust equalizer taps to achieve a constant modulus in the received signal. Any deviation from constant modulus is used as an error signal that drives the adaptation algorithm. In this way, equalizer adaptation can be performed without explicit transmission of a training signal [13, 55].

3.4 Application to the Present Work

The ultrasonic through-metal communication environment shares similarities with more commonly encountered (and more thoroughly studied) hardwired and radio frequency channels. The interference experienced in the ultrasonic channel is similar to wireless multipath fading, for example. A key difference in the ultrasonic channel

is that interference is well structured, consisting of an exponentially decaying pulse train. This can be used to our advantage to design particularly simple transceiver architectures when low data rates are needed (the focus of Chapters 5). At high data rates, more elaborate channel equalization techniques must be applied (the focus of Chapters 6).

In recent years, several through-metal ultrasonic communication system designs have emerged. No effort has been made to develop accurate mathematical models of the ultrasonic channel, however. The topics presented in this chapter address modeling and analysis of *components* of the ultrasonic communication channel. In the following chapter, these will combined to form a *complete* channel model. In particular, we will develop a transfer function that relates the electrical signal at the input of the transmitting transducer to the electrical signal at the output of the receiving transducer.

4. Ultrasonic System Model

In this chapter, mathematical models are developed for each of the components that comprise the ultrasonic communication channel: transmitting transducer, bulkhead, and receiving transducer. These models provide insight into the nature of acoustic echoes, and allows us to test echo channel equalization techniques in simulation. A block diagram of the ultrasonic communication system is shown in Figure 4.1.

Figure 4.1: Block diagram of the ultrasonic communication system

The subsystem blocks shown in Figure 4.1 reflect the placement of components in the ultrasonic communication system. In Section 4.5, we will show that the system is linear, allowing us to rearrange blocks as needed to simplify modeling.

4.1 Transducer-Bulkhead Decomposition

We have observed that the transient response of the ultrasonic channel consists of a *primary* received pulse followed by a series of *echo* pulses. Furthermore, the echo portion of the response is what we seek to eliminate. Rather than develop explicit models of the transmitting transducer, bulkhead, and receiving transducer, we will first recast the transducer-bulkhead-transducer subsystem (which will be referred to as the *acoustic channel*) into a form that models the primary pulse and echo pulses.

The acoustic channel is a cascade of three components, shown in Figure 4.2: the

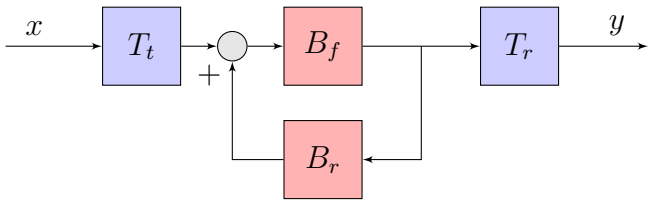

Figure 4.2: The components of the *acoustic subsystem*

transmitting transducer (T_t), the bulkhead, and the receiving transducer (T_r). The bulkhead is further decomposed into forward and reverse paths (B_f and B_r respectively), which accounts for the echoing observed in the system's transient response. The transfer function of the channel in Figure 4.2 in terms of these blocks is

$$H_c = \frac{T_t B_f T_r}{1 - B_r B_f} \tag{4.1}$$

Under the assumption of linearity (which will be discussed in Section 4.5), the system can be expanded and rearranged into the representation shown in Figure 4.3. This representation shows two signal paths. The first is through the transmitting transducer, bulkhead forward path, and the receiving transducer. The second path circulates from the output through the bulkhead reverse path, and the bulkhead forward path. The latter accounts for channel echoes. It is straightforward to verify that this representation is also described by Equation 4.1.

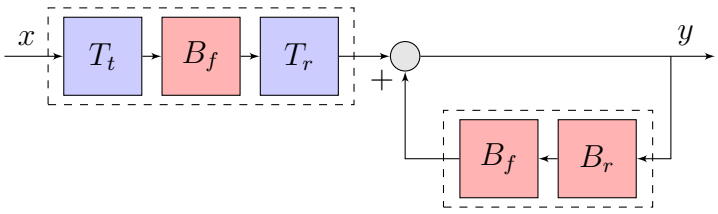

Figure 4.3: Expanded and rearranged channel elements

For convenience, the blocks in Figure 4.3 are grouped into two transfer functions. P is the transfer function of the primary path, and E is the transfer function of the echo path. With these definitions, the transfer function in equation 4.1 can be rewritten as Equation 4.3.

$$H_c = \frac{T_t B_f T_r}{1 - B_r B_f} = \frac{P}{1 - E} \tag{4.2}$$
$$P = T_t B_f T_r, \quad E = B_r B_f$$

The simplified channel block diagram in Figure 4.4 partitions the channel into two subsystems. P relates the input pulse to the *primary* output pulse, and E relates successive *echo* output pulses to one another.

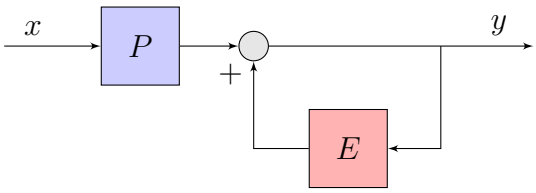

Figure 4.4: Channel partitioned into *primary* (P) and *echo* (E) subsystems

Rather than model the components in Figure 4.2 directly, we will base the acoustic subsystem's model on the derived blocks in Figure 4.4. In addition to providing a direct interpretation of the echoing phenomena in the channel, we will show in subsequent sections that models for these blocks can be easily extracted from experimental data.

4.2 Primary Path Model

The primary signal path in the acoustic channel consists of the cascade of transmitting transducer, bulkhead forward path, and receiving transducer, i.e. $P = T_t B_f T_r$. Extensive work has been done on modeling the individual components of the primary path [21, 22, 36, 43]. For example, [43] uses a system identification to extract a rational transfer function approximation of the transducer. The equivalent circuit model in [36] produces a PSPICE compatible simulation model of the transducer. Many of the commonly used transducer modeling techniques are discussed in greater detail in Section 3.2.1. In general, each of these two-port models relates an *electrical* signal at one port of the transducer to an *acoustic* signal at the other port. In our application, however, two transducers are placed back-to-back (with the bulkhead between them) with the resulting system containing two electrical ports – the acoustic signals are internal to the system. In this section, two methods of modeling the primary signal path will be considered. The first is a frequency domain approach, while the second is a time domain approach. Each method uses experimental channel input-output data to form the model.

4.2.1 Transfer Function Model

Adapting the system identification technique used in [21, 43], which models the electrical-acoustic transfer function of a *single* transducer, we have developed a method of modeling the entire primary signal path (*both* transducers *and* the bulkhead froward path) as a cascade of a rational transfer function and a pure delay, expressed as $P(z) = P_l(z)z^{-d}$. The lumped element portion of the transfer function, $P_l(z)$, accounts for the frequency selective effects of the transducers and bulkhead, while z^{-d} accounts for the acoustic delay contributed by those components. The form of $P_l(z)$

is given by Equation 4.4.

$$P(z) = P_l(z)\, z^{-d} \tag{4.3}$$

$$P_l(z) = \frac{b_P(1) + b_P(2)z^{-1} + \cdots + b_P(M_P+1)z^{-M_P}}{a_P(1) + a_P(2)z^{-1} + \cdots + a_P(N_P+1)z^{-N_P}} \tag{4.4}$$

Using system identification techniques, the coefficient vectors $\boldsymbol{b_P}$ and $\boldsymbol{a_P}$ and the time delay d can be determined from channel input-output data. The details of the primary path modeling algorithm are presented in Section 4.4.2, including an automated method of probing the channel and processing the resulting input-output data used to estimate the parameters of Equation 4.3.

4.2.2 Analytical Pulse Model

The Gaussian pulse model was introduced in Section 3.2.2 as a model sometimes used to describe the response of ultrasonic transducers in the time domain. The pulse is defined by five parameters that control its amplitude, bandwidth, time offset, resonant frequency, and phase.

$$s(t) = be^{-a(t-\tau)^2} \cos\left(2\,\pi\, f\,(t-\tau) + \phi\right)$$

The Gaussian pulse modeling approach is particulary useful in estimating the delay between two echo pulses, which indicates the round trip pulse time. Figure 4.5 shows the primary received pulse and first echo to emanate from the bulkhead,and a pair of Gaussian pulses fitted to that data. An estimate of the round trip time can be calculated once the pulses are fitted to the data, by taking the difference in the delay values of the two pulses (i.e. $\Delta\tau = \tau_2 - \tau_1$).

Gaussian pulse fitting is especially useful for parametric detection of ultrasonic echoes in low SNR environments. In our application, this time domain approach

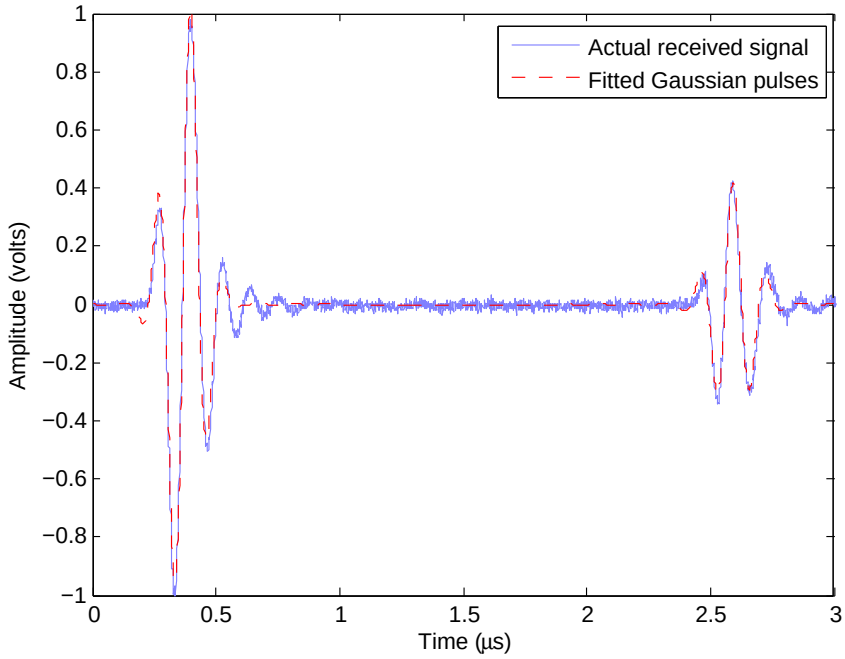

Figure 4.5: Gaussian pulses fitted to two consecutive echoes

is used primarily for estimation of transducer center frequency and round-trip echo time.

4.3 Echo Path Model

The second block of the acoustic channel – $E(z)$ in Figure 4.4 – accounts for the echo portion of the transient response. This block consists of the forward and reverse bulkhead paths, modeling the dispersive effects of the bulkhead material, the time delay of the acoustic signal traveling through the material, and the signal reflections from the front and back faces of the bulkhead. Two modeling methods will be presented in this section. In the first, the bulkhead is modeled as a cascade of a rational transfer function and a delay element, just as was done in modeling the primary path. This effectively treats the bulkhead as a one dimensional structure. The second approach uses an analysis technique called Finite Difference Time Domain

(FDTD) simulation to model the true three dimensional propagation phenomena of the bulkhead. While the former yields a simple, closed form model, the latter captures propagation effects that are ignored by the one dimensional model.

4.3.1 Lumped Element Model

Following the same procedure that was used to model the primary signal path, the echo path is assumed to be the cascade of a rational transfer function and an ideal delay, $E(z) = E_l(z)z^{-r}$. Here, the delay z^{-r} accounts for the *round trip* acoustic delay of the channel, and $E_l(z)$ models the frequency selective effects of the bulkhead. The form of $E_l(z)$ is identical to that of the primary signal path's lumped element component.

$$E(z) = E_l(z)\, z^{-r} \tag{4.5}$$

$$E_l(z) = \frac{b_E(1) + b_E(2)z^{-1} + \cdots + b_E(M_E+1)z^{-M_E}}{a_E(1) + a_E(2)z^{-1} + \cdots + a_E(N_E+1)z^{-N_E}} \tag{4.6}$$

The details of the echo path modeling algorithm are presented in Section 4.4.3, including an automated method of probing the channel and processing the resulting input-output data used to estimate the parameters of Equation 4.5.

4.3.2 Acoustic Propagation Simulation

The bulkhead model developed in Section 4.3.1 is a one-dimensional approximation of the three dimensional acoustic propagation within the bulkhead. As such, some effects of the physical system are unmodeled. For example, in Section 6.1.2, we will use this model to build an equalizer that *should* provide perfect cancelation of channel echoes according to the one-dimensional model. In reality, a residual echo remains, and can only be accounted for by considering a more detailed bulkhead model.

While impedance mismatch is the dominant mechanism for producing channel echoes, diffraction (which the 1D model does not capture) experienced as the acoustic pulse passes from the transducer to the bulkhead also leads to echoes, even under perfect acoustic impedance matching. In this section, we present a three-dimensional simulation model that provides greater insight into the nature of channel echoes.

Acoustic Propagation The propagation of acoustic signals is governed by the *acoustic wave equation*, a second order partial differential equation describing acoustic pressure and particle velocity as a function of both time and space. The finite difference time domain (FDTD) method provides a means of approximating a solution to the wave equation. This technique was first developed for electromagnetic propagation simulation [56], but has since been extended to acoustic applications [57]. FDTD analysis is a grid based technique that begins by dividing the physical region of interest into a series of *cells* and the time range of interest into *time steps*.

Consider an infinitesimal volume element of air being acted on by a pressure gradient in the x-direction. The relationship between the element's velocity, and the pressure differential is described as

$$\frac{\partial p}{\partial x} = -\rho \frac{\partial u}{\partial t} \tag{4.7}$$

where $\partial p/\partial x$ is the pressure gradient acting on the element, ρ is the *density* of the material, and u is the element's velocity. Note that this is analogous to the relationship $F = ma$. The negative sign indicates that the element accelerates in a direction opposite the pressure gradient.

The pressure gradient across the volume element causes the element to deform. From Hooke's law, we know that the stress and strain in an elastic medium (like air) are linearly related. The relationship between the change in size of the volume

element and the corresponding change in pressure is given by

$$\frac{\partial u}{\partial x} = -\frac{1}{B}\frac{\partial p}{\partial t} \tag{4.8}$$

where $\partial u/\partial x$ is the velocity differential across the element, B is the *bulk modulus* of the material, and p is the pressure of the element. Note the correspondence between this relationship and Hooke's law, $F = -kx$.

Equations 4.7 and 4.8 form the basis of the FDTD method for acoustics. They can be solved simultaneously for either pressure or velocity to yield two equivalent forms of the *acoustic plane wave equation*,

$$\frac{\partial^2 p}{\partial t^2} = \frac{B}{\rho}\frac{\partial^2 p}{\partial x^2}$$
$$\frac{\partial^2 u}{\partial t^2} = -\frac{B}{\rho}\frac{\partial^2 u}{\partial x^2}.$$

The propagating characteristics of a homogenous elastic material can be complectly described by its density and bulk modulus. From these parameters, two important quantities can be calculated, the wave propagation velocity (c) of the medium, and the characteristic impedance (Z_0) of the medium.

$$c = \sqrt{\frac{B}{\rho}} \tag{4.9}$$

$$Z_0 = \sqrt{\rho B} = \rho c \tag{4.10}$$

Where two dissimilar materials, a wave will experience a reflection if there is an impedance mismatch between the materials. The acoustic reflection coefficient is defined as

$$\Gamma = \frac{Z_1 - Z_0}{Z_1 + Z_0}, \tag{4.11}$$

where Z_0 is the characteristic impedance of the material that the wave originates in, and Z_1 is the characteristic impedance of the material that the wave passes into. Note the similarity between the definitions of reflection coefficient in acoustics and electromagnetics.

Finite Difference Time Domain (FDTD) Algorithm The FDTD algorithm works by discretizing the physical region of interest into cells, approximating the spacial derivatives in 4.7 and 4.8 as pressure and velocity differences between adjacent cells. Similarly, time derivatives are approximated by dividing the time interval of interest into small time steps. Using the approximations,

$$\frac{\partial f(x,t)}{\partial x} \approx f(x,t) - f(x-1,t)$$
$$\frac{\partial f(x,t)}{\partial t} \approx f(x,t) - f(x,t-1)$$

the pressure and velocity equations for plane wave propagation can be rewritten in discrete form. The FDTD algorithm proceeds as follows. At $t = 0$, initial values for the pressure and velocity components are defined for each cell. At each time step moving forward, the pressure and velocity values for each cell are updated in two stages. In the first stage, the pressure values of each cell are updated according to

$$p(x,t) = p(x-1,t) - \rho[u(x,t) - u(x,t-1)]\,\frac{\Delta t}{\Delta x}. \tag{4.12}$$

In the second stage, the velocity values for these cells are updated according to the following, completing one time step of the simulation.

$$u(x,t) = u(x-1,t) - 1/B[p(x,t) - p(x,t-1)]\,\frac{\Delta t}{\Delta x}. \tag{4.13}$$

Note that for simplicity Equations 4.12 and 4.13 are written for a 1D plane wave case. They can, however, be extended to 2D and 3D simulation.

Simulation Setup The FDTD simulation was conducted in Matlab. Though the acoustic propagation phenomenon occurs in three dimensions, due to axial symmetry, a 2D simulation gives identical results. Figure 4.6(a) shows the geometry and regions defined for the simulation. Figure 4.6(b) shows how the geometry is divided using a square mesh. Each cell of the mesh has its own density (ρ) and bulk modulus (B) defined based on the material properties of that region.

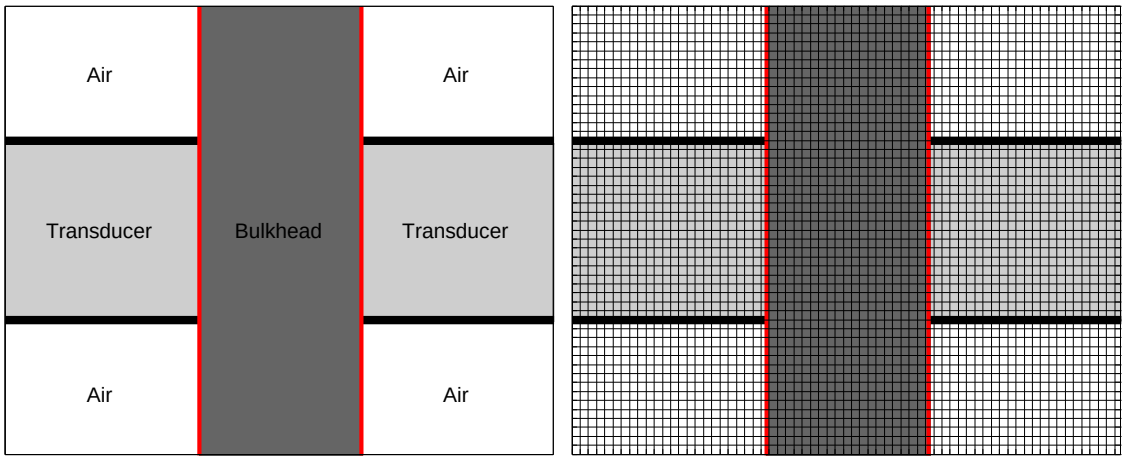

(a) Simulation geometry (b) Meshed geometry

Figure 4.6: The geometry and mesh used for the FDTD simulation

The transducer width and the bulkhead thickness are both 6 mm. The analysis grid spacing is 0.1 mm, and the analysis region measures 20 mm x 15 mm. Each simulation is run for one thousand time steps, approximately 14 μs. An acoustic source located at the leftmost face of the left side transducer. At each time step, the acoustic force measured at the plane of each transducer (the face contacting the

bulkhead) was measured.

Simulation Results Using the setup described above, several simulations have been performed to analyze the effect of material mismatch and transducer misalignment on the channel's transient response.

• ***Material Mismatch*** Transducers purchased for non-destructive testing are often designed to be matched to a particular type of material. Matching the characteristic impedance of the transducer to the material being tested results in a low reflection coefficient at the junction between transducer and specimen under test and maximizes the power coupled from transducer to specimen. Impedance matching between the transducer crystal and the specimen under test (or in our case, the bulkhead) is usually done by bonding a *quarter wavelength matching layer* to the crystal during manufacturing.

In our application, impedance mismatch causes not only poor power coupling, but is also the major cause of channel reflections (and therefore ISI). Figure 4.7 illustrates simulation results where a transducer matched to aluminum has been used with a steel bulkhead. Figure 4.7(a) shows the acoustic pulse originating within the transmitting transducer. In Figure 4.7(b), the pulse has entered the bulkhead. Due to the impedance mismatch between transducer and bulkhead, the reflection coefficient at the interfaces between the two is $\Gamma = -0.48$. As a result, only portion of the incident energy is coupled into the bulkhead. The remainder is reflected back into the transmitting transducer. Figure 4.7(c) shows the acoustic pressure distribution just after the transmitted pulse strikes the receiver side of the bulkhead. Again, a portion of this signal passes into the transducer, and a portion is reflected back into the bulkhead. Finally, in Figure 4.7(d), the signal is re-reflected from the transmitter side of the bulkhead and travels back to the receiver side.

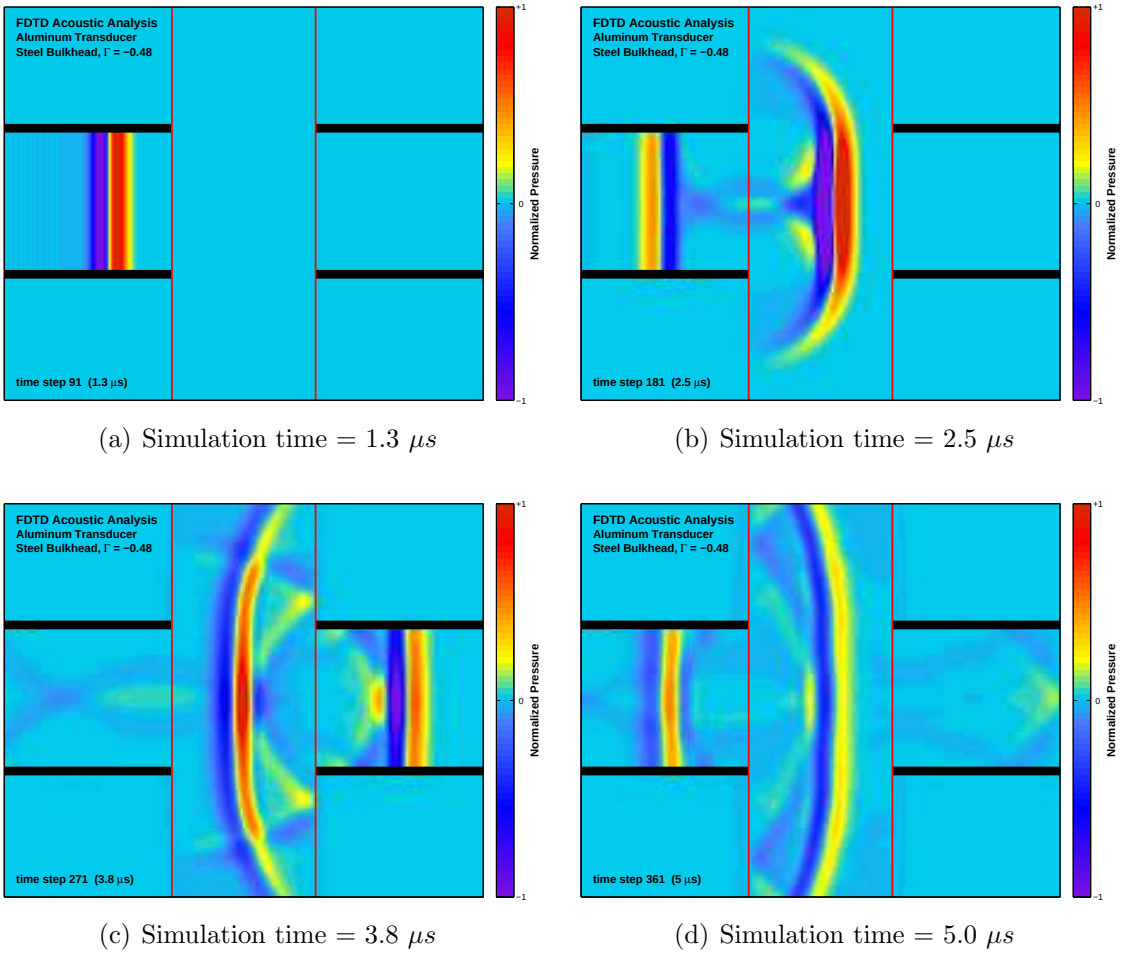

(a) Simulation time = 1.3 μs

(b) Simulation time = 2.5 μs

(c) Simulation time = 3.8 μs

(d) Simulation time = 5.0 μs

Figure 4.7: FDTD simulation, steel bulkhead and aluminum matched transducer

At each time step, the acoustic force measured at the face of each transducer (where it contacts the bulkhead) is measured. Figure 4.8 shows the acoustic force at the transmitting and receiving transducers over the duration of the simulation. Just as with the experimental results, a strong primary received pulse is seen, followed by an exponentially decaying series of echo pulses.

Using Equation 4.11, we determine that at the aluminum-steel interface, $\Gamma = -0.48$ looking into the steel bulkhead. This value can also be determined from the transient response when the exact material properties required by Equation 4.11 are

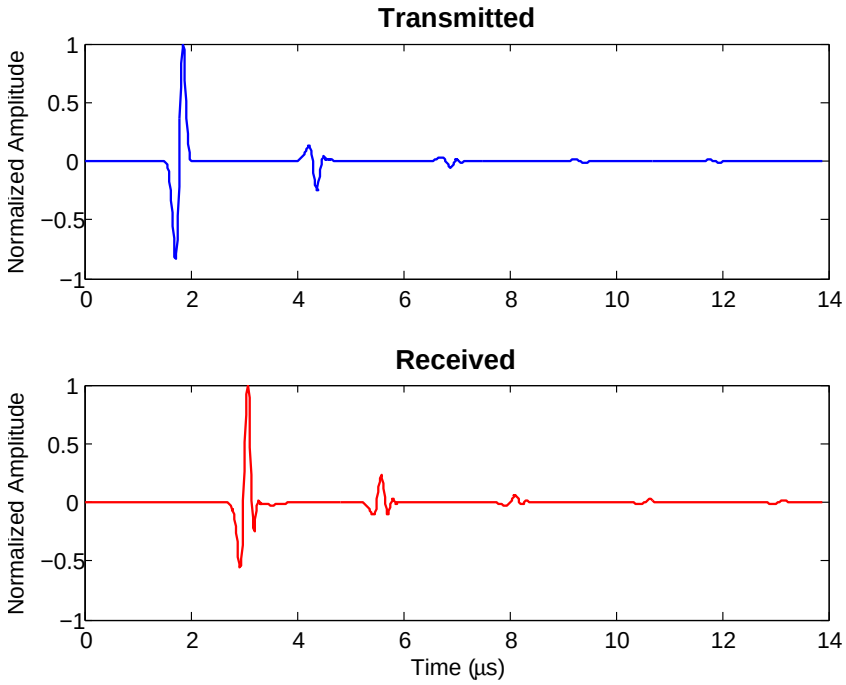

Figure 4.8: Acoustic force at transmitter and receiver faces, steel-aluminum

not known. Figure 4.9 illustrates the process of successive reflection in the bulkhead and shows the amplitude level of the echoes after successive bounces, as well as the amplitudes of the primary received pulse (a_p) and first echo (a_e) emanating from the bulkhead. From the figure, we see that the ratio of these two quantities leads to

$$\frac{a_e}{a_p} = \Gamma^2 \;\rightarrow\; \Gamma = \sqrt{\frac{a_e}{a_p}}. \tag{4.14}$$

By measuring the amplitudes of the first two pulses to emanate from the bulkhead and using Equation 4.14, the value of the coefficient can be experimentally determined. This relationship demonstrates that large acoustic mismatch leads to large echo amplitude, and slow decay of the echo pulse train.

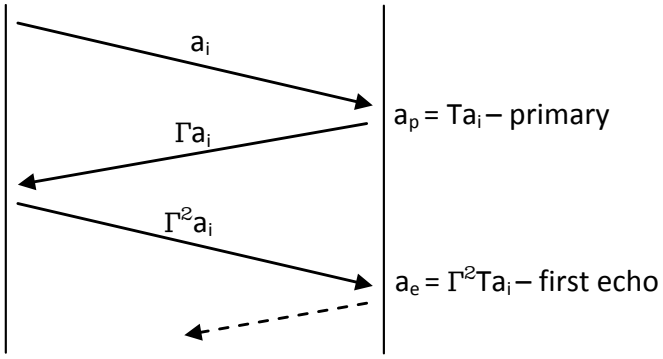

Figure 4.9: Determination of echo amplitude levels

• ***Perfect Transducer-Bulkhead Matching*** In the previous simulation, acoustic echoes were attributed to impedance mismatch between the transducer and bulkhead. Next, we look at the case where the two are prefectly impedance matched – a situation that can never quite be achieved in practice. Figure 4.10 shows four snapshots of this simulation at the same time steps as in the previous simulation. The acoustic pulse generated by the transmitting transducer in Figure 4.10(a) enters the bulkhead in Figure 4.10(b). In Figure 4.10(c), the incident acoustic pulse strikes the receiver side of the bulkhead. The majority of the energy is coupled to the transducer, but due to *diffraction* the pulse spreads while traveling, and some acoustic energy is reflected back into the bulkhead. Note the circular wavefronts that emanate from the top and bottom edges of the receiving transducer in Figure 4.10(c). Figure 4.10(d) shows these wavefronts re-reflecting back toward the receiver side of the bulkhead.

This simulation reveals that even with perfect transducer-bulkhead matching, echoes will still be present in the channel. This effect goes unmodeled in the transfer function model (Equation 4.6). There are, in fact, two effects that contribute to channel echoes; *impedance mismatch* causes signal energy to reflect from the transducer-bulkhead interfaces, while *diffraction* causes the spreading and reflection from the edges of the transducers and the surrounding bulkhead. The acoustic pressure mea-

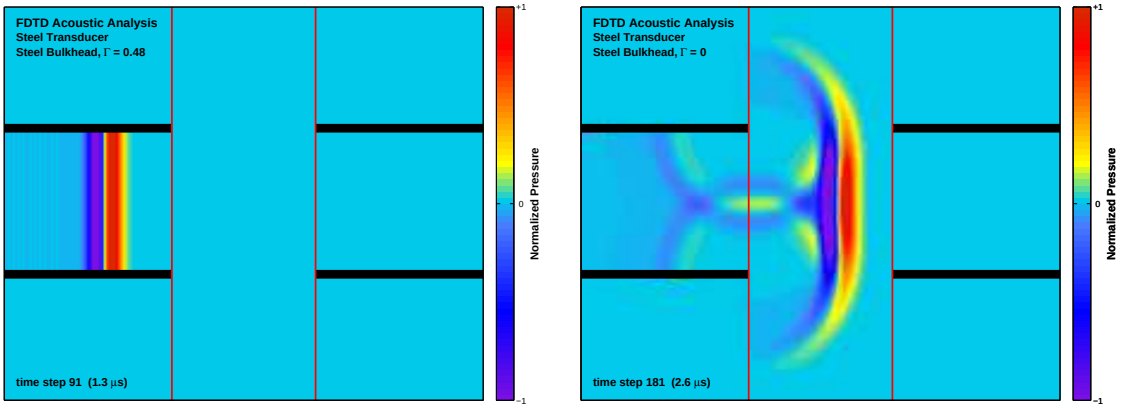

(a) Simulation time = 1.3 μs

(b) Simulation time = 2.6 μs

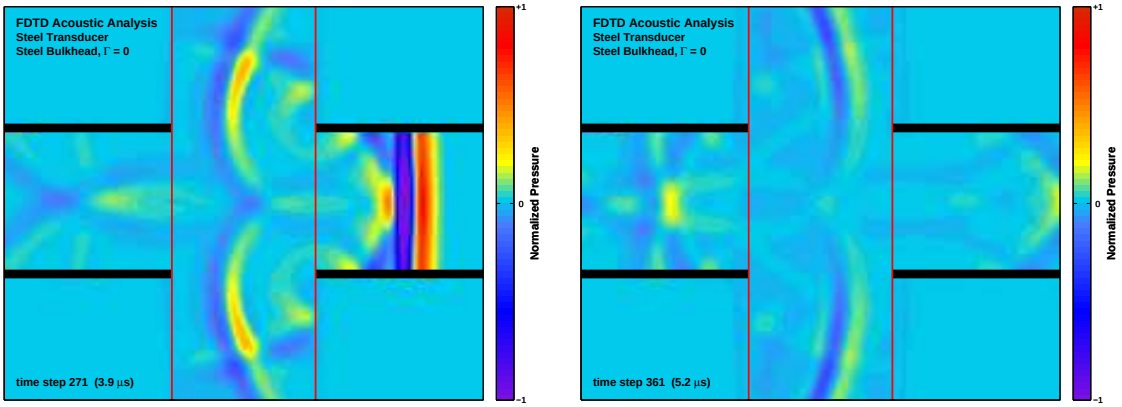

(c) Simulation time = 3.9 μs

(d) Simulation time = 5.2 μs

Figure 4.10: FDTD simulation, steel bulkhead and steel matched transducer

sured at the face of the receiving transducer is shown in Figure 4.11.

Following the same procedure that was used in the previous simulation, Equation 4.14 can be used to find the *apparent* reflection coefficient based on the amplitude of the primary and first echo pulses from Figure 4.11, yielding $\widehat{\Gamma} = 0.25$. Since the actual refection coefficient for this simulation run is zero, the non-zero value calculated here is due to the diffraction effects noted earlier. While this exercise shows that under well matched conditions, the reflection coefficient reported by Equation 4.14 yields a large error, the error diminishes as the actual reflection coefficient increases. In

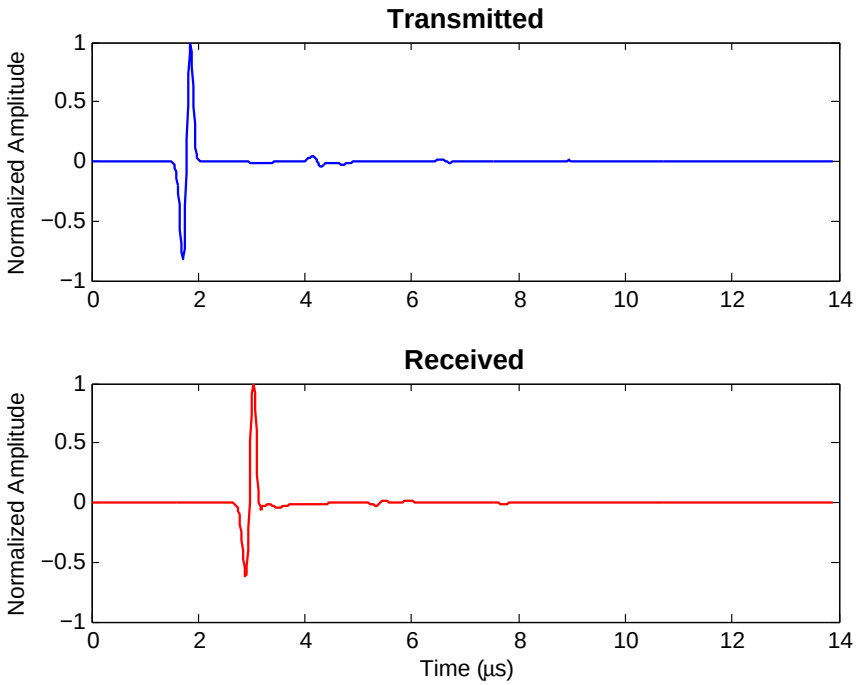

Figure 4.11: Acoustic force at transmitter and receiver faces, steel-aluminum

the hardware testing presented later, we will see that very small values of Γ are not achieved in practice (typical values are in the range of $0.45 - 0.65$), and the experimentally derived value (from Equation 4.14) is quite close to the actual value (from Equation 4.11), within 5%.

• ***Transducer Misalignment*** The final simulation examines the effects of axial misalignment between the transmitting and receiving transducers. Misalignments of $0-5$ mm in 1 mm increments were examined using the aluminum-steel configuration.

The six curves in Figure 4.12(a) show the primary received pulses under misalignments of $0-5$ mm. As misalignment increases, the energy coupled from transmitter to receiver decreases. Figure 4.12(b) shows the power coupling from transmitter to receiver as a function of misalignment. The results are normalized with respect to zero misalignment. For the 6 mm wide transducers used in this simulation, a mis-

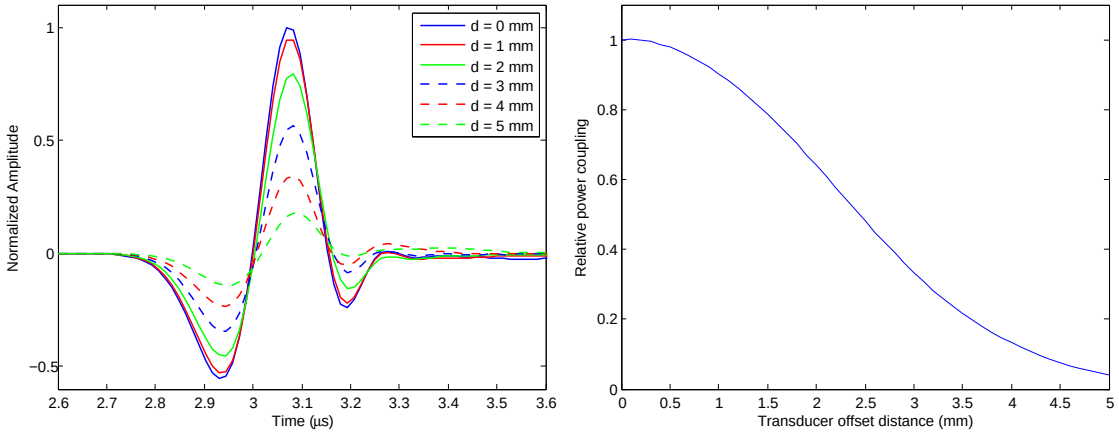

(a) Primary Rx pulses (b) Energy coupling vs. misalignment

Figure 4.12: Transducer misalignment test results

alignment of 2.5 mm causes a 3 dB reduction in coupled power and a misalignment of 4.5 mm causes a 10 dB reduction in coupled power.

Figure 4.13 shows four frames of the 3 mm misalignment test, again at the same time instants as the prior simulations. The simulation shows that the effect of misalignment is to cause a large fraction of the transmitted energy to be reflected back into the transmitting transducer.

4.4 Channel Model Estimation

In the previous sections, we discussed techniques for modeling the components of the ultrasonic channel. In particular, the channel shown in Figure 4.4 has a transfer function given by

$$H_c = \frac{P}{1-E} = \frac{P_l(z)z^{-d}}{1-E_l(z)z^{-r}}, \tag{4.15}$$

where $P_l(z)$ and z^{-d} are the lumped element and delay components, respectively, of the *primary path* transfer function, while $E_l(z)$ and z^{-r} are the corresponding components of the *echo path* transfer function. In this section, a technique for calculating

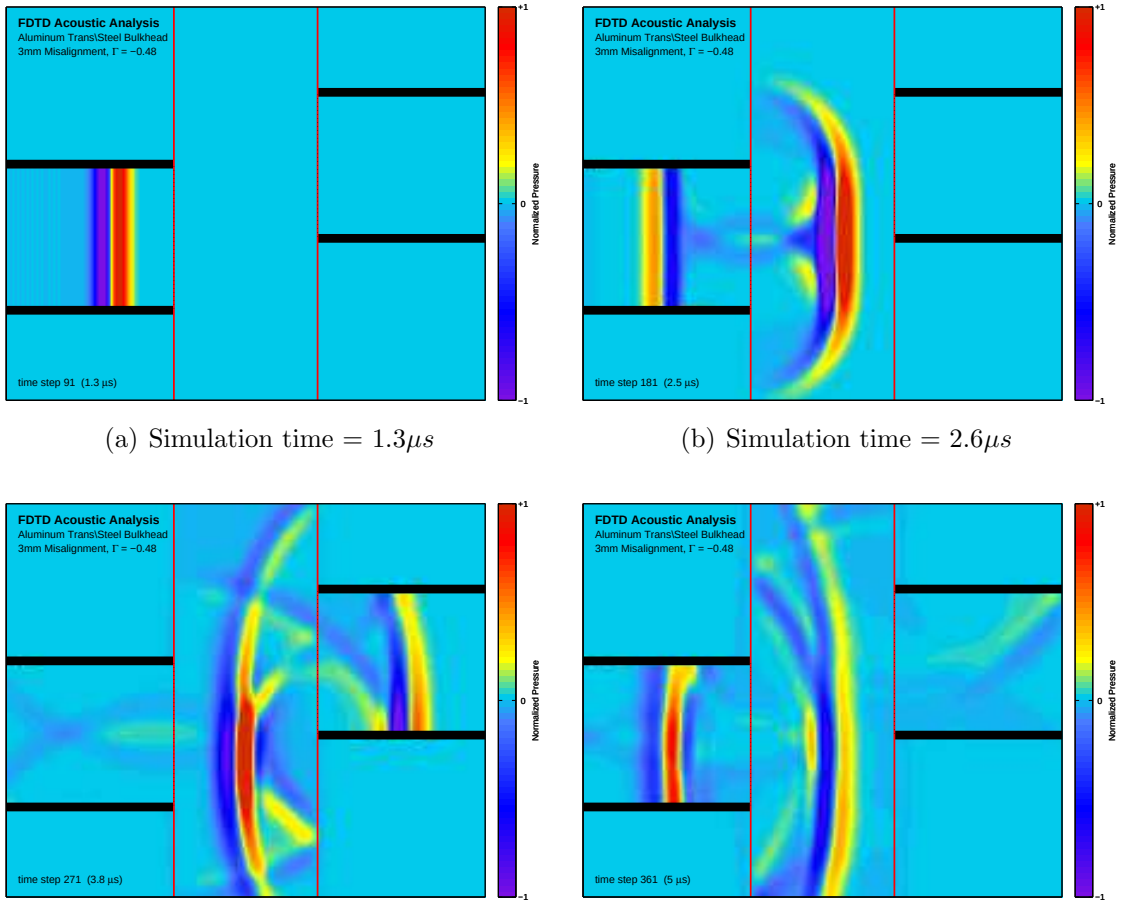

(a) Simulation time = $1.3\mu s$

(b) Simulation time = $2.6\mu s$

(c) Simulation time = $3.9\mu s$

(d) Simulation time = $5.2\mu s$

Figure 4.13: FDTD simulation, steel bulkhead and aluminum matched transducer, 2mm misalignment

the parameters for these transfer functions using *system identification* is presented.

The top and bottom curves in Figure 4.14 show the input and output signals, respectively, produced when the test setup in Figure 2.3 is excited with a 70 ns, 5 V amplitude rectangular pulse. In this section, a technique will be presented that uses the transient response data along with system identification techniques to build models for the primary and echo paths.

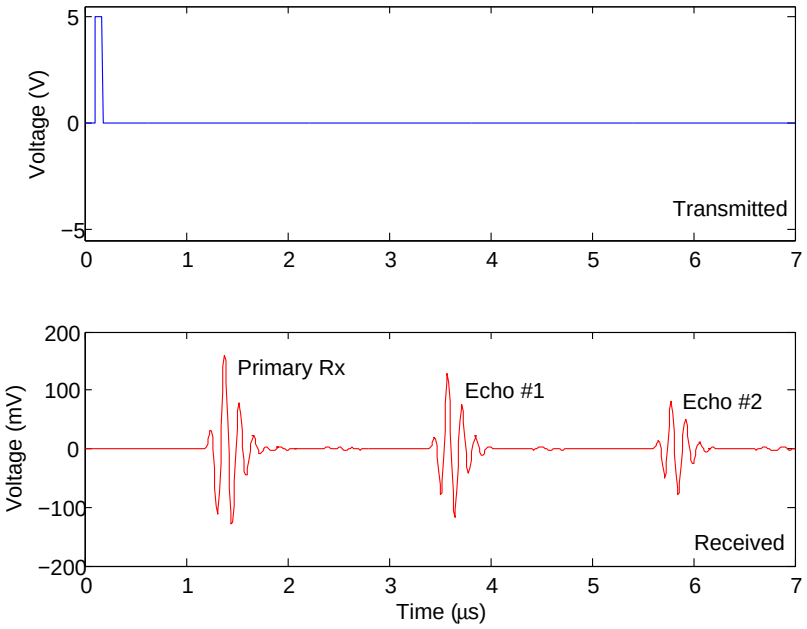

Figure 4.14: Channel transient response used to generate input-output data pairs

4.4.1 System Identification

System identification is the process of forming a mathematical model of a dynamic system based on experimental data gathered from that system. System identification is particularly useful when it is difficult or impractical to develop a system model based on first principles. In such cases, *black box models* are used to describe the behavior of a system. This approach was taken in developing the models in Equations 4.3 and 4.5, where we assumed the structure of each subsystem (rational transfer functions), but did not determine values of the model coefficient. Presently, we consider how to determine the values of these coefficients from experimental data.

Sending a known input signal $x[n]$ into a physical system $P(z)$ produces a measured output signal $y[n]$. Sending that same input $x[n]$ into a model of that system, denoted $\widehat{P}(z)$, produces an output $\hat{y}[n]$. The goal of system identification is to minimize the error between the actual system's response, and that of the model. The

error is usually defined in the mean-squared sense,

$$\min_{b_P, a_P, d} \sum_{i=0}^{k} |\hat{y}[n] - y[n]|^2, \tag{4.16}$$

where the input-output data record has length k. The minimization for the primary path transfer function ($P(z)$, Equation 4.3) is performed with respect to the model coefficient vectors $\boldsymbol{b_P}$ and $\boldsymbol{a_P}$ and time delay d. The input-output data needed to calculate $P(z)$ can be obtained from the transient response waveforms shown in Figure 4.14. In this study, the Steiglitz-McBride iteration [58] is used to compute the model coefficients. The Steiglitz-McBride iteration is a *linear* parametric modeling technique, i.e., it is used for identification of linear discrete-time models like the ones we have used to describe $P(z)$ and $E(z)$. With the model structure determined, input-output data must be generated so that model coefficients can be found.

4.4.2 Primary Path Input-Output Data

The transfer function $P(z)$ relates the transmitted pulse to the *primary* received output pulse (see Figure 4.14). To estimate $P(z)$ using system identification, the transmitted pulse and primary received pulse are extracted from the channel transient response and used as the input and output, respectively, for the Steiglitz-McBride iteration. Figure 4.15 shows these two curves overlayed on the same plot. The time delay d between the two has been removed for clarity.

4.4.3 Echo Path Input-Output Data

The echo transfer function $E(z)$ relates successive echoes to one another. For example, *echo 1* in figure 4.14 results from passing the *primary received pulse* through $E(z)$, and *echo 2* results from passing *echo 1* through that same transfer function. The input-output data needed to estimate $E(z)$ is obtained by isolating the primary

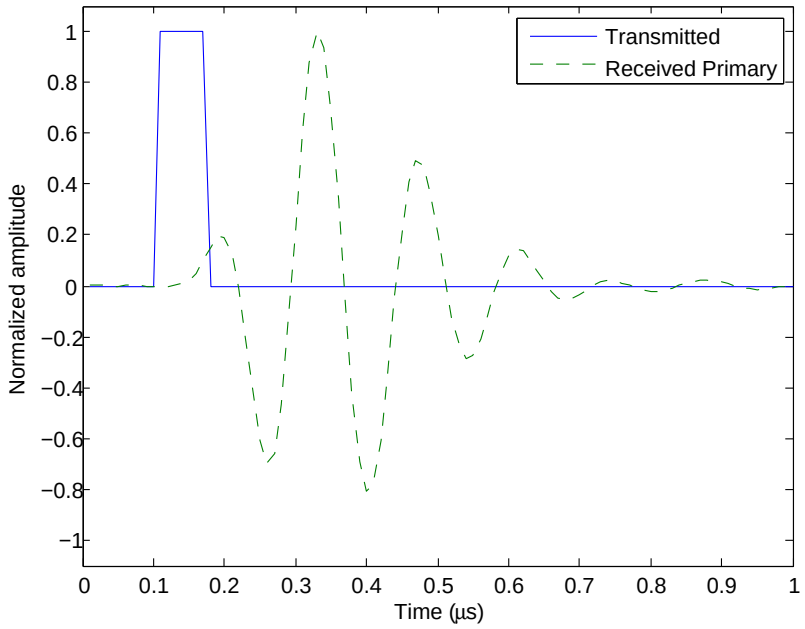

Figure 4.15: The transmitted pulse and primary received pulse aligned.

received pulse and first echo, and using those as the input and output data for the Steiglitz-McBride iteration applied to $E(z)$. Figure 4.16 shows these two curves overlayed on the same plot. Again, the time delay between the two has been removed for clarity.

4.4.4 Parameter Estimation Algorithm

The algorithm for estimating channel model parameters from the the channel's transient response is summarized in the following steps. In the following discussion, model orders for $P(z)$ and $E(z)$ are assumed to be known and fixed. The issue of model order estimation will be addressed subsequently.

1. Excite the channel with a step function and measure the resonant frequency of the transducers.

2. Excite the channel with a pulse matched to the transducer's resonant frequency

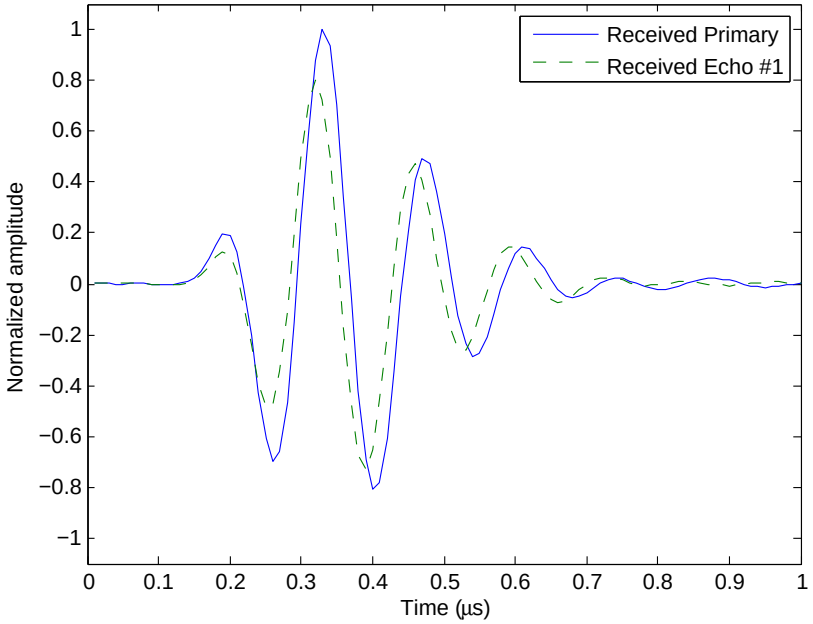

Figure 4.16: The primary received pulse and first echo aligned.

and record transient response.

3. Form initial estimate of channel round trip delay.

4. Extract *primary received pulse* and *first echo* from transient response.

5. Estimate parameters [$\boldsymbol{b_E}$ $\boldsymbol{a_E}$ r] of $E(z)$ using extracted *primary received pulse* and *first echo*.

6. Estimate parameters [$\boldsymbol{b_P}$ $\boldsymbol{a_P}$ d] of $P(z)$ using known *transmitted pulse* and extracted *primary received pulse*.

The bulkhead is first excited with a step input then re-excited with an optimal rectangular. The rectangular pulse has higher energy in the channel's passband, and results in a higher SNR received signal on which to perform parameter estimation. The acoustic round trip time is then estimated by calculating the envelope of the received pulse and locating the first two local maxima of that envelope. The distance

between these two points gives the estimated round trip time. Figure 4.17 shows this estimation for a 0.635 cm thick steel bulkhead, with the two peaks marked by □ symbols.

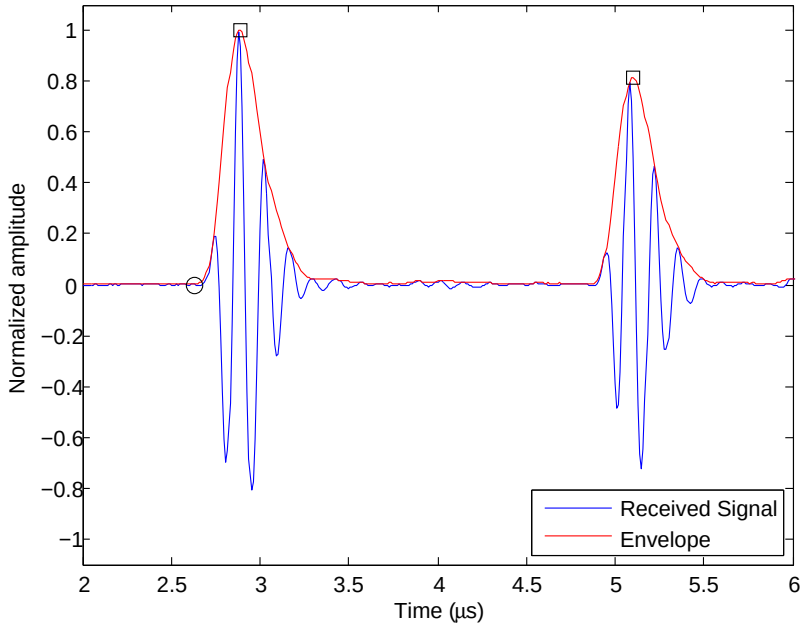

Figure 4.17: The complex envelope of the received signal with peaks marked

From Figure 4.17, the estimated round trip delay was 2.21 μs. This yields a propagation speed of

$$c = \frac{2 * 0.635 \text{ cm}}{2.21 \ \mu\text{s}} = 5750 \text{ m/s},$$

which is consistent with published engineering data for the speed of sound through steel. The envelope formed in Figure 4.17 is also used to extract the two echo pulses. By searching to the left of the first peak for the envelope to decay to zero, the start of the primary received pulse can be found. This point is shown in Figure 4.17 by a ○ symbol. With the start of the first received pause and the time between pulses

known, the first two received pulses can be extracted.

Next, the extracted pulses are used by the Steiglitz-McBride iteration to determine model parameters for $E(z)$ and $P(z)$. At the conclusion of the iteration, the coefficients for the lumped element and time delay components of each block are determined.

Offline Determination of Model Order Thus far, the orders of the numerator and denominator terms in $P_l(z)$ and $E_l(z)$ have been assumed known. The order of each transfer function is determined by the dynamic properties of the channel's primary and echo paths. For a given set of transducers and bulkhead, these orders are fixed, however, they must be estimated at least once for each installation. We have developed an algorithm to determine a suitable model order based on residual mean-squared error between the channel response and model response. The steps described below are in terms of $P_l(z)$, but the same algorithm is used for estimating the model order of $E_l(z)$.

1. The system identification algorithm is run over a set of rational transfer function models $P_l(z : M, N)$, where the numerator (M) and denominator (N) orders are noted explicitly. The residual error is recorded for each run.

2. An error threshold is set based on the smallest residual error from the group. All models whose error exceeds that threshold are excluded.

3. Of the remaining models, the one with the smallest combined order $(M + N)$ is selected, and its order is chosen as the order for that subsystem.

For our system, the algorithm was iterated over the range of $M \in \{2, ..., 8\}$ and $N \in \{2, ..., 8\}$. The motivation for choosing the model with lowest combined order (in step 3) is that this value relates directly to the number of multiply-accumulate

operations needed to calculate an output from the filter for each input. Thus, this step results in choosing the least computationally complex model within the acceptable residual error range. At the conclusion of the algorithm, the model orders for $P(z)$ and $E(z)$ were found to be $M_P = 3$, $N_P = 6$ and $M_E = 3$, $N_E = 2$, respectively. Using the laboratory testbed, the algorithm results in the following expressions for the primary and echo transfer functions.

$$P(z) = \frac{-0.0004108\ z^{-3} + 0.00183\ z^{-4} - 0.002546\ z^{-5} + 0.001137\ z^{-6}}{1 - 4.863\ z^{-1} + 10.36\ z^{-2} - 12.32\ z^{-3} + 8.613\ z^{-4} - 3.359\ z^{-5} + 0.574\ z^{-6}}\ z^{-110}$$

$$E(z) = \frac{0.08627 - 0.06211\ z^{-1} - 0.05301\ z^{-2} + 0.05128\ z^{-3}}{z^{-1} - 1.705\ z^{-2} + 0.864\ z^{-3}}\ z^{-221}$$

4.5 Model Validation

In this section, the ultrasonic channel model developed in Section 4.1 and tuned in Section 4.4 is validated using experimental data gathered in the time and frequency domains. Using such a model, the channel's response to arbitrary inputs can be simulated, including the response to digital waveforms. Furthermore, an accurate simulation model allows us to assess the effects of various digital modulation and equalization techniques. In subsequent chapters, the channel model will be used to simulate the performance of several channel equalization algorithm.

The simulations presented here were performed in SIMULINK®, using the model shown in Figure 4.18. Note the direct correspondence between this and the system block diagram of Figure 4.4. The sample period used in the simulation is 100 ns ($f_s = 100$ MHz). The *primary* and *echo* paths are each represented by a cascade of a delay element and a transfer function. The bulkhead's round-trip delay is 221 samples,

or 2.21 μs. This value matches the time delay estimated from Figure 4.17.

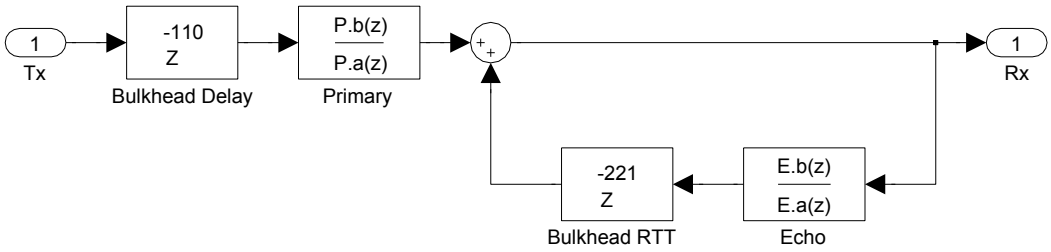

Figure 4.18: Representation of the acoustic channel in SIMULINK®

4.5.1 Frequency Response

In Chapter 2, it was illustrated that the introduction of the bulkhead into the ultrasonic channel causes spectral nulls, associated with the standing wave pattern within the bulkhead. Figure 4.19(a) shows a frequency sweep performed on the channel (with bulkhead in place) over the $0 - 22$ MHz range, and Figure 4.19(b) shows the same sweep conducted with the simulation model.

From the two plots several quantities can be measured. Values for channel center frequency, null spacing, and null depth at center frequency are given in table 4.1.

Quantity	**Physical**	**Simulation**	**% error**
Center frequency	7.75 MHz	7.78 MHz	0.4 %
Null spacing	460 kHz	458 kHz	0.4 %
Null depth	6.70 dB	6.59 dB	2.5 %

Table 4.1: Comparison of measured quantities from physical bulkhead and simulation model

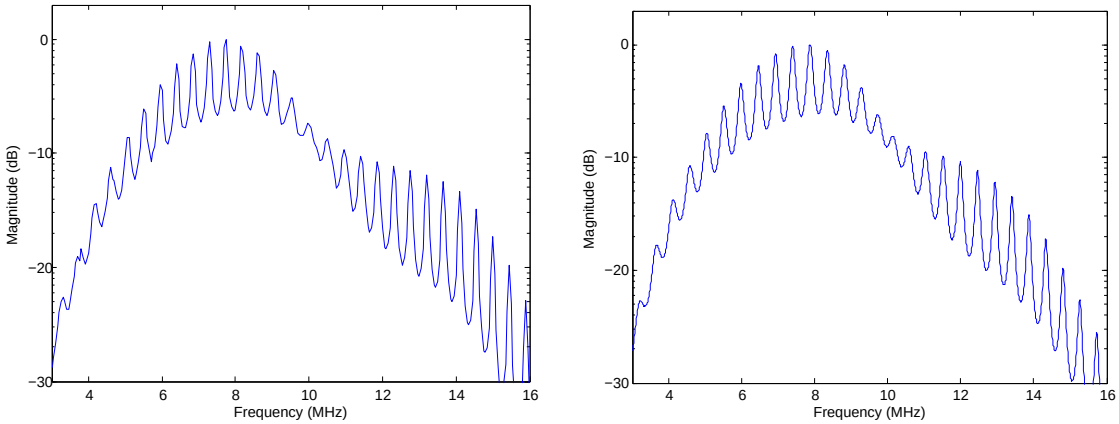

(a) Physical channel (b) Simulated channel

Figure 4.19: Frequency response of real and simulated channels

4.5.2 Transient Response

The time domain behavior of the channel model has been tested with several representative inputs. The accuracy of the model is determined by measuring the error between the outputs of the physical and simulated systems when subject to the same input.

Response to a single rectangular pulse The channel parameter estimation algorithm uses a pulse matched to the channel's resonant frequency as its excitation signal. The top curve in Figure 4.20 show the response of the physical system when excited with that pulse. The middle curve shows the output of the simulation model (after estimating its parameters using the procedure in Section 4.4) when subject to the same input pulse. As expected, the error between the two signals (bottom curve) is small. The peak error between real and simulated outputs is less than 3% over the duration of the output signal.

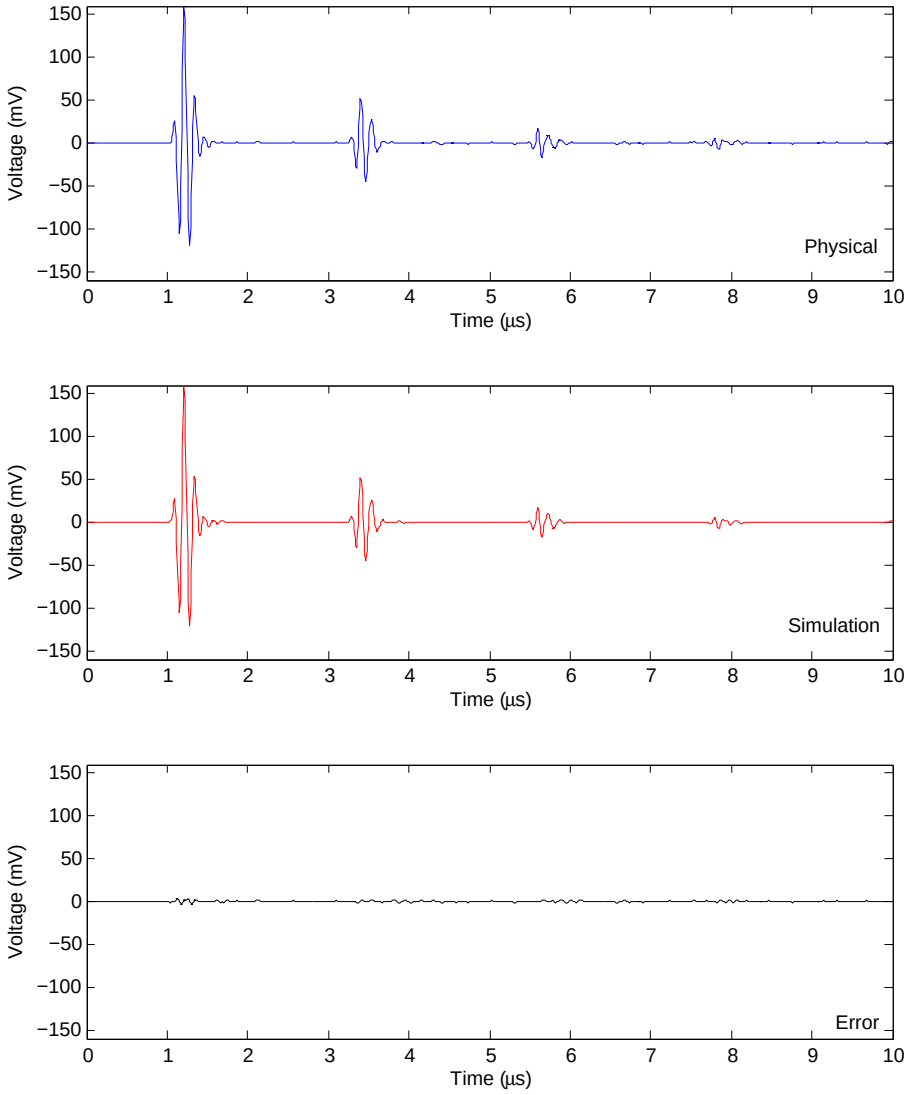

Figure 4.20: Responses of physical and simulated system - single input pulse

Response to data symbol sequence The results in Figure 4.21 show a more interesting case where a series of pulses are transmitted in sequence. This is representative of using binary pulse-amplitude modulation (PAM) to to transmit the binary sequence 1101011 at a symbol rate of 2 μs. The top waveform shows the transmitted sequence, and the middle waveform shows the simulated received sequence. This simulation clearly demonstrates the intersymbol interference introduced by closely spaced

transmitted symbols. The pulses at 6 μs and 9 μs are the result of channel echoes. If a simple energy detection based receiver were used, these echoes would result in bit errors. The error between simulation received signal and that of the physical system is shown in the bottom waveform. Again, the amplitude error between actual and simulated outputs is less than 3%.

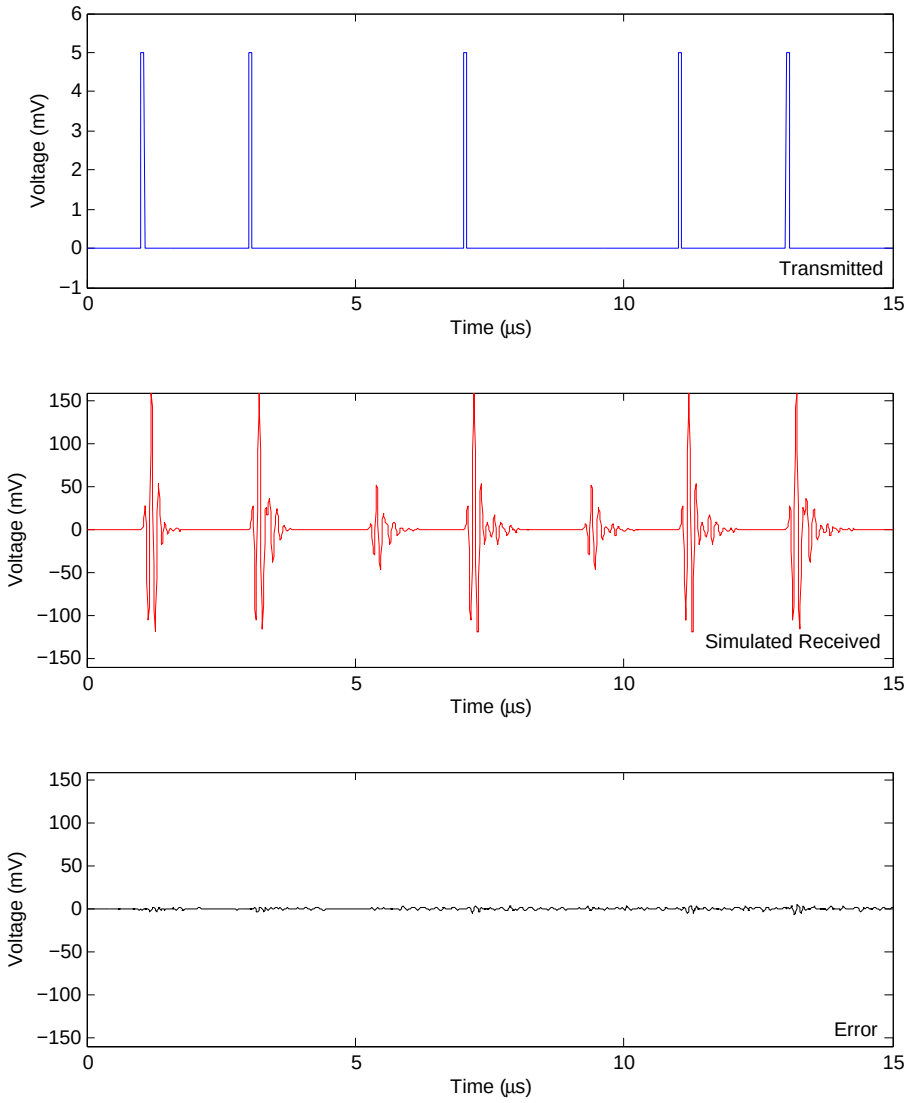

Figure 4.21: Responses of simulated system - series of data pulses

Response to an arbitrary waveform The final test shows the response of the real and simulated channels to an arbitrary input waveform. The top pane of Figure 4.22 shows the transmitted waveform. The bottom pane shows the outputs form both the physical and simulated systems, overlayed. The time axis has been expanded to show only the primary received pulse. The exotic transmitted pulse used here may considered the superposition of scaled, shifted versions of the "basic" pulses used in the training algorithm. The agreement between real and simulated responses indicates that the linear model assumption is reasonable.

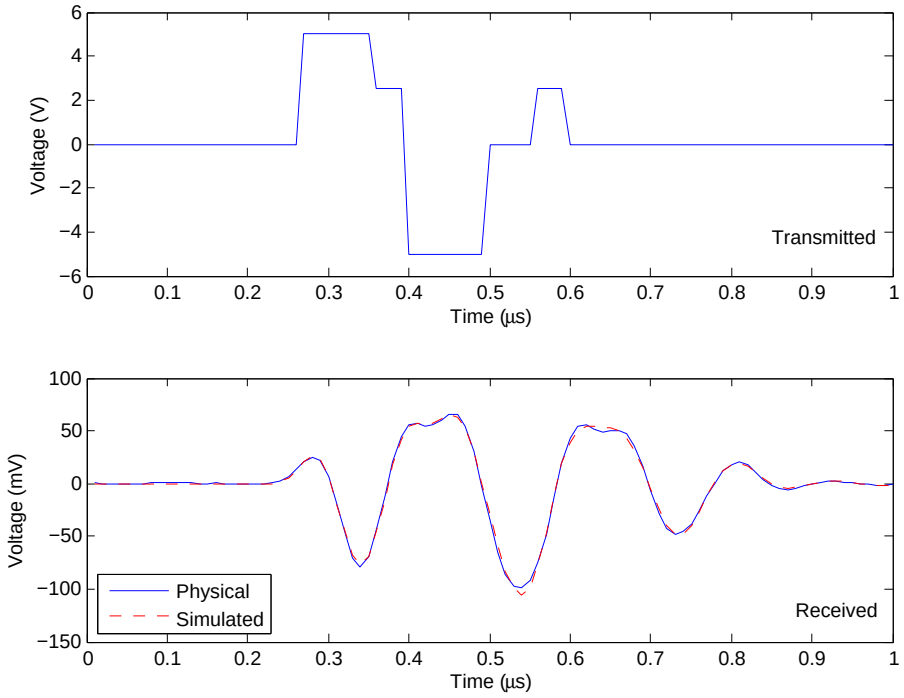

Figure 4.22: Responses of physical and simulated systems - arbitrary pulse shape

4.5.3 Test of Channel Linearity

The channel model developed in Section 4.1 assumes that the ultrasonic channel is linear. The tests conducted in the previous section do not contradict this hypothesis. In this section, two additional tests are performed to the error between the response of the physical system and that of the linear model.

Consider a system described by the operator G that maps inputs $x(t)$ into outputs $y(t)$, expressed as $y(t) = G(x(t))$. Given any two inputs $x_1(t)$ and $x_2(t)$, and their respective outputs $y_1(t)$ and $y_2(t)$, the system G is linear if and only if the properties of *additivity* and *homogeneity* hold, i.e.

$$\alpha_1 y_1(t) + \alpha_2 y_2(t) = G(\alpha_1 x_1(t) + \alpha_2 x_2(t)).$$

To measure how closely the linear model matches the physical system's response, we begin by constructing two waveforms $x_1[n]$ and $x_2[n]$, and sending them into the system. Figure 4.23(a) shows the input-output pair $x_1[n]$ and $y_1[n]$. The signal $x_1[n]$ is a 60 ns pulse with 1 volt amplitude. Figure 4.23(b) shows the input-output pair $x_2[n]$ and $y_2[n]$. The signal $x_2[n]$ is a 100 ns pulse with 1 V amplitude followed by a second 100 ns pulse with -1 V amplitude. These two pulses have been chosen because they are spectrally rich and linearly independent of one another.

The remainder of this section describes the tests that were performed to individually test for homogeneity and additivity in the channel, and the numerical results obtained.

Homogeneity The set of input signals $x[n] = \alpha\, x_2[n]$ for $\alpha \in [-5, \ldots, 5]$ volts was sent through the channel and the output $y[n]$ was recorded. For each input, the signal $\hat{y}[n] = \alpha\, y_2[n]$ was generated, and the *error signal* $e[n] = \hat{y}[n] - y[n]$ was calculated. Over the {-5 5} volt amplitude range of interest, the error signal's peak amplitude was

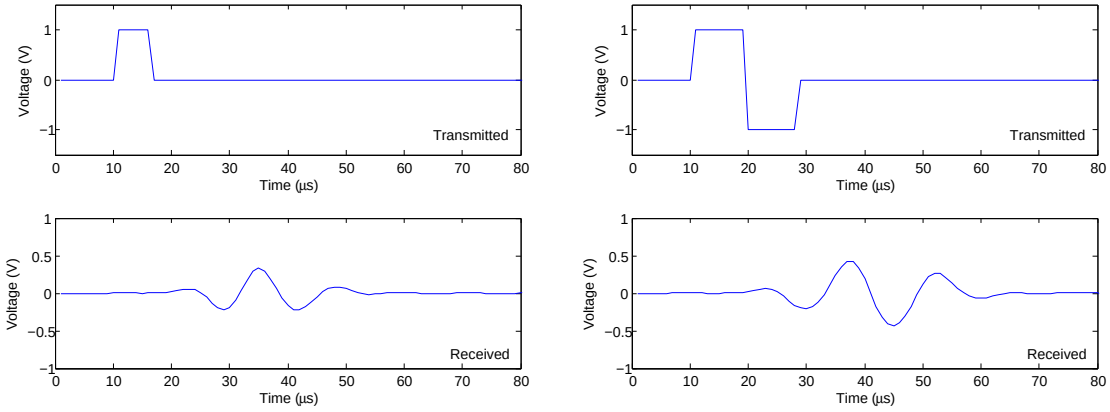

(a) Basis pulse No.1 - $x_1(n)$ (b) Basis pulse No.2 - $x_1(n)$

Figure 4.23: The two basis pulses used to test channel linearity

less than 3 ns for received signals with a nominal 200 ns amplitude – an error of less than 2%. The input signal amplitude range chose coincides with the pulse amplitudes used during operation of the communication system. This test indicates that with the chosen signals, homogeneity is a good working assumption for the ultrasonic channel.

Additivity The set of input signals $x[n] = x_1 + x_2[n - \delta]$ for $\delta \in [-400, \ldots, 400]$ ns was sent through the channel and the output $y[n]$ was recorded. For each input, the signal $\hat{y}[n] = y_1 + y_2[n - \delta]$ was generated, and the *error signal* $e[n] = \hat{y}[n] - y[n]$ was calculated. In this test as well, the error signal's peak amplitude was less than 2% for all input signals, indicating that with these test signals additivity is a reasonable assumption for the ultrasonic channel. Figure 4.24 shows a snapshot of this experiment. The transmitted signal is the sum of $x_1[n]$ and $x_2[n - 500\text{ ns}]$. The actual output from the ultrasonic channel ($y[n]$) and the expected output ($\hat{y}[n]$) coincide very closely.

Taken together, the test results above indicate that the linear channel model in Equation 4.15 matches the response of the physical system to within 2% *with respect to the test inputs chosen.* As with any physical system, we cannot prove linearity from

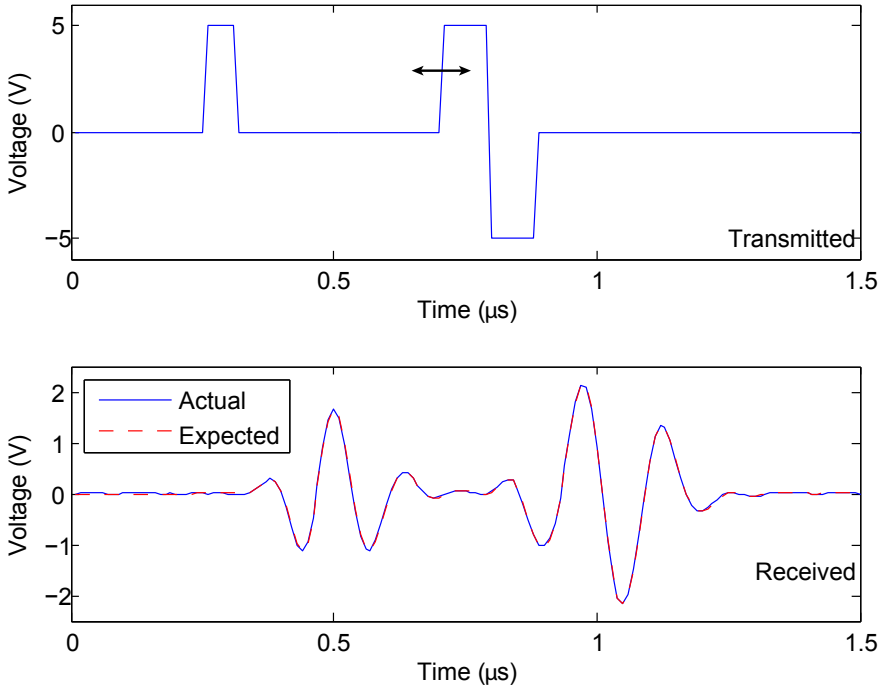

Figure 4.24: The sum of the two shifted basis pulses is used to test additivity

testing input-output pairs. However, linearity for the set of signals we have tested appears to be a good working assumption.

5. Basic Transceiver Designs

In Chapter 2, the echo characteristics of the ultrasonic channel, and the intersymbol interference they cause, were introduced. Subsequently these effects were captured with the mathematical models developed in Chapter 4. In the current chapter, the design of *pulse amplitude modulated* (PAM) transceivers sending *baseband* data will be considered, and the design issues relevant to reliable communication with this scheme are discussed. The transceiver design techniques presented in this chapter do not attempt to eliminate ISI (which would require the use of a channel equalizer), but rather operate in the presence of ISI. These transceiver designs result in low hardware/computational complexity, but intersymbol interference limits their data throughput. In the next chapter, more advanced transceiver designs will be considered that use various equalization techniques to suppress echoes and achieve much higher data throughput. The high-speed operation of these transceivers comes at the expense of higher hardware/software complexity.

Ultrasonic through-metal communication systems are finding use in a wide variety of applications. Some require high throughput, while others require low power consumption. The motivation for developing multiple transceiver designs – ranging from low complexity, low power to high complexity, high throughput – is so that the best design can be matched to each application.

5.1 Communication System Model

Consider an *echo free* ultrasonic communication channel. When it is excited with a narrow pulse (e.g., the 60 ns, 5 V pulse that has been used previously), the resonant characteristics of the transducers produce an oscillatory output signal that can

be approximated as a *Gaussian pulse* (see Section 4.2.2) – the product of a sinusoidal *carrier* and an Gaussian *envelope*. Data can be transmitted on a series of such transmitted pulses by modulating some pulse parameter (amplitude, width, position) using the incoming data. Figure 5.1 illustrates data transmission over an ideal (noiseless, distortionless, zero-ISI) channel using eight level pulse amplitude modulation (8-PAM). For each transmitted symbol, one Gaussian pulse is received. The amplitude of the received pulse encodes the data being transmitted. In this example, the sequence [7 1 4 6 2] has been transmitted.

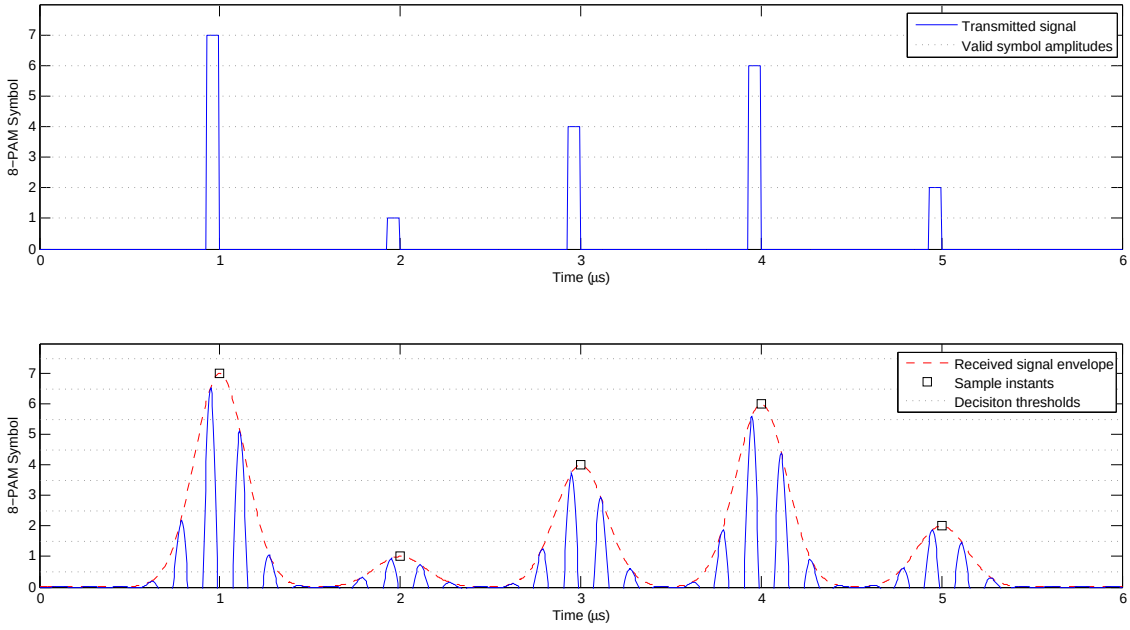

Figure 5.1: PAM received over an ideal ultrasonic channel

Using M-ary PAM, all of the signal's information content is encoded in the amplitude of received signal – the amplitude takes one of M values. In this chapter, we model transmission of symbols through the ultrasonic channel as *baseband PAM* transmission using *Gaussian pulse shaping*. Furthermore, the receiver will be *incoher-*

ent, using an envelop detector, such that only the amplitude (and not the sign) of the transmitted pulse can be discerned. In the next chapter, more complex transmissions schemes will be investigated.

Figure 5.2(a) shows the equivalent channel model used to study PAM communication thought the ultrasonic channel. Incoming symbols A_m are sent through a *transmitting filter/pulse shaper* G_t that maps each symbol into a Gaussian pulse of appropriate amplitude. The Gaussian pulses pass through the channel H_c, which induces echoes. The signal emanating from the channel then passes through a *receiving filter* G_r. Finally, the signal passes through a *detector* that samples the received signal in synchronization with the transmitted symbol rate, and maps each sample to one of the M transmitted symbols. The output of the channel is the estimate $\hat{A}_m$ of the transmitted symbol A_m.

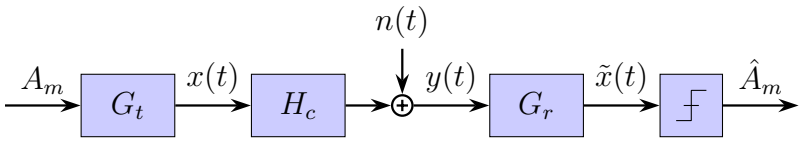

(a) Equivalent system model

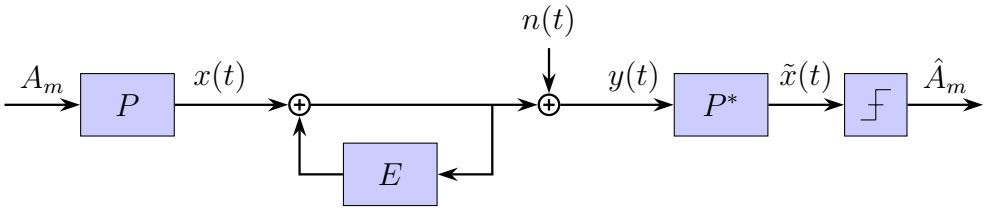

(b) Physical system components

Figure 5.2: Components of the PAM communication system

Figure 5.2(b) shows how the physical components of the communication system correspond to the model components. The ultrasonic channel's primary path transfer

function (P) acts as a pulse shaper, mapping rectangular pulses into Gaussian pulses of appropriate amplitude. The Gaussian pulse shape is not commonly used in PAM applications because it does not satisfy the Nyquest criterion for zero-ISI. It is being considered here, though, because it is the implemented naturally by the ultrasonic transducers. The communication channel H_c corresponds to the echo path transfer function (E). The receiving filter is matched to the Gaussian transmit filter, and thus has the transfer function P^*. Typically, additional filtering would be performed at the received to equalize the channel response. This may be combined with the matched filter, or placed in cascade. The focus of this chapter is on *basic* receiver techniques that provide reliable communication without the use of equalization, so this block is not present in the current model.

5.2 Intersymbol Interference

When Nyquest pulses are transmitted over an ideal channel, the received signal amplitude *at each sampling instant* corresponds exactly to one of the M transmitted symbol amplitudes. Graphically, these amplitude values are located midway between the decision thresholds in Figure 5.1. In a non-ideal channel – one containing noise and interference – these sampled values will not correspond exactly to the ideal values. In the presence of AWGN, the optimal PAM detector is the maximum likelihood (ML) detector (assuming all symbols are equally likely). Upon sampling the received signal at the symbol instant, the ML detector assigns to that sample the closest valid symbol value. Figure 5.3 illustrates transmission of the same symbol sequence that was used in Figure 5.1, but over a channel containing ISI. The transmitted sequence [7 1 4 6 2] would be incorrectly interpreted by the receiver as [7 1 3 6 1]. ISI has caused decision errors in the third and fifth received symbols.

Despite the severe ISI in the ultrasonic channel, a low complexity transceiver

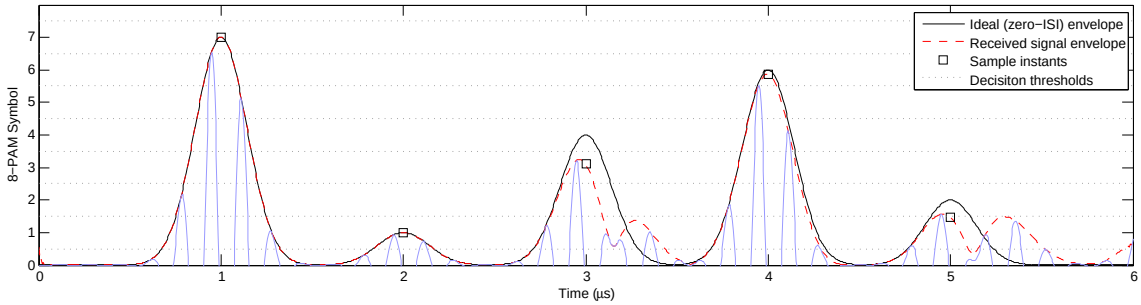

Figure 5.3: PAM received over non-ideal ultrasonic channel, contains ISI

may still achieve reliable communication by transmitting symbols at a rate "low enough" that the echoes from successive symbols have decayed sufficiently that they have negligible impact on one another. In this low noise environment, it is possible to encode multiple bits per symbol. As the number of bits per symbol increases, however, sensitivity to echo ISI also increases. It is therefore necessary to understand the echo decay characteristics of the channel, and relate those to the maximum ISI for a given symbol rate. From this, bit rate can be optimizes as a function of symbol rate and number of bits per symbol.

The simulation results in Figure 5.4 show the interference measured at the output of the ultrasonic channel as a function of symbol rate. The symbol rate t_s is swept from 0.4 μs to 10.0 μs. At each step, a random 100 symbol sequence is transmitted thought the channel and the ISI level is measured at the receiver. The lowest signal-to-ISI ratio (SIR) is reported for each time step. The channel simulation model used here was extracted from a physical ultrasonic channel whose round trip echo period is $t_r = 2.21\,\mu s$, using the procedure presented in Chapter 4.

The simulation shows several interesting results. First, at multiples of the echo round trip time (2.21 μs, 4.42 μs, 6.63 μs,...), the SIR is particularly low. Second, the ISI varies greatly as t_s varies from one multiple of t_r to the next, and at specific symbol rate SIR is very high (e.g., 40 dB at $t_s = 4\,\mu s$). In general, the interference

phenomena in the channel are difficult to describe analytically, but in the following sections, the dependency of ISI on symbol period will be investigated, and analytical bounds will be established to describe the *worst case ISI*.

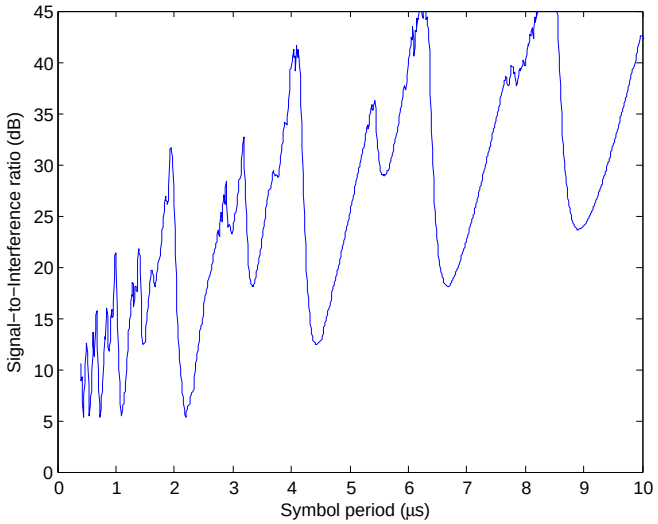

Figure 5.4: The measured ISI varies significantly with symbol rate

5.3 Echo Decay Envelope

In Chapter 4, the ultrasonic channel was decomposed into a *primary* path and an *echo* path. With respect to the communication system shown in Figure 5.2, the primary path accounts for pulse shaping (modeled in G_t), and the echo path accounts for ISI (modeled in H_c). The n-th symbol to be transmitted produces the baseband pulse $x_n(t)$ at the pulse shaper output,

$$s_m(t) = A_m\, p(t) = m \cdot p(t), \quad \text{for } m \in \{0,\, 1,\, \ldots,\, M-1\}, \tag{5.1}$$

$$x_n(t) = s_{m[n]}(t - n\, t_s) = m[n]\, p(t - n\, t_s). \tag{5.2}$$

where $s_m(t)$ is the baseband pulse encoding the m-th symbol from the M-ary family. Its amplitude is A_m and it is derived from the basis pulse shape $p(t)$. In this discussion $p(t)$ is a Gaussian pulse, but is often a Nyquist (or root Nyquist) pulse. The amplitude of A_m is m. The waveform $x_n(t)$ is the baseband pulse transmitted at the n-th symbol instant.

In Equation 4.14 it was show that the amplitudes of successive echo pulses are related to one another by the recursion $a[i+1] = |\Gamma|^2 a[i]$, where $a[i]$ is the amplitude of the i-th received echo pulse and Γ is the reflection coefficient between the bulkhead and transducer. Using this, the output of the channel in response to a single baseband PAM pulse is

$$y_n(t) = \sum_{i=0}^{\infty} |\Gamma|^{2i}\, x_n(t - it_r) = m[n] \sum_{i=0}^{\infty} |\Gamma|^{2i}\, p(t - it_r - nt_s). \tag{5.3}$$

The output of the channel is a series of exponentially decaying pulses spaced by the bulkhead's round-trip time t_r. Our goal is to develop a relationship describing the envelope of this decaying pulse train. Provided that the transmission filter's output pulse satisfies

$$\begin{aligned} &p(0) = 1, \\ &p(t) = 0, && \text{for } |t| > t_r/2, \\ &p(t) \in \mathbb{R} < 1, && \text{otherwise,} \end{aligned}$$

the echoes comprising $y_n(t)$ do not overlap, and the output of the channel at $t = nt_s$ is $m[n]$, the amplitude of the symbol transmitted at that time instant. Figure 5.5 shows the first three echoes that emanate from the acoustic channel in response to the isolated symbol $m[1] = 1$. The pulse shape $p(t)$ satisfies the requirements above, and successive pulses decay in an exponential manner described by Equation 5.3.

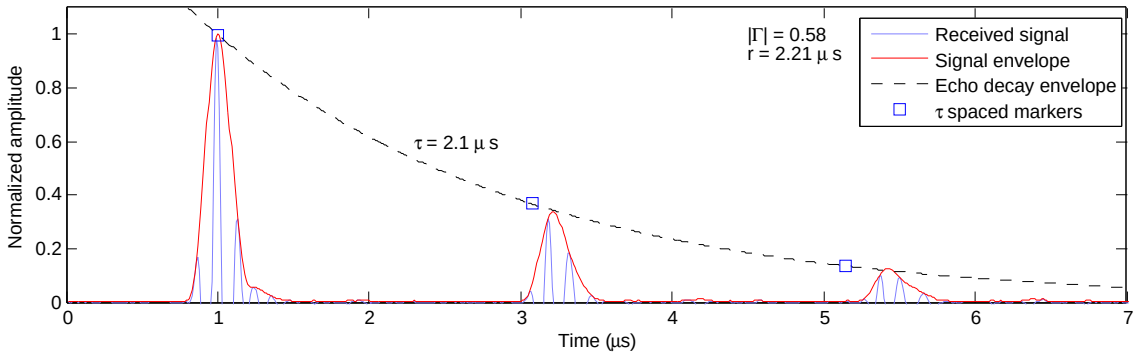

Figure 5.5: The channel echoes exhibit an exponential decay

To develop an equation for the bounding *echo decay envelope*, we sample $y_n(t)$ at a period equal to the bulkhead's round-trip time t_r, yielding

$$\begin{aligned} y_n(t = jt_r + nt_s) &= m[n] \sum_{i=0}^{\infty} |\Gamma|^{2i}\, p([jt_r + \cancel{nt_s}] - it_r - \cancel{nt_s}), \quad \text{for } j \in 0, 1, 2, \ldots \\ &= m[n] \sum_{i \neq j} |\Gamma|^{2i}\, \cancel{p(jt_r - it_r)} + m[n]|\Gamma|^{2j}\, p(0) \\ &= m[n]|\Gamma|^{2j} \end{aligned} \tag{5.4}$$

These samples represent points *on* the exponential decay envelope, denoted $y_{\text{env}}(t)$ and shown in Figure 5.5. Equating $y_{\text{env}}(t)$ to the sampled points in Equation 5.4 and applying the transformation $j = (t - nt_s)/t_r$ yields

$$y_{\text{env-}n}(t) = m[n]|\Gamma|^{2(t-nt_s)/t_r} = m[n]\, e^{-(t-nt_s)/\tau}, \quad \text{for } t \geq nt_s, \tag{5.5}$$

from which, the relationship $|\Gamma|^{2/t_r} = e^{-1/\tau}$ is implied. Solving for τ allows us to

express the echo decay envelop as a decaying exponential in the more familiar form,

$$y_{\text{env-}n}(t) = \begin{cases} m[n]\, e^{-(t-nt_s)/\tau}, & \text{for } t \geq n\, t_s \\ 0, & \text{for } t < n\, t_s \end{cases} \quad \text{where } \tau = \frac{-t_r}{2\ln|\Gamma|} \tag{5.6}$$

yielding the desired relationship between exponential decay envelope and the channel's characteristics – round trip time (t_r) and reflection coefficient (Γ). The exponential decay envelope shown in Figure 5.5 has a time constant of 2.1 μs. From equation 5.6, we see that the echo decay rate varies directly with bulkhead thickness and inversely with the reflection coefficient. Under good bulkhead-transducer matching ($\Gamma \approx 0$), very little energy is retained in the bulkhead and echoes decay rapidly. Similarly, as bulkhead thickness increases, the time between successive echoes increases, and the echoes take longer to decay.

Figure 5.6 shows the effect of reflection coefficient on the decay rate of the echo envelop. The echo decay time constant is normalized with respect to the round trip echo time (i.e., it is expressed as τ/t_r). For example, when $\Gamma = \sqrt{e^{-1}} \approx 0.61$, the decay

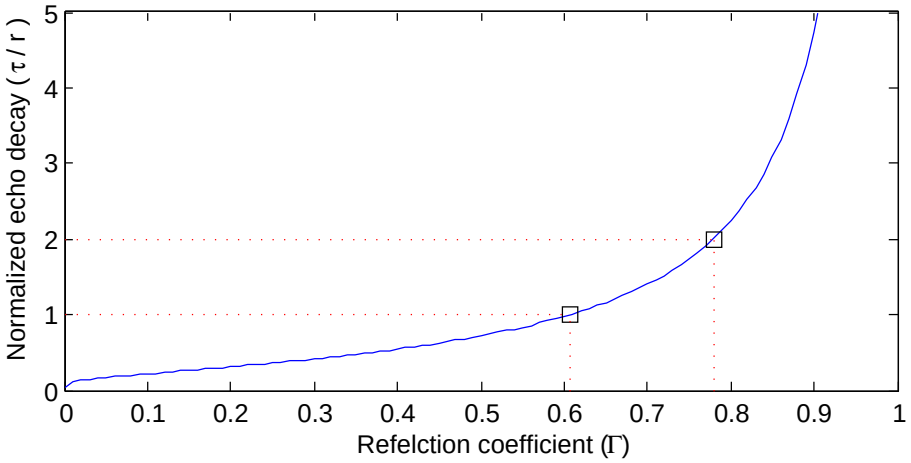

Figure 5.6: The echo decay time constant as a function of reflection coefficient

time constant is equal to one round trip time period ($\tau = t_r$); when $\Gamma = \sqrt[4]{e^{-1}} \approx 0.78$, the decay time constant is equal to two round trip time periods ($\tau = 2\,t_r$). As $|\Gamma| \rightarrow 1$, the echo train takes infinitely long to decay. In our experimentation, typical values of Γ are in the range $[0.45, 0.55]$, giving decay time constants of $\tau \in [\,0.63\,t_r, 0.84\,t_r\,]$.

5.3.1 Worst Case ISI

For the ultrasonic channel having the transient response shown in Figure 5.5, the *maximum* ISI induced by a symbol received at $t = 0$ on a symbol sampled at some $t > 0$ is given by Equation 5.6. When a sequence of symbols is transmitted, the ISI experienced at time t is the sum of the ISI components contributed by *all* previously received symbols. For a sequence of symbols beginning at $t = \text{-}\infty$ and having period t_s, the received signal sampled *at time zero* can be expressed in terms of the symbol being received at time zero and the worst case ISI present at time zero due to all previously received symbols, given in Equation 5.7.

$$\begin{aligned} y_{\text{env}}(0) &= \sum_{n=\text{-}\infty}^{0} y_{\text{env-}n}(0) = \sum_{n=\text{-}\infty}^{0} m[n]\; e^{nt_s/\tau} \\ &= m[0] + \sum_{n=1}^{\infty} m[\text{-}n]\; e^{\text{-}nt_s/\tau} \\ &= m[0] + I_{\text{env}}[t_s, \boldsymbol{m}] \end{aligned} \tag{5.7}$$

The term $I_{\text{env}}[t_s, \boldsymbol{m}]$ gives the worst case ISI that results from transmission of the sequence $\boldsymbol{m}$, i.e. $m[\text{-}\infty], ..., m[\text{-}2], m[\text{-}1]$, at a symbol rate t_s over a channel with echo decay constant τ. The worst case ISI is different for each transmitted sequence $\boldsymbol{m}$, and we are interested in finding the sequence $\bar{\boldsymbol{m}}$ that maximizes the worst case ISI. For the PAM symbol alphabet whose *normalized* symbol amplitudes are uniformly distributed between 0 and 1, the sequence $\bar{m}[n] = 1$ for $n \in \{\text{-}\infty, ..., 0\}$ maximizes

the worst case ISI.

$$\begin{aligned}\bar{I}_{\text{env}}[t_s, \bar{\boldsymbol{m}}] &= \sum_{n=0}^{\infty} m[\text{-}n]\ e^{\text{-}nt_s/\tau} - m[0] \\ &= \sum_{n=0}^{\infty} e^{\text{-}nt_s/\tau} - 1 \\ &= \frac{1}{1 - e^{\text{-}t_s/\tau}} - 1 \end{aligned} \tag{5.8}$$

Figure 5.7 shows the same measured signal-to-interference ratio presented earlier, with the exponential worst case bound overlayed. As expected, the symbol rates that are at multiples of the round trip time correspond to points on the exponential bound curve, and give rise to especially high ISI. In general, however, the bound in Equation 5.8 underestimates the actual ISI present at particular symbol rates. Its simplicity nonetheless makes it a convenient, closed form bound. In Section 5.5, this ISI bound will be used to determine an upper limit on the achievable data rate in this equalizer free communication system.

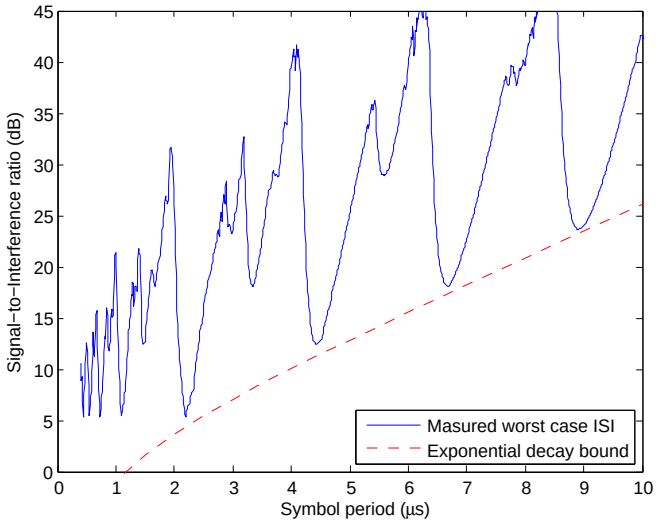

Figure 5.7: The signal-to-interference bound for the exponential decay approximation compared to the measured value

5.4 Symbol/Echo Synchronization

The analysis in the previous section provided an ISI bound that approximated the decaying pulse train phenomenon as an exponentially decaying envelope. This bound is convenient because it is dependant only on the time constant of the echo decay, but in general it is very conservative. The echoes found in the ultrasonic channel are different from the ISI found in most hardwired and wireless channels in that they are well structured – characterized by an *exponentially decaying* series of *equally spaced* pulses. Only when the data symbols are sent at a rate equal to some multiple of the echo period does the ISI experienced approach that predicted by Equation 5.8. By interleaving the transmitted symbols with channel echoes, ISI can be greatly reduced, and data rate can be increased.

The design of the communication system in this chapter has assumed the use of a Gaussian symbol shaping filter, due to the approximately Gaussian response of the ultrasonic transducers to a rectangular excitation pulse. While the Gaussian pulse does not satisfy the Nyquist criterion, the pulse does decay rapidly, so in an *echo free* environment, ISI from adjacent primary pulses can be controlled by proper selection of symbol period. The illustration in Figure 5.1 shows an example where symbol spacing is sufficient to ensure low ISI. Strictly speaking, the Gaussian pulse is infinite duration, but in practice, some time interval t_p can be found such that the pulse shaping filter's response is essentially zero outside of that interval.

$$\begin{aligned} &p(0) = 1 \\ &p(t) \approx 0, && \text{for } |t| > t_p/2, \\ &p(t) \in \mathbb{R} < 1, && \text{otherwise} \end{aligned} \tag{5.9}$$

We begin by expressing the bulkhead's round-trip time t_r and symbol period t_s as integer multiples of the *time slot width*, t_w. Let k_r denote the number of time slots between each echo, and k_s denote the number of time slots between each transmitted symbol. If a common factor g exists between the two, it is factored out to give $\widetilde{k_r}$ and $\widetilde{k_s}$, respectively.

$$t_r = k_r\, t_w, \qquad t_s = k_s\, t_w, \qquad \text{where } k_r = \left\lfloor \frac{2\, t_r}{t_p} \right\rfloor \tag{5.10}$$

$$k_r = g\, \widetilde{k_r}, \qquad k_s = g\, \widetilde{k_s}, \qquad \text{where } g = \mathrm{GCF}(k_r, k_t) \tag{5.11}$$

Due to the choice of t_w, the i-th echo resulting from a pulse transmitted at time zero is centered within the ik_r-th time slot. Furthermore, the n-th symbol is transmitted within the nk_s-th time slot. Since the Guassian pulse width is less than the time slot width ($t_w \geq t_p$), an echo only interferes with a symbol if they are centered in the same time slot. Figure 5.8 illustrates the concept with $k_r = 6$ and $k_s = 5$. The exponentially decaying pulse train from the symbol transmitted at $t = 0$ is spaced at multiples of six time slots. If symbols are transmitted every five time slots, we see that interference occurs in time slot thirty, between the sixth transmitted symbol and the *fifth* echo of symbol zero.

Figure 5.9 shows the same ultrasonic channel, but now when transmitting at a symbol rate of $k_s = 3$. At this symbol rate, there is interference between the second transmitted symbol and the *first* echo, leading to much stronger ISI than was present in the prior example. The relationship between k_s and k_s dictates the way in which symbols and echoes interact. Our goal is to develop a relationship between the parameters k_s and k_s, and the worst case ISI that results. From this, we can determine the symbol period that maximizes data rate.

These examples only illustrate the interference between a pair of symbols. In

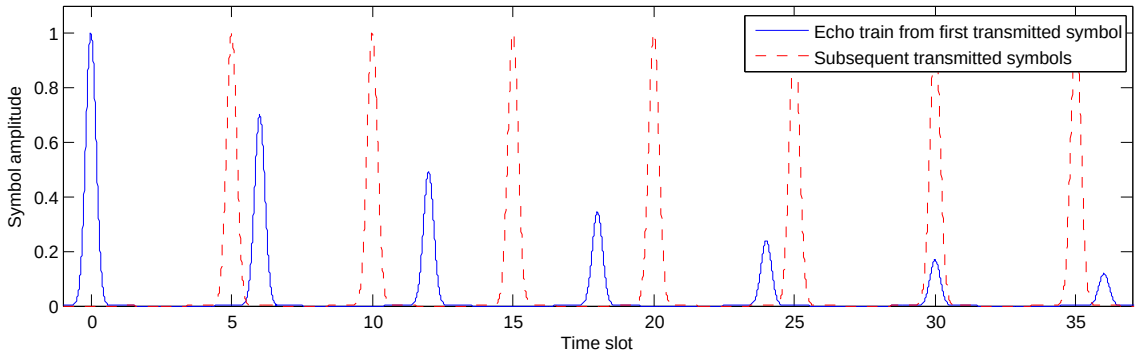

Figure 5.8: Interleaving symbols between echoes with $t_r = 6\,t_p$, $t_s = 5\,t_p$. Interference at fifth echo.

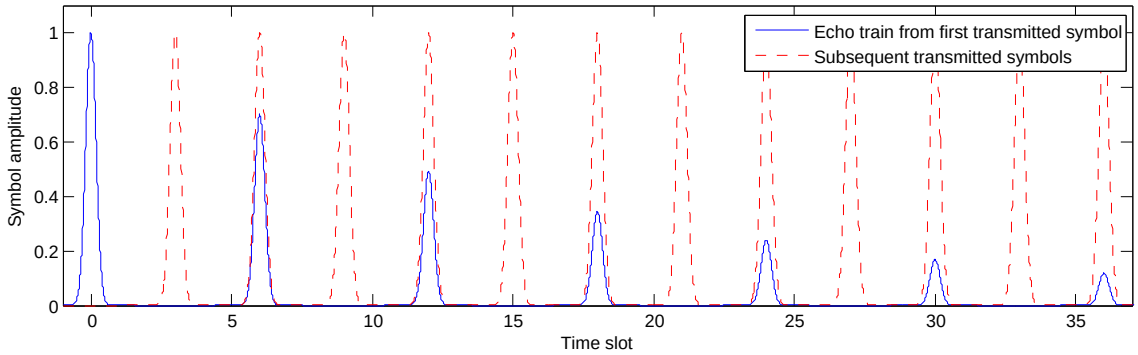

Figure 5.9: Interleaving symbols between echoes with $t_r = 6\,t_p$, $t_s = 3\,t_p$. Interference at first echo.

general, a series of data symbols will be transmitted, each yielding its own decaying echo train. As a result, the ISI experienced by a symbol is a function of *all* symbols that precede it.

5.4.1 Worst Case ISI

In Section 5.2, the equation $y_n(t)$ was developed to describe the received pulse train that results from transmitting the symbol $m[n]$. The decaying pulse train was the approximated by a bounding exponential $y_{\text{env-}n}(t)$ and used to derive a simple

upper bound on channel ISI. Beginning again with the equation for $y_n(t)$, a tighter ISI bound can be formed by accounting for the "symbol-echo synchronization" effect seen in Figure 5.8.

$$y_n(t) = m[n] \sum_{i=0}^{\infty} \alpha^i \, p(t - it_r - nt_s), \quad \text{where } \alpha = |\Gamma|^2$$

The received signal at any time is the superposition of the individual received signals for all past transmitted symbols. Equation 5.12 describes the maximum amplitude of the channel output at $t = 0$ for a particular symbol sequence $\boldsymbol{m}$. The time indices have been written in terms of the time slot width t_w, and the round trip and symbol slot spacings k_r and k_s, respectively.

$$\begin{aligned} y(0) = \sum_{n=-\infty}^{0} y_n(0) &= \sum_{n=-\infty}^{0} m[n] \sum_{i=0}^{\infty} \alpha^i \, p(-i\,t_r - n\,t_w) \\ &= \sum_{n=-\infty}^{0} m[n] \sum_{i=0}^{\infty} \alpha^i \, p(-i\,k_r\,t_p - n\,k_s\,t_w) \\ &= \sum_{n=0}^{\infty} m[-n] \sum_{i=0}^{\infty} \alpha^i \, p([k_s\,n - k_r\,i]\,t_w) \end{aligned} \tag{5.12}$$

Since the quantity $[k_s\,n - k_r\,i]$ assumes only integer values, the non-overlap constraint of Equation 5.9 means that $p([k_s\,n - k_r\,i]\,t_p)$ is non-zero only for $[k_s\,n - k_r\,i] = 0$, or equivalently for *integer values* of $i = n \cdot k_s/k_r$. The integer values of this equation occur only at values of $n = \widetilde{k_r}\,j$ for $j \in \mathbb{Z}$. Upon substituting $n = \widetilde{k_r}\,j$ and $i = \widetilde{k_s}\,j$, Equation 5.12 can be rewritten as

$$\begin{aligned} y(0) &= \sum_{j=0}^{\infty} m[\text{-}\widetilde{k_r}\,j] \; \alpha^{\widetilde{k_s}\,j} \; p(0) = \sum_{j=0}^{\infty} m[\text{-}\widetilde{k_r}\,j] \; \alpha^{\widetilde{k_s}\,j} \\ &= m[0] + \sum_{j=1}^{\infty} m[\text{-}\widetilde{k_r}\,j] \; \alpha^{\widetilde{k_s}\,j} \\ &= m[0] + I[k_s, \boldsymbol{m}] \end{aligned} \tag{5.13}$$

Returning to the example in Figure 5.8, with $k_r = 6$ and $k_s = 5$, Equation 5.13 says that the amplitude of the channel output sampled at $t = 0$ is

$$y(0) = m[0] + m[\text{-}6]\,\alpha^5 + m[\text{-}12]\,\alpha^{10} + m[\text{-}18]\,\alpha^{15} + \cdots.$$

For the example in Figure 5.9, $k_r = 6$ and $k_s = 3$. Upon factoring out the common factor 3 from each, we have $\widetilde{k_r} = 2$ and $\widetilde{k_s} = 1$. The channel output at $t = 0$ is

$$y(0) = m[0] + m[\text{-}2]\,\alpha^1 + m[\text{-}4]\,\alpha^2 + m[\text{-}6]\,\alpha^3 + \cdots.$$

The first term in each summation represents the desired information symbol, $m[0]$, and the remaining terms represent intersymbol interference. In the first example, the ISI terms die with α^{5n}, while in the second, they die with α^n. In an M-level PAM system, *normalized* symbol amplitudes take values in the range [0 1]. The worst case ISI results when the infinite symbol sequence $\bar{m}[n] = 1$, for $n \in [\text{-}\infty\ 0]$, is transmitted. The worst case ISI at $t = 0$ can then be expressed as

$$\begin{aligned}
\bar{I}[k_s, \bar{\mathbf{m}}] &= \sum_{j=1}^{\infty} \bar{m}[\text{-}\widetilde{k_r}\,j]\ \alpha^{\widetilde{k_s}\,j} - m[0] \\
&= \sum_{j=1}^{\infty} \alpha^{\widetilde{k_s}\,j} - 1 \\
&= \frac{1}{1 - \alpha^{\widetilde{k_s}\,j}} - 1
\end{aligned} \tag{5.14}$$

Equation 5.14 defines the *symbol-echo synchronous* ISI bound. It is interesting to compare the maximum ISI given by this equation to the maximum ISI predicted using the *exponential decay envelope* ISI bound. Upon expressing Equation 5.14 in terms of the continuous time variable t_s and expressing 5.8 in terms of $\alpha = |\Gamma|^2$, we

have

$$\bar{I}[t_s, \bar{\mathbf{m}}] = \sum_{j=0}^{\infty} \alpha^{\widetilde{k_r}\, t_s\, j/t_r} - 1 = \frac{1}{1 - \alpha^{\widetilde{k_r}\, t_s/t_r}} - 1 \tag{5.15}$$

$$\bar{I}_{\text{env}}[t_s, \bar{\mathbf{m}}] = \sum_{n=0}^{\infty} \alpha^{t_s\, n/t_r} - 1 \quad = \frac{1}{1 - \alpha^{t_s/t_r}} - 1. \tag{5.16}$$

Comparison of the two equations reveals that the ISI predicted by Equation 5.15 is less than or equal to that given by Equation 5.16, and that the two ISI bounds are equal only when symbols are transmitted at some integer multiple of the echo round trip time (i.e., $t_s = n\, t_r$ for $n \in \mathbb{Z}^+$), for which $\widetilde{k_r} = 1$.

Figure 5.7 compares the measured channel signal-to-interference ratio with that predicted from the bounds in Equations 5.15 and 5.16. In this example, echoes are spaced by two time slots (i.e., $k_r = 2$), with each time slot $t_w = 1.11\ \mu s$. The symbol-echo synchronous bound is only valid for symbol periods of $t_s = n\, t_w$ for $n \in \mathbb{Z}^+$. Again, we note that the two bounds are equal when $t_s = n\, t_r = 2\, n\, t_w$ for $n \in \mathbb{Z}^+$. When a symbol is transmitted in an intermediate time slot (one that is not a multiple of t_r), lower ISI levels can be realized.

In most wireless communication channels, interference is characterized as a random process. The structured nature of echoes in the ultrasonic channel allows us to treat them as deterministic, using one of the bounds established above. With this knowledge, we can then find bounds on the data rate supported by the ultrasonic channel based on desired bit-error rate.

5.5 Achievable Data Rate

The data rate supported by the ultrasonic channel is limited by two quantities, inter-symbol interference, and channel noise. To this point, we have only considered the former. In this section, the limiting effects of both quantities are considered, and

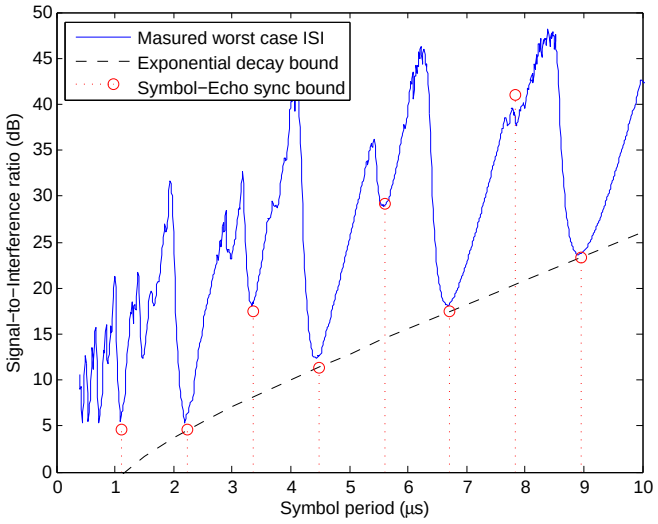

Figure 5.10: The ISI bound when considering symbol-echo synchronization

an optimization problem is formed to describe the achievable data rate as a function of reflection coefficient (which controls ISI) and signal-to-noise ratio.

5.5.1 PAM Error Rate in Ideal AWGN Channel

The M-ary PAM communication scheme transmits $k = \log_2 M$ bits of information per symbol, encoded in one of M waveforms. These waveforms are expressed as

$$s_m(t) = A_m\, p(t) = m \cdot p(t), \quad \text{for } m \in \{0,\, 1,\, \ldots,\, M-1\}. \tag{5.17}$$

All symbol waveforms are of identical shape, and the amplitude of the m-th waveform is A_m. The energy of $p(t)$, denoted E_p, is

$$E_p = \int_{-\infty}^{\infty} |p(t)|^2 dt. \tag{5.18}$$

If all symbols are transmitted with equal probability, the *average symbol energy* is given by

$$E = \frac{1}{M}\sum_{m=0}^{M-1} E_p\, A_m^2 = \frac{E_p}{M}\sum_{m=0}^{M-1} m^2 = \frac{2M^2 - 3M + 1}{6}\, E_p. \tag{5.19}$$

The *average bit energy* is defined as the average symbol energy divided by the number of bits conveyed per symbol, $E_b = E/k$. In terms of Equation 5.19, the average bit energy is

$$E_b = \frac{2M^2 - 3M + 1}{6\log_2 M}\, E_p. \tag{5.20}$$

When represented in vector form, the family of PAM signals can be viewed as a (one dimensional) signal constellation, shown in Figure 5.11. The figure shows the PDF of the amplitude of a received signal that results when transmitting the symbol $m = 2$ through an AWGN channel. The upper and lower tails (shaded) represent the probability of error for this channel.

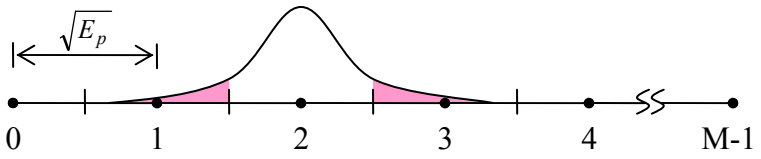

Figure 5.11: The PAM constellation

The error probability is influenced by two terms: the *variance* of channel noise, and the *minimum distance* between constellation points. The norm of a signal is

given by

$$||s(t)|| = \left(\int_{-\infty}^{\infty} |s(t)|^2 \, dt \right)^{1/2},$$

and the distance between two symbols is $||s_i(t) - s_j(t)||$. The minimum distance between constellation points is simply the distance between any two adjacent symbol waveforms.

$$\begin{aligned} d_{min} &= ||s_{i+1}(t) - s_i(t)|| \\ &= \left(\int_{-\infty}^{\infty} |s_{i+1}(t) - s_i(t)|^2 \, dt \right)^{1/2} \\ &= \left(\int_{-\infty}^{\infty} |[i+1] \cdot p(t) - i \cdot p(t)|^2 \, dt \right)^{1/2} \\ &= \left(\int_{-\infty}^{\infty} |p(t)|^2 \, dt \right)^{1/2} = \sqrt{E_p} \end{aligned} \tag{5.21}$$

Upon substituting Equation 5.20, d_{min} can be expressed in terms of E_b.

$$d_{min} = \sqrt{\frac{6 \log_2 M}{2M^2 - 3M + 1} E_b} \tag{5.22}$$

It can be shown [18] that the error probability of PAM signaling is expressed in terms of the minimum constellation distance and noise variance through Equation 5.23. Upon substituting for d_{min}, the error probability using unipolar PAM signaling can be expressed in terms of SNR (Equation 5.24) or SNR per bit (Equation 5.25).

$$P_e = 2 \left(1 - \frac{1}{M} \right) Q \left(\frac{d_{min}}{\sqrt{2 N_0}} \right) \tag{5.23}$$

$$= 2 \left(1 - \frac{1}{M} \right) Q \left(\sqrt{\frac{3}{2M^2 - 3M + 1} \frac{E}{N_0}} \right) \tag{5.24}$$

$$= 2 \left(1 - \frac{1}{M} \right) Q \left(\sqrt{\frac{3 \log_2 M}{2M^2 - 3M + 1} \frac{E_b}{N_0}} \right) \tag{5.25}$$

Figure 5.12 shows the symbol error performance of the signaling scheme for several values of M. The graph shows that for our system – with typical SNR in the $30 - 35$ dB range – 16-ary PAM can be used to achieve a symbol error rate of approximately 10^{-5}.

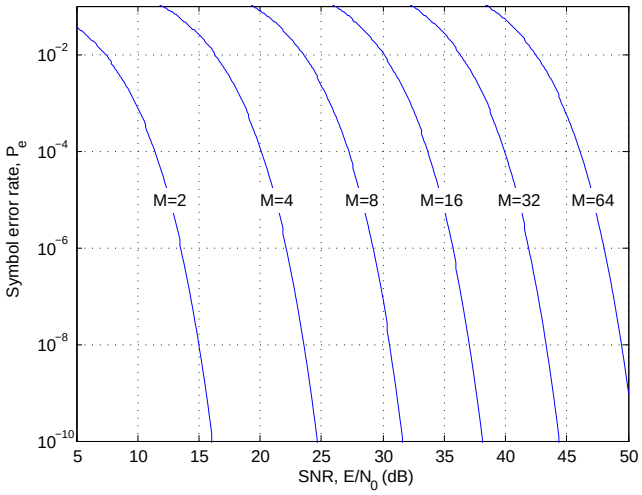

Figure 5.12: Bit error rate for unipolar PAM signaling

5.5.2 PAM Error Rate in Noisy ISI Channel

In the previous section, only the effects of noise were considered in deriving the symbol error rate for our signaling scheme. With the assumption of zero ISI, the derived error probability (Equation 5.25) was independent of symbol rate. When transmitting at very low symbol rates, the zero-ISI assumption is valid, but at high symbol rates, ISI must be considered when deriving channel error probability.

Figure 5.13 illustrates the effect of ISI using the exponential decay envelope bound if Equation 5.16. When symbols are transmitted at a rate equal to the echo decay time constant ($t_s = \tau$), the worst case ISI is $\bar{I}_{\text{env}}(\tau, \bar{\mathbf{s}}) = 0.58$. Consider 2-level PAM

transmission, with transmitted symbols having amplitudes of $A_m \in \{0, 1\}$. A decision error occurs when ISI causes the received symbol's amplitude to cross the detector's decision threshold of 0.5, which can happen only if $I > 0.1$. Clearly, the ISI present at this symbol rate can induce decision errors with 2-PAM transmission.

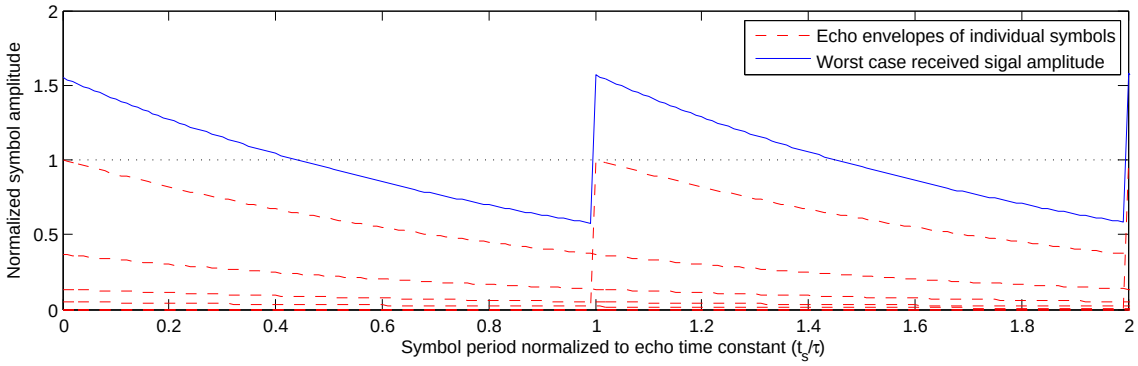

Figure 5.13: Worst case ISI when transmitting at symbol rate $t_s = \tau$

Next, consider symbols transmitted at a rate of $t_s = 4\tau$, shown in Figure 5.14. The maximum ISI possible here is $\bar{I}_{\text{env}}(4\tau, \bar{\mathbf{s}}) = 0.02$. At this low symbol rate, maximum ISI amplitude is quite small. In this section, we seek to develop a relationship that describes symbol error rate in terms of SNR *and* worst case ISI, or alternatively SNR and symbol rate.

Figure 5.15 shows the PAM constellation with shaded regions corresponding to the worst case ISI centered on each symbol value. Let d_{fs} denote the *full-scale symbol amplitude* used by the system. In terms of the minimum symbol distance ($d_{\min}$ given in Equation 5.22), the full scale symbol amplitude is $d_{\text{fs}} = (M - 1)\, d_{\min}$, as indicated in the figure. The worst case ISI equations given in Equations 5.15 and 5.16 describe ISI *normalized to the full-scale symbol amplitude*. The actual worst case ISI amplitude

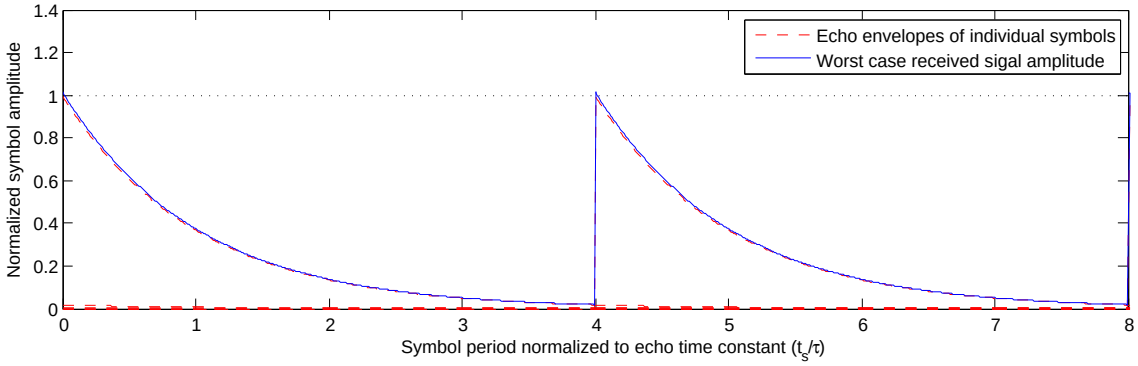

Figure 5.14: Worst case ISI when transmitting at symbol rate $t_s = 4\tau$

for a given symbol rate is given by

$$\tilde{I} = d_{\text{fs}}\, \bar{I} = (M-1)\, d_{\min}\, \bar{I} \tag{5.26}$$

$$= (M-1)\, \sqrt{E_p}\, \bar{I}. \tag{5.27}$$

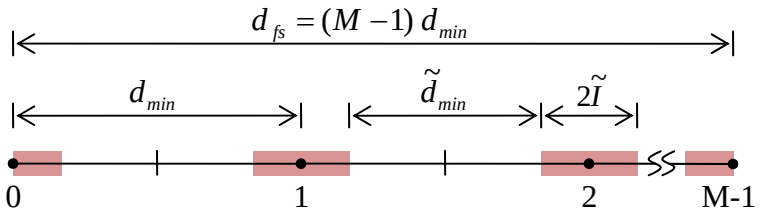

Figure 5.15: The PAM constellation showing ISI bounds

The presence of ISI reduces the effective distance between symbols. In an eye diagram, this is manifest as a closure of the eye in the vicinity of the sampling instant. For a given symbol distance d_{min}, an *effective* distance $\tilde{d}_{min}$ can be expressed in terms

of the ISI level.

$$\begin{aligned}\tilde{d}_{\min} &= d_{\min} - 2\,\tilde{I} \\ &= \sqrt{E_p} - 2\,\bar{I}\,(M-1)\,\sqrt{E_p} \\ &= [1 - 2\,\bar{I}\,(M-1)]\,\sqrt{E_p} \\ &= \beta\,\sqrt{E_p}, \quad \text{where } \beta = 1 - 2\,\bar{I}\,(M-1)\end{aligned} \tag{5.28}$$

The effective minimum distance is just $d_{\min}$ multiplied by some constant $\beta \leq 1$. Note that $\beta = 1$ only when no ISI is present, and can take *negative* values for high ISI or when the alphabet consists of a large number of symbols. A negative value of β indicates that worst case ISI will lead to (ISI induced) symbol errors. The symbol error probability can now be expressed in terms of both noise and ISI. The multiplier β inside the Q-function causes the bit error rate curve to shift to the right with increasing ISI level.

$$\begin{aligned}P_e &= 2\left(1 - \frac{1}{M}\right) Q\left(\frac{\tilde{d}_{\min}}{\sqrt{2\,N_0}}\right) \\ &= 2\left(1 - \frac{1}{M}\right) Q\left(\beta\,\sqrt{\frac{3}{2M^2 - 3M + 1}\,\frac{E}{N_0}}\right) \qquad (5.29) \\ &= 2\left(1 - \frac{1}{M}\right) Q\left(\beta\,\sqrt{\frac{3\log_2 M}{2M^2 - 3M + 1}\,\frac{E_b}{N_0}}\right) \qquad (5.30)\end{aligned}$$

Figure 5.16 shows two sets of curves generated for different ISI levels. Figure 5.16(a) shows that when the ISI level is 10%, only 2-ary and 4-ary PAM communication are supported by the channel. The ISI-free 4-ary BER curve is also shown. To maintain the error performance realized in the ISI-free channel using 4-PAM, an SNR increase of 8 dB is required. Figure 5.16(b) shows the effect of a 1% ISI level.

Alphabet sizes of up to $M = 32$ are supported. The SNR degradation here is significantly less; a 1 dB SNR increase is required to maintain the 4-PAM ISI-free BER performance.

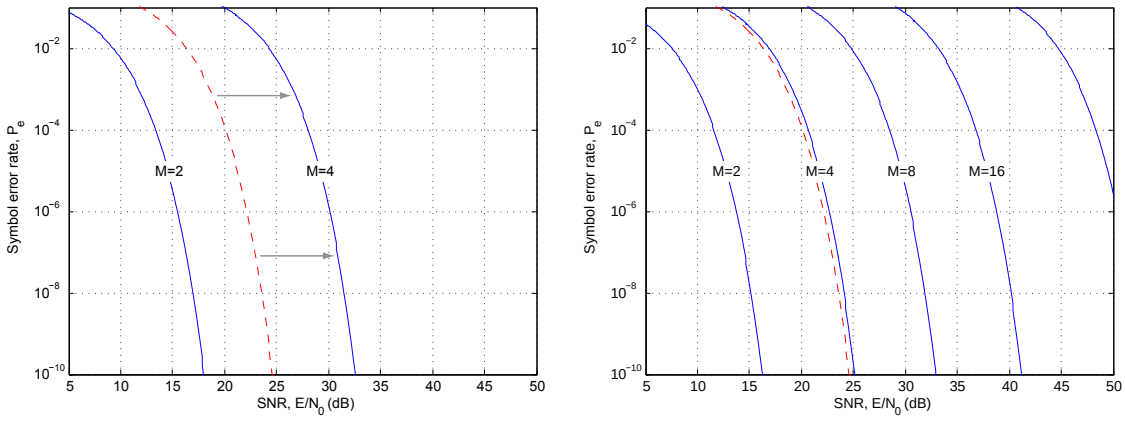

(a) 10% ISI amplitude (b) 1% ISI amplitude

Figure 5.16: Bit error rate degradation with increase in ISI level. ISI free $M = 4$ curve shown also.

5.5.3 Data Rate Optimization

The raw data rate through the ultrasonic channel is the product of the symbol rate ($f_s = 1/t_s$) and the number of bits conveyed per symbol (k).

$$R = k/t_s = k\, f_s \quad \text{where } k = \log_2 M \tag{5.31}$$

We have shown that as symbol rate increases, ISI also increases. We have also shown that the severity of ISI limits the size of the PAM alphabet (and therefore the size of k) that can be used. In this section, a systematic approach is presented to determine the optimal symbol rate (and resulting data rate) for the ultrasonic channel. The

optimization can be expressed as follows.

$$\begin{aligned} \underset{t_s}{\text{maximize}} \quad & R = k/t_s \\ \text{subject to} \quad & t_{s\text{-min}} < t_s < t_{s\text{-max}}, \quad \text{where } t_s \in \mathbb{R}^+ \\ & 1 \leq k \leq \left\lfloor \log_2\left(\tfrac{1}{2I} + 1\right) \right\rfloor, \quad \text{where } k \in \mathbb{Z}^+ \\ & I = f(t_s) \\ & P_e\left(\tfrac{E}{N_0}, k, I\right) < P_{e\text{-max}} \end{aligned} \tag{5.32}$$

The goal of the optimization is to determine the pair (t_s, k) that maximizes data rate while satisfying the error probability requirement, subject to a specified channel SNR and ISI characteristic. As posed in Equation 5.32, the data rate maximization can be solve directly using tools such as AMPL [59] or Matlab's Optimization Toolbox [60].

The optimization in Equation 5.32 is performed subject to four constraints. The first constraint specifies the allowable range of symbol periods over which to optimize. Using the exponential ISI bound, symbol rate varies continuously. Using the symbol synchronous bound, symbol period takes discrete values. Valid values of t_s are shown in Figure 5.10 for both bounds over the $0 - 10$ μs range. The second constraint specifies the allowable constellation sizes for a given ISI level. The upper value of k is just the largest k such that β in Equation 5.28 non-negative. The ISI level is a function of symbol period, specified by constraint three. The fourth constraint places a lower limit on the error probability of the transceiver, where its dependance on SNR, constellation size, and ISI level is explicitly noted.

Achievable Data Rate The optimization problem in Equation 5.32 is a function of two independent variables, the system's signal-to-noise ratio E/N_0 and the ISI as a function of symbol period. The ISI is, in turn, a function of the reflection

coefficient. As E/N_0 increases, so to does achievable bit rate. As Γ decreases, echo decay rate increases, and bit rate increases. Here, we look at the effect of each of these parameters individually on the maximum achievable channel bitrate. We use unipolar PAM signaling and a maximum error probability of 10^{-5}.

Effect of Signal-to-Noise Ratio First, the reflection coefficient is fixed at $\Gamma = 0.48$ and the E/N_0 is varied over the range $10 - 50$ dB. For each $(E/N_0, \Gamma)$ pair, the optimization in Equation 5.32 is carried out to yield the pair (t_s, k) that maximizes data rate. Figure 6.6 shows the minimum achievable data rate as a function of signal-to-noise ratio using both the exponential and synchronous ISI bounds (Equations 5.15 and 5.16 , respectively). As expected, the more conservative exponential bound predicts a lower achievable data rate than the synchronous bound.

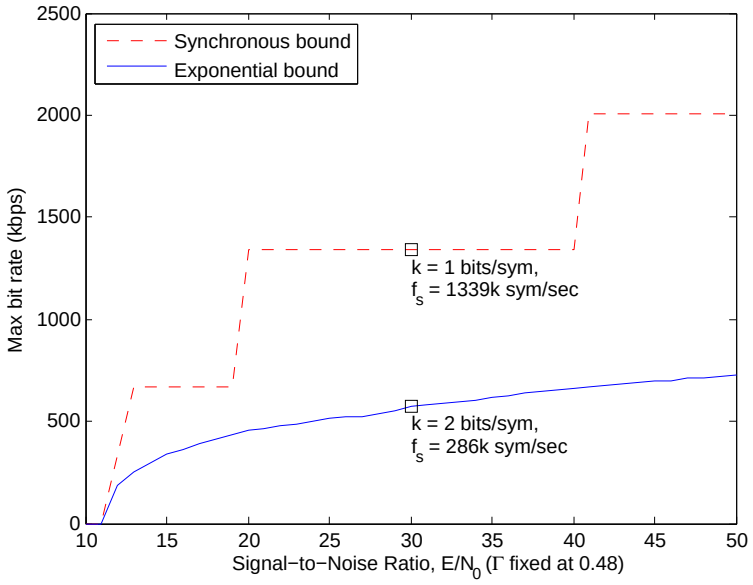

Figure 5.17: Bit rate as a function of SNR with Γ fixed at 0.48

According to the exponential bound, at a 30 dB SNR, the minimum achievable

bit rate is 572 kbps (2 bits/sym · 286 ksym/sec). The synchronous bound indicates a minimum bit rate of 1.34 Mbps (1 bit/sym · 1.34 M-sym/sec) at the same SNR.

Effect of Reflection Coefficient Next, E/N_0 is fixed at 30 dB and the reflection coefficient is varied over the range $0.20 - 0.80$. Figure 5.18 shows the minimum achievable data rate as a function of reflection coefficient, again using the exponential and synchronous ISI bounds. As expected, better transducer-bulkhead matching (smaller Γ) results in lower echo amplitude and higher achievable data rate. The same operating point shown in Figure 6.6 ($\Gamma = 0.48$, $E/N_0 = 30$ dB) is shown on this graph as well, and indicates the same achievable bit rate.

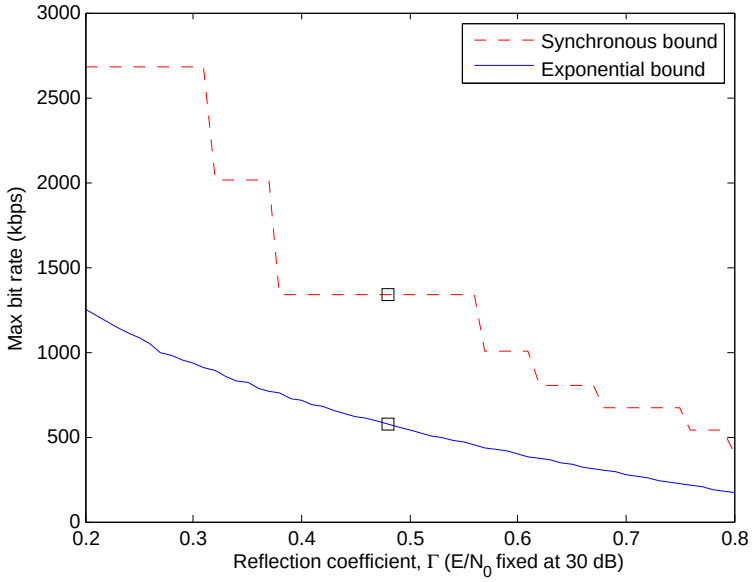

Figure 5.18: Bit rate as a function of Γ with SNR fixed at 30 dB

Simulation Results The results in Figure 6.6 indicate that a data rate of 1.4 Mbps can be achieved at a bit-error rate of 10^{-5} when t_s and k are chosen properly. This can

be verified using the channel simulation model with the aid of an *eye diagram*. Figure 5.19(a) shows the eye diagram generated by sending 200 random symbols thought the channel for $t_s = 0.75\,\mu$s and $k = 1$ bit. The interference results in some closure of the eye, but the remaining noise margin is sufficient to meet the BER requirement. Figure 5.19(b), on the other hand, shows the same symbol rate, but for $k = 2$ bits/sym. Here, the eye is completely closed, indicating that symbol errors will occur. Note that the data in Figure 6.6 also indicates that this $(t_s\, k)$ pair is not supported.

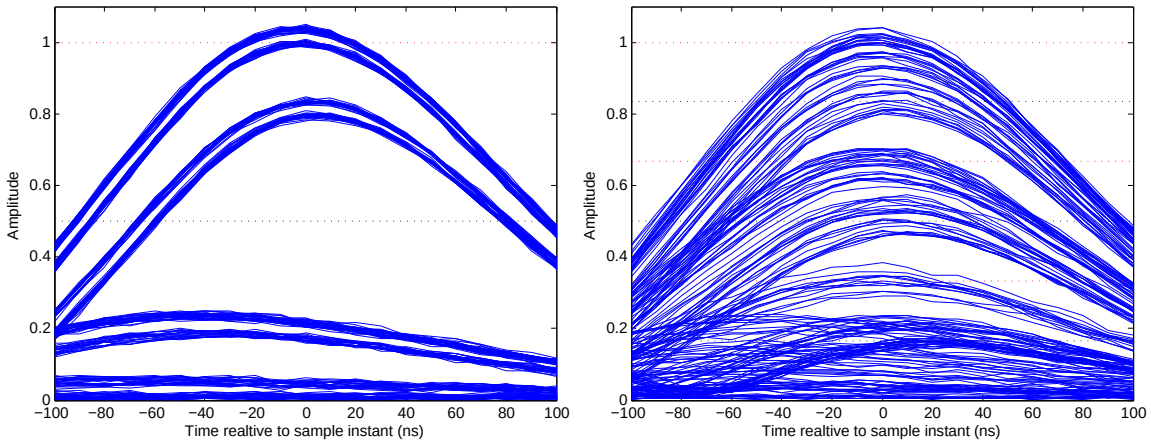

(a) $k = 1$ bit/symbol, eye open

(b) $k = 2$ bits/symbol, eye closed

Figure 5.19: Eye diagrams of PAM transmission at $f_s = 1338$k symbols/sec

5.6 Summary

In this chapter, techniques for designing reliable equalizer-free communication transceivers were presented. It is obvious that transmitting at a "low enough" symbol rate will mitigate the effects of echo induced ISI, and in this chapter we have provided numerical bounds to quantify this symbol rate. The motivation for considering such simple transceiver designs is that they translate into simple, low-cost,

low-power hardware implementations, making them ideal for battery powered or energy harvesting based systems.

The data rate in the presence of echoing was determined by first deriving bounds on the echo ISI as a function of symbol rate. The *exponential bound* requires knowledge only of the reflection coefficient between transducer and bulkhead. The *synchronous bound* requires determination of reflection coefficient, echo period, and pulse width, so its implementation is more difficult in practice. Furthermore, this method requires that the symbol rate can be precisely adjusted (to achieve synchronization with the echo period).

While the methods presented in this chapter represent a very simple set of transceivers, they should be considered in applications that require low data rates. In the following chapter, more complex equalizer-based designs will be developed for high data rate applications.

6. Advanced Transceiver Designs

The goal of the previous chapter was to present transceiver designs that resulted in very simple hardware/software implementations. Those designs simply *avoided* echo related intersymbol interference by transmitting at a sufficiently low data rate, or by interleaving transmitted symbols with echo pulses in a way that reduces the effective channel interference. While those techniques are ideal for low power, low bandwidth applications, the presence of ISI limits the channel bandwidth to a point well below the theoretical limit. Intersymbol interference in high-speed communication channels is traditionally addressed through the used of *channel equalizers*. In this chapter, several common equalization techniques are applied to ultrasonic transceiver design. In addition, we derive an equalizer based on the channel model developed in Chapter 4. The penalty paid for all of the techniques presented in this chapter is increased transceiver cost and complexity, but in applications where high data rates are required, this may be justified. The experimental and simulation results presented throughout this chapter were performed using the test setup presented Chapter 2 and channel model developed in Chapter 4.

6.1 Channel Model Based Equalizer

In Chapter 4, a block diagram of the ultrasonic channel (reproduced in Figure 6.1) was formed that decomposed the channel into a *primary path* and an *echo path*. It was shown that the primary path transfer function acts as a pulse shaper, and the echo path transfer function accounts for acoustic energy being reflected within the bulkhead. Once an estimate of the channel model is formed, it can be used to construct a simple equalizer. We begin by considering an equalizer that, when placed

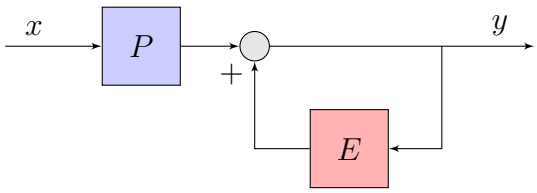

Figure 6.1: Ultrasonic channel model developed in Chapter 4

in cascade with the ultrasonic channel, causes complete cancelation of the *echo portion* of the channel response. In terms of the transfer functions of the equalizer (H_e) and the channel (H_c), the overall system transfer function (H) is

$$H = H_e H_c = P.$$

In other words, the transfer function of the composite system reduces to the transfer function of the *primary path*. Using Equation 4.3, the equalization filter that exactly cancels the channel echoes is given by

$$H_e = \frac{P}{H_c} = 1 - E, \tag{6.1}$$

which depends only on the *echo transfer function*, E. The block diagram of Figure 6.2 shows the interconnection of equalizing filter and channel. $\widehat{E}$ denotes the estimate of the actual echo transfer function E. Two approximations will be considered to form the model of $\widehat{E}$, each of differing complexity and effectiveness. The *simplified* echo path model assumes that E is an attenuator in cascade with an ideal delay element, i.e., the echoes that emanate from the channel are scaled, time delayed version of one another. The *improved* echo path model, on the other hand, models the dispersive effects of the channel in addition to the attenuation and delay characteristics. This model yields a superior equalization filter at the expense of greater transceiver

complexity.

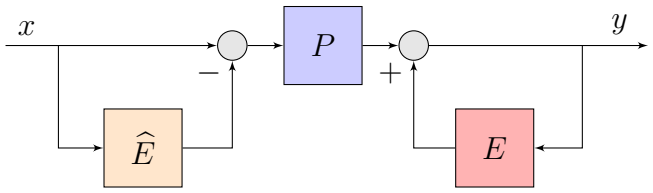

Figure 6.2: Construction of the predistortion filter

The echo transfer function, E, accounts for several phenomena experienced as an acoustic signal makes a single round trip through the bulkhead. A signal within the bulkhead, incident upon the receiving side, meets an impedance mismatch between the bulkhead wall and the receiving transducer. A portion of the energy is coupled to the transducer (appearing as a voltage at the output) and the remainder of the energy is reflected back within the bulkhead toward the transmitting transducer. As the signal travels through the bulkhead material, it is attenuated and dispersed. When the signal reaches the other bulkhead wall, it meets another impedance mismatch and again, a portion of the energy is coupled to the transducer while the remainder is reflected back toward the reverer side. This process continues until all acoustic energy is dissipated within the bulkhead or transducers.

As described, the bulkhead can be considered a cascade of several subsystems. In this analysis, we represent all of the effects described above by a cascade of an *ideal delay* and a *rational transfer function*. The delay element accounts for the round trip delay of acoustic signals, and the transfer function provides a lumped element approximation of all other magnitude and phase characteristics. The filter will be implemented in a digital signal processor, so we have chosen to describe it in discrete time form.

$$\widehat{E}(z) = \widehat{E}_l(z)z^{-r}$$
$$\widehat{H}_e(z) = 1 - \widehat{E}_l(z)z^{-r} \tag{6.2}$$

where z^{-r} denotes the round trip delay of acoustic signals (in samples) and $\widehat{E}_l(z)$ is the lumped element approximation of all other bulkhead effects. The remainder of this section discusses methods of building the equalizer from experimental data. Two equalizers are presented, based on two models of the echo transfer function of differing complexity and accuracy.

6.1.1 *Simplified* Echo Path Model

We begin by assuming that the echos in the ultrasonic channel are characterized by an exponentially decaying pulse train, i.e. successive echoes are equally spaced and differ in amplitude by a factor α. Under this assumption, Equation 6.2 reduces to

$$\widehat{H}_e(z) = 1 - \alpha\, z^{-r}, \tag{6.3}$$

requiring the estimation of two parameters, the decay constant α and the round trip echo delay r. A block diagram of the equalizer is shown in Figure 6.5. In the previous chapters, we have discussed the estimation of both the decay constant and round trip time. Figure 6.3 shows the effect of an equalizer derived from the basic channel model. Here, we assume that the equalizer is placed on the transmitting side of the channel, but it works identically when placed at the receiver side. The first curve in the figure shows that the equalizer's effect is to augment each transmitted pulse with a *cancelation pulse* whose time offset and amplitude correspond to the echo period and decay constant of channel echoes. The second curve shows the received signal that

results when no equalization is used, while the third curve shows the channel output when equalization is used. The effect of the cancelation pulse to cause destructive interference with and reduce the amplitude of channel echoes.

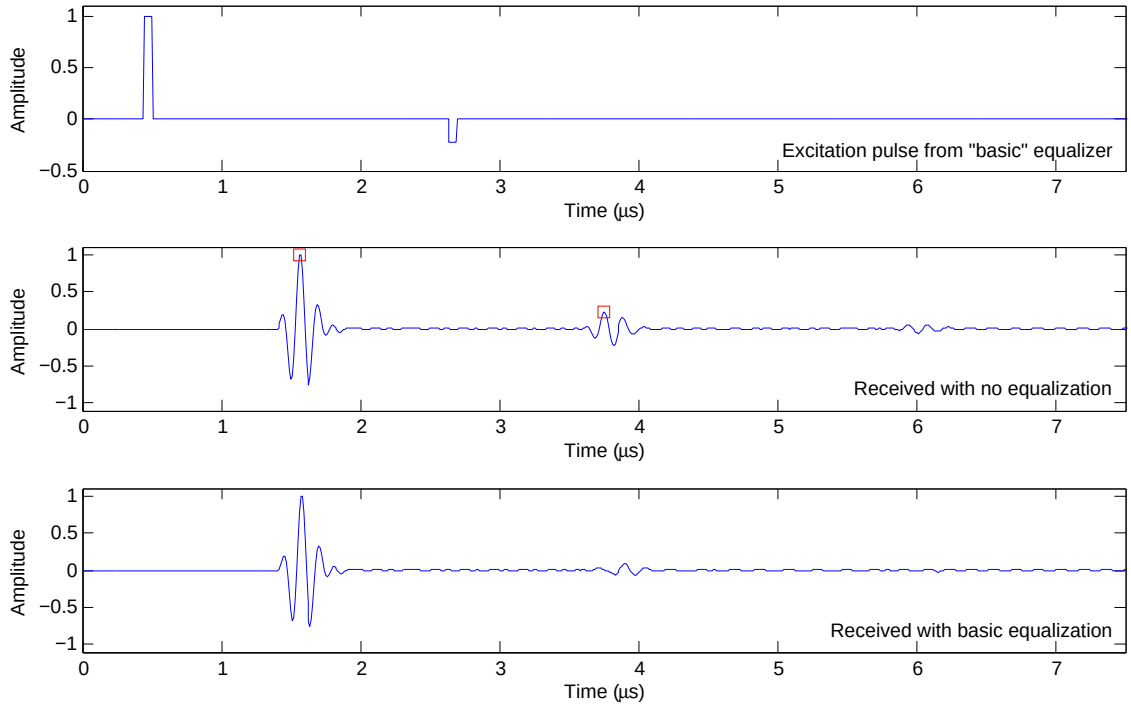

Figure 6.3: Echo suppression using equalizer derived from *simplified* channel model

The results of this experiment show that a residual echo is still present in the received signal. This is not surprising given the simplifying assumption made about the nature of channel echoes. Recall that the model developed in Chapter 4 treated $E_l(z)$ as a rational transfer function, where here we assume that it is a constant. Testing this technique on several bulkheads of varying thickness has shown that it typically results in an $8-10$ dB reduction in echo energy over the unequalized channel. The results in Figure 6.3 yield a reduction in echo energy of 9 dB.

In Chapter 5, a simulation of the channel's signal-to-interference ratio as a function

of symbol period was performed. Figure 6.4 shows these results along with results from the same test performed on the equalized channel. Comparing Figures 6.4(a) and 6.4(b), we see that the equalizer effectively shifts the curve up by 9 dB, corresponding the the 9 dB of echo energy suppression noted in Figure 6.3.

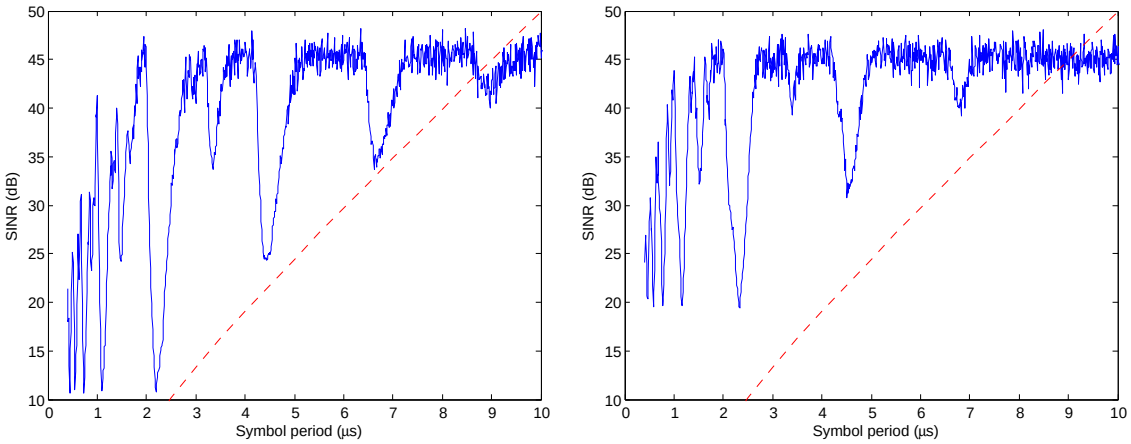

(a) Without equalization (b) Using "simple" equalizer

Figure 6.4: SINR improvement of 9 dB realized with *simplified* equalizer

The simplified channel model results in an equally simple equalizer structure, shown in Figure 6.5. The hardware implementation requires a digital delay line of length d and one multiplication per output sample, and the equalizer can be placed on either side of the channel. While the equalizer is less effective than alternatives discussed later in the chapter, the particularly simple implementation makes it suitable for hardware constrained systems.

Achievable Data Rate In Chapter 5, equations were developed to related the transmitted symbol rate to worst-case ISI amplitude in the ultrasonic channel. The function of the simplified equalizer is to cause destructive interference in the channel

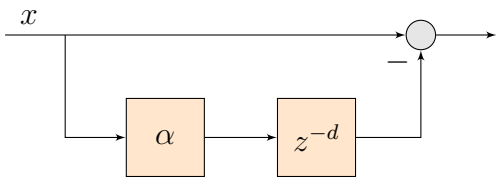

Figure 6.5: The implementation of the *simplified* equalizer

echoes. Effectively, the amplitude of the first echo is decreased, and all subsequent echoes decay with the same decay constant seen in the equalizer-free system. The ISI equations developed previously can be easily adapted to account for the effect of echo cancelation. The modified equations can then be used to determine the bitrates achievable using cancelation. The modified synchronous ISI bound, for example, is given by

$$\bar{I}_{eq}[t_s, \bar{\mathbf{m}}] = \frac{1}{1 - \beta\alpha^{\widetilde{k_r}\, t_s/t_r}} - 1, \tag{6.4}$$

where β is the *echo scaling factor*, the ratio of echo amplitude with cancelation to its amplitude when no cancelation is used. For example, $\beta = 0.5$ results in an equalized echo that is one half its original value. The echo suppression achieved in Figure 6.5 yield $\beta \approx 0.35$.

The bitrate optimization (Equation 5.32) can now be performed with this new relationship for channel ISI. Figure 6.6 shows the result of performing this optimization over the range $E/N_0 \in [10\ 50]$ dB, using the bound in Equation 6.4 and $\Gamma = 0.48$. The results from the prior chapter, where no equalization is used, are shown for comparison. Under channel conditions identical to those examined in the previous chapter, the *simplified* equalizer provides a doubling in data rate at $E/N_0 = 30$ dB. While the symbol period for the two strategies is the same ($0.75\,\mu$s, corresponding to transmission of one symbol during each time slot in Figure 5.8), the equalizer suppresses echoes sufficiently to allow the used of 4-PAM, encoding two bits per symbol.

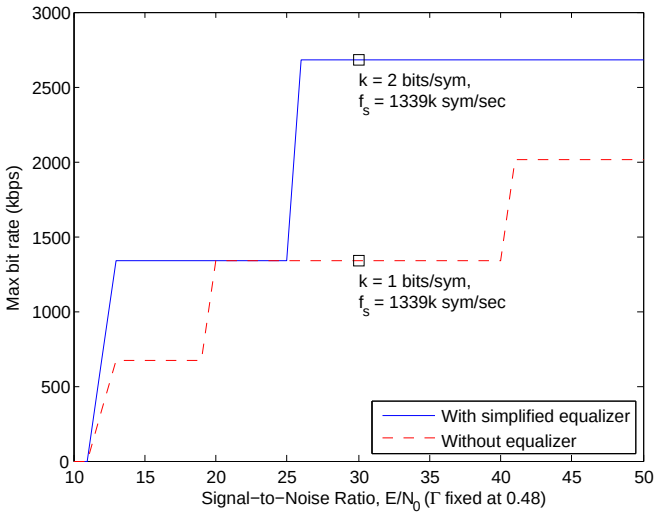

Figure 6.6: Bit rate as a function of SNR with Γ fixed at 0.48

The resulting minimum bitrate is 2.68 Mbps.

The eye diagrams in Figure 6.7 show transmission through the ultrasonic channel without equalization (Figure 6.7(a)) and with equalization (Figure 6.7(b)) for $f_s = 1339\,\text{ksym/sec}$ and $k = 2\,\text{bits/sym}$, the operating point indicated in Figure 6.6. Without equalization, 4-ary PAM communication is not possible, but using the *simplified* equalizer allow communication at 2.68 Mbps with a BER $< 10^{-5}$

6.1.2 *Improved* Echo Path Model

In Chapter 4, the echo path of the channel was modeled as the cascade of a delay element and a discrete time rational transfer function. Once this echo path model is estimated, it can be used directly to form the equalizer given in Equation 6.2. The equalizer's block diagram is shown in Figure 6.8. Note that when $\widehat{E}_l(z) = \alpha$, the equalizer of Equation 6.3 is recovered.

Based on the channel model developed in Chapter 4, the hardware implementation of this equalizer requires two components, a *delay line* if length d samples, and

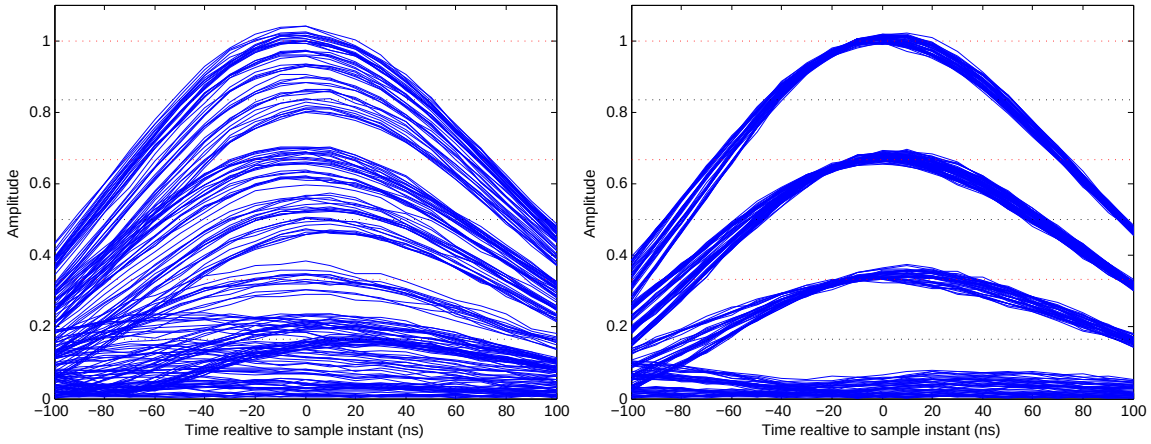

(a) Without equalization (b) With *simplified* equalizer

Figure 6.7: Eye diagrams of 4-ary PAM at $f_s = 1339$k symbols/sec

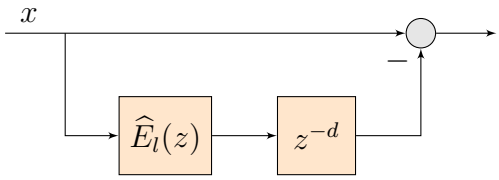

Figure 6.8: The implementation of the advanced equalizer

an IIR filter with numerator order of three and denominator order of two (see Section 4.4.4 for a discussion of model order estimation). This particular filter requires five multiply-accumulate operations per output sample. Figure 6.9 shows the effect of the *improved* equalizer when it is placed on the transmitter side of the channel. Each transmitted symbol pulse is paired with a cancelation pulse, but unlike the previous cancelation pules, this has no resemblance to the symbol pulse. This cancelation pulse, resulting from passing the symbol pulse through the improved $E(z)$, causes almost complete cancelation of echoes. What echo energy remains is below the channel's noise amplitude.

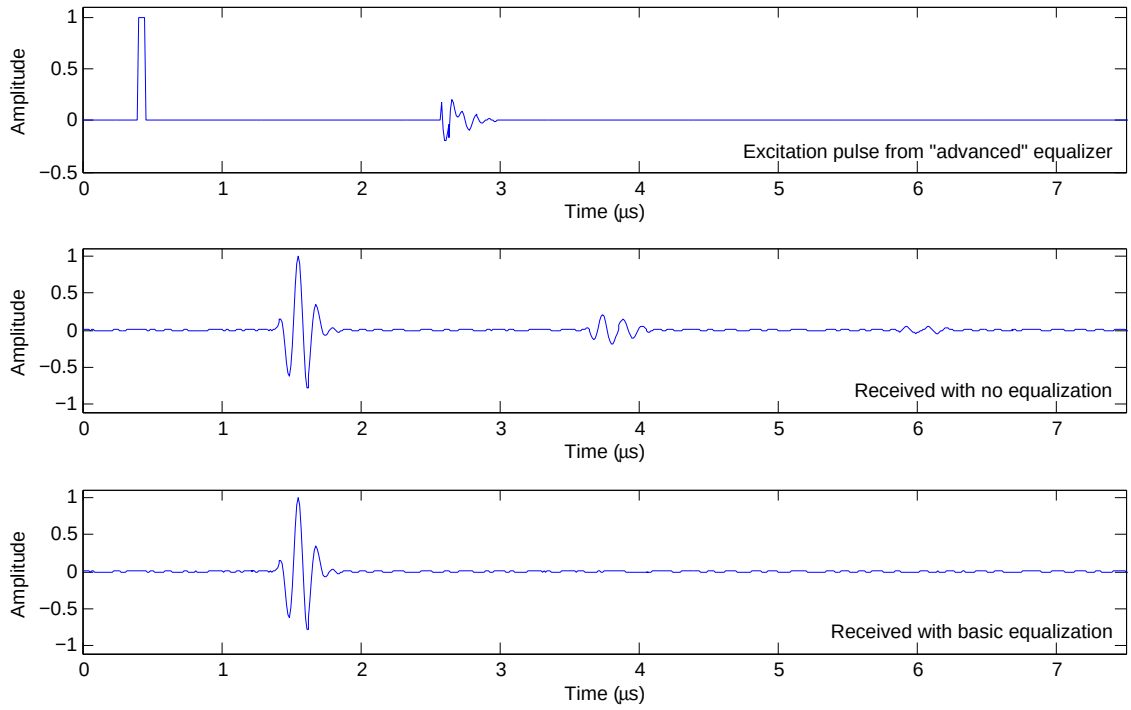

Figure 6.9: Echo suppression using equalizer derived from *improved* channel model

Achievable Data Rate The *improved* equalizer effectively eliminates all echo induced ISI, leaving only the channel's bandwidth and noise to limit the achievable data rate. In Section 5.5.1, bit error rate curves were derived for the PAM signaling scheme using several alphabet sizes. If a symbol error rate bound of BER $< 10^{-5}$ is imposed on a channel with 30 dB SNR, for example, Figure 5.12 shows that 8-PAM (3 bits/symbol) is the largest alphabet size that can be supported. If Nyquest pulses were being transmitted over the channel, the transmission symbol rate would be obvious. Since we are using the naturally occurring Gaussian response as our baseband pulse shape, however, the pulse width must be approximated. The 99% pulse width for the prototype system (i.e., the time period containing 99% of the pulse energy) is $t_{pw} = 1000\,\text{ns}$. The minimum symbol rate at which no ISI occurs is then $t_{s-min} = t_{pw}/2 = 500\,\text{ns}$. When the *improved* equalizer is used, the maximum

bit rate is

$$R = 3\,\text{bits}/500\,\text{ns} = 6.00\,\text{Mbps}. \tag{6.5}$$

Note that this rate is dependant only on the channel SNR and bandwidth, not the ISI or reflection coefficient of the channel. Figure 6.10 shows the eye diagram when transmitting 8-PAM at a 500 ns period. The *improved* equalizer provides seven-fold increase in data rate over the equalizer free transceiver and better than a three-fold increase over the *simplified* equalizer.

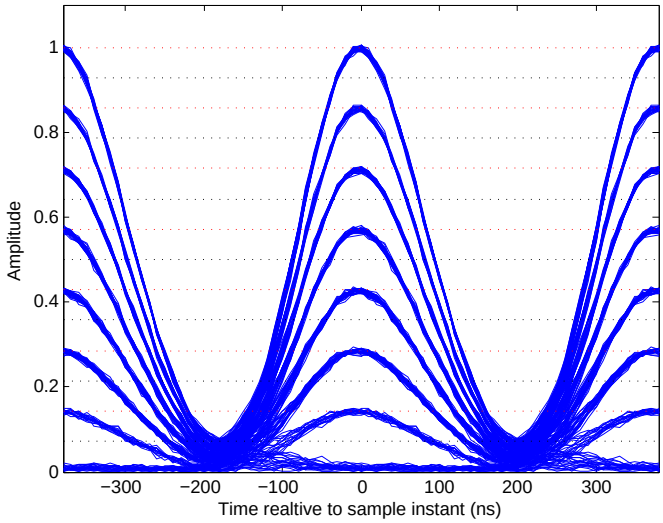

Figure 6.10: PAM eye diagram when using *improved* equalizer

6.2 Linear Equalizer

Linear equalizers are commonly used in communication systems to combat channel impairments. These equalizers are most often implemented as transversal filters. In this section, linear equalization techniques are applied to the ultrasonic communication system. First, the equalizer is applied to the PAM system developed in

Chapter 5, then extended to a bandpass QAM system. Furthermore, adaptive equalization techniques allow for automatic filter tuning and adaptation in time-varying channels.

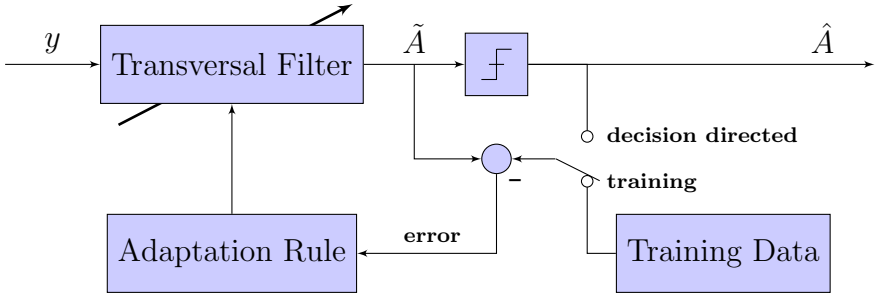

Figure 6.11: The Adaptive Linear Equalizer

Figure 6.11 shows the adaptive linear equalizer under consideration. Samples of the channel output y pass through a *transversal filter* and are presented to a *detector* that maps these (equalized) samples $\tilde{A}$ into valid symbol values $\hat{A}$. An error signal is formed by taking the difference between the signal at the output of the equalizer and the true transmitted symbol (or an estimate of it). The error signal is continually fed back and used to adjust filter coefficients according to some *adaptation rule*. The filter operates in one of two modes. In *training mode*, a known training sequence is sent through the channel, while a replica is generated within the equalizer. The error signal is formed based on the *known* transmitted sequence. The training sequence is sufficiently long to ensure that the equalizer converges. After convergence, the equalizer witches to a *decision directed mode*, where the output of the detector is assumed to be the true transmitted symbol, and this *estimate* of the transmitted

sequence is used for form the error signal. The transversal filter is described by

$$\tilde{A}[k] = \sum_{j=-K_1}^{K_2} c_j \, y_{k-j}, \tag{6.6}$$

where $\tilde{I}[k]$ is the output of the filter at time k, $\boldsymbol{c}$ are the filter's coefficients, and $\boldsymbol{v}$ are filter input samples (channel output samples) spanning $(k - K_2 \ldots k + K_1)$. The K_1 anticausal filter taps counteract precursor ISI while the K_2 causal taps counteract postcursor ISI.

6.2.1 PAM Communication

We begin by applying the linear equalizer to the PAM equivalent channel introduced in Chapter 5. Recall that the Gaussian pulse shape was used and symbols were detected incoherently at the receiver. The width of the Gaussian pulse allowed us to transmit at $t_s = 500$ ns with zero pulse overlap. Figure 6.12 shows 1000 samples at the output of the adaptive equalizer while in training mode, transmitting 2-PAM at 2 Msps. These are the same parameters used in the improved equalizer test of Section 6.1.2. The filter employs the LMS algorithm to minimize the mean-squared value of the error signal formed at the equalizer's output. The result in Figure 6.12 shows convergence after approximately 600 iterations. After convergence, the equalizer is switched to decision directed mode for continual adaptation.

Achievable Data Rate The SNR measured at the output of the filter after training is approximately 30 dB, allowing 8-PAM to be transmitted at a BER of less than 10^{-5}. The 99% pulse width of the Gaussian pulse is $t_{pw} = 1000$ ns, yielding $t_{s-min} = 500$ ns. The achievable data rate using the linear equalizer is then

$$R = 3 \, \text{bits}/500 \, \text{ns} = 6.00 \, \text{Mbps}. \tag{6.7}$$

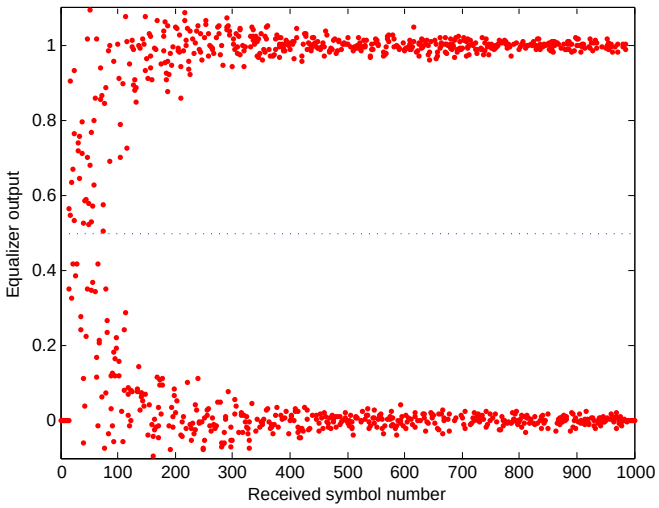

Figure 6.12: Convergence of linear adaptive PAM equalizer

which is the same rate achieved with the *improved* equalizer. Both techniques result a level of ISI suppression such that channel noise becomes the dominant factor that limits data rate.

Filter Tap Allocation When considering the computational complexity of a linear equalizer, the number of non-zero filter coefficients is of interest. The results in Figure 6.12 were produced for the equalizer in Equation 6.7 having $K_1 = K_2 = 12$. It is expected that due to the non-overlap of transmitted symbols, non-causal taps will be zero valued (corresponding to zero precursor ISI). Furthermore, due to the sparse nature of channel echoes, many of the causal taps will be zero valued as well [11]. Figure 6.13 shows the filter coefficients for the equalizer after training.

As expected, all non-causal taps are essentially zero-valued, and most causal taps are as well. The tap corresponding to c_0 is the filter's direct feedthrough path. Although the training algorithm has been performed on a 25 tap filter, substantial computational reductions can be realized by allocating taps non-uniformly. Several techniques are used in practice [11, 12, 61]. The simplest is to assign N available taps

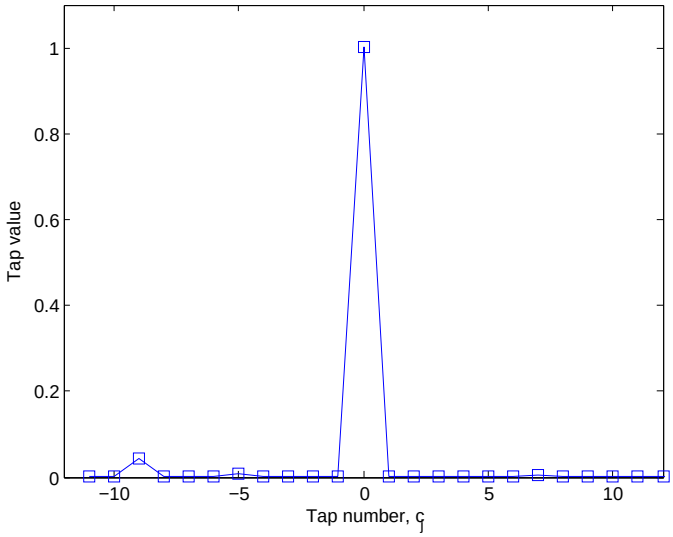

Figure 6.13: Filter tap coefficients for PAM equalizer

to the N largest coefficients. Alternatively, a threshold can be applied to the tap values and only those taps whose coefficients exceed that threshold survive. In this example, applying a normalized threshold value of 0.01 to the taps results in only three non-zero coefficients: c_0, c_{-5}, and c_{-9}. The resulting equalizer experiences an SNR degradation of less than 0.5 dB over the full 25 tap equalizer.

For the bulkhead test setup used throughout this study, the linear adaptive equalizer provides bit rate and BER comparable to that of the *improved* equalizer. Intelligent allocation of filter taps has yielded an equalizer with very low computational complexity. The complexity tradeoffs of the various equalizer methods will be discussed in greater detain in the following chapter.

6.2.2 QAM Communication

The communication techniques presented thus far have treated the communication channel as a baseband PAM channel. In reality, the resonant behavior of the transmitting transducer acts as a Gaussian pulse shaper and upconverter, and com-

munication occurs over a passband channel. Operating in this mode results in spectrally inefficient double sideband transmission. While the resulting system has low complexity, it also yields relatively low throughput. By modulating separate PAM symbol sequences on in-phase and quadrature carriers, the resulting QAM system can achieve twice the throughput of the PAM system. Furthermore, Nyquest pulse shaping can be accommodated, yielding better spectral efficiently and a further increase in throughput.

Achievable Data Rate The ultrasonic channel in our lab test setup exhibits a bandpass response with center frequency of 7.75 MHz and 3 dB bandwidth of approximately 2.9 MHz. The channel's 10 dB bandwidth is approximately 6.2 MHz. The I/Q pulse shaping is accomplished using a root raised-cosine filter (RRCF) with symbol frequency $f_s = 2.5$ MHz and rolloff factor $\beta = 0.5$. At the receiver, another RRCF functions as a matched filter, giving an overall raised-cosine (RC) response. After modulation, the bandwidth occupied by the symbols stream is

$$BW = f_s(1 + \beta) = 3.75 \text{ MHz} \tag{6.8}$$

The same adaptive filtering structure can be used with the QAM channel as was used for PAM. The only difference is that the filter tap coefficients are complex valued, and the filter processes complex valued channel samples. Figure 6.14 shows the signal constellation at the output of the adaptive filter (the predetection point $\tilde{A}$ in Figure 6.11) after convergence when transmitting 64-QAM. The achievable bit rate is 15 Mbps while maintaining a BER of 10^{-5}.

Filter Tap Allocation Just as with the PAM transceiver, we apply a threshold to the filter tap coefficients to remove those that are very near zero. The filter coefficients

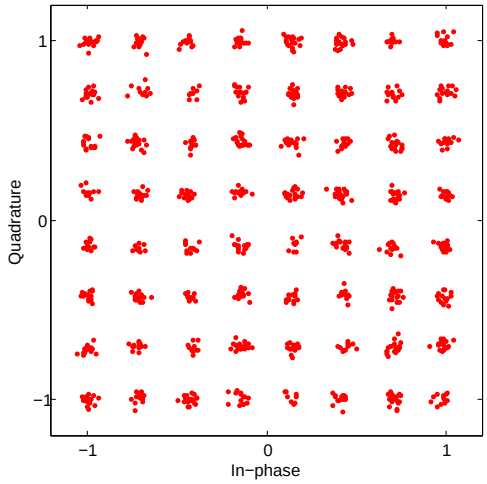

Figure 6.14: Signal constellation after convergence of QAM linear equalizer

are shown in Figure 6.15. After thresholding the tap coefficients to eliminate those whose normalized amplitude is less than 0.02, six non-zero taps remain.

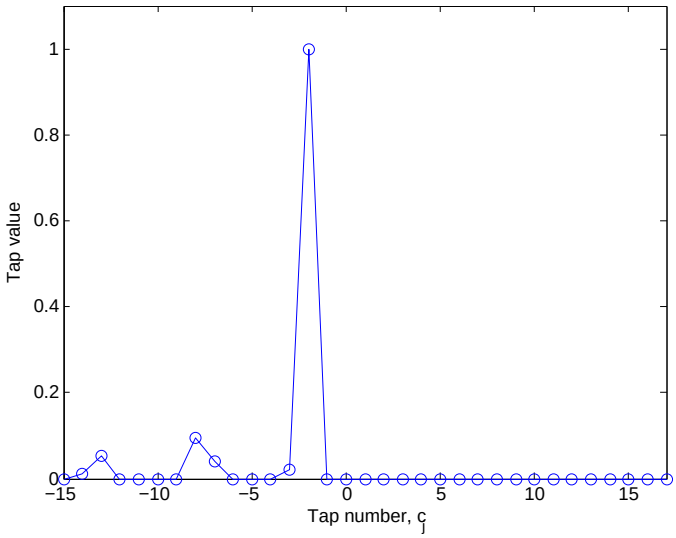

Figure 6.15: Filter tap coefficients for QAM equalizer

6.3 Orthogonal Frequency Division Multiplexing

Figure 6.16(a) shows the magnitude response of the ultrasonic channel introduced in Chapter 4, without the bulkhead in place. The bandpass characteristic is due to the frequency selective nature of the ultrasonic transducers. When the bulkhead is added to the channel, it introduces the magnitude fluctuations shown in Figure 6.16(b). Near the channel's 7.75 MHz center frequency, the magnitude response fluctuates by approximately 8 dB.

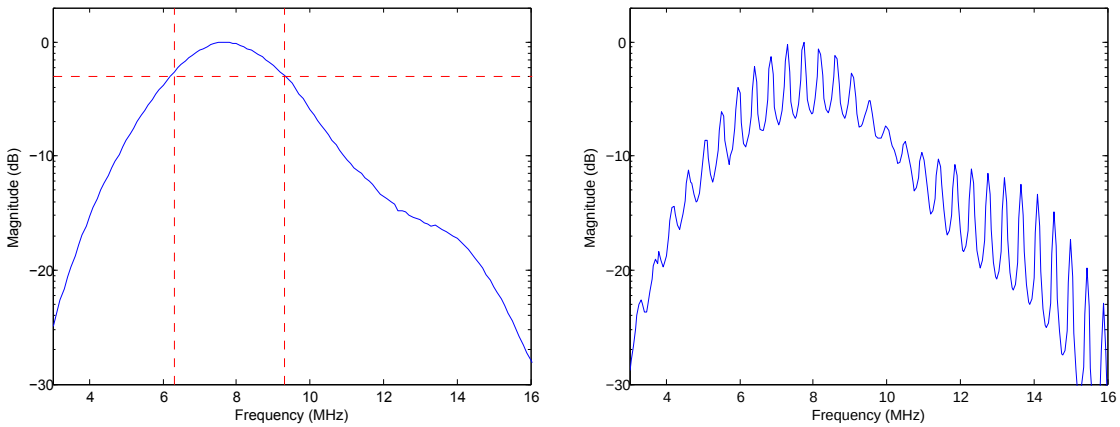

(a) Without bulkhead (b) With bulkhead

Figure 6.16: Magnitude response of the ultrasonic channels

Orthogonal Frequency Division Multiplexing (OFDM) is well suited for communication over channels exhibiting spectral nulls in the passband, such as this one. Because it divides the channel into numerous subcarriers (each occupying a small fraction of the total bandwidth), an OFDM system can assign different modulation schemes and power levels to each subcarrier to maximize total channel thoughput. A subcarrier with high SNR may be assigned 64-QAM, while one with low SNR may only be able to support 4-QAM. Furthermore, if a large number of subcarriers is

chosen, the bandwidth of each can be made small enough that the channel is approximately flat over the subcarrier's bandwidth. Under this condition, the channel equalizer reduces to a single complex multiplication per subcarrier.

In our implementation, the passband is divided into 512 subcarrieres, spanning a bandwidth of 8.33 MHz. The 60 subcarriers closest to $\pm F_s/2$ are unused (set to zero), giving 452 subcarriers, spanning a bandwidth of 7.35 MHz. A cyclic prefix of 70 symbols (8.4 μs) is included to counteract channel echoes. The OFDM transceiver operates in one of three modes: channel estimation mode, bit allocation mode, and decision directed mode.

Channel Estimation In OFDM, the (flat) magnitude and phase errors experienced by each subcarrier must be estimated and corrected for at the receiver, effectively forming a single tap equalizer for each subcarrier. Through channel estimation, the complex channel coefficient for each subcarrier is determined [62]. The techniques used most commonly in practice make use of pilot tones transmitted either (1) periodically on all subcarriers (block type estimation), or (2) continually on several dedicated subcarriers (comb type estimation) [63]. In the slowly time-varying ultrasonic channel, a simpler approach can be taken however.

Consider the symbol A_j transmitted over the j-th OFDM subcarrier. At the output of the channel, the received symbol $\tilde{A}_j$ is

$$\tilde{A}_j = c_j A_j \tag{6.9}$$

where c_j is the complex channel coefficient for that subcarrier, i.e. the scalar that describes the magnitude and phase distortion the channel imparts to that subcarrier.

If the coefficient is known, an equalizer can be formed for that subcarrier.

$$e_j = 1/c_j = A_j/\tilde{A}_j \tag{6.10}$$

Over a noiseless channel, transmitting a *single* training symbol on each subcarrier (i.e. transmitting a single OFDM data block) is sufficient to extract the channel coefficient vector. In a practical implementation, this coefficient estimation may be performed over several training blocks so that noise can be filtered. In our implementation, the channel coefficient vector is estimated iteratively over several training data blocks using

$$\mathbf{c}[n] = (1-\alpha)\mathbf{c}[n-1] + \alpha(\mathbf{A}/\tilde{\mathbf{A}}) \tag{6.11}$$

The channel coefficient vector $\mathbf{c}[n]$ at time n is a weighted sum of the past value $\mathbf{c}[n-1]$ and the current estimate $\mathbf{A}/\tilde{\mathbf{A}}$. This is an implementation of a discrete time exponentially decaying filter where α controls the filter's cutoff. Using our experimental setup, a training period consisting of forty OFDM data blocks has been used to produce a channel coefficient vector estimate.

Bit Allocation The maximum constellation size that each OFDM subcarrier can support is determined by the SNR and required bit-error rate of the subcarrier. SNR estimation of OFDM subcarriers can be performed several ways [64]. After the channel gain coefficients have been estimated and the equalizer applied to the channel, the residual error at the output of the equalizer can be attributed to channel noise. In *bit allocation* mode, a sequence of such noise samples is generated for each subcarrier, and from these, an SNR estimate can be made for each subcarrier. Figure 6.17 shows the normalized RMS noise measured on each subcarrier using the experimental setup. For subcarriers near the center of the channel's passband, where attenuation is low, RMS noise is low. At the edges of the passband, where the channel's attenuation is

high, the high gain of the channel equalizer enhances noise.

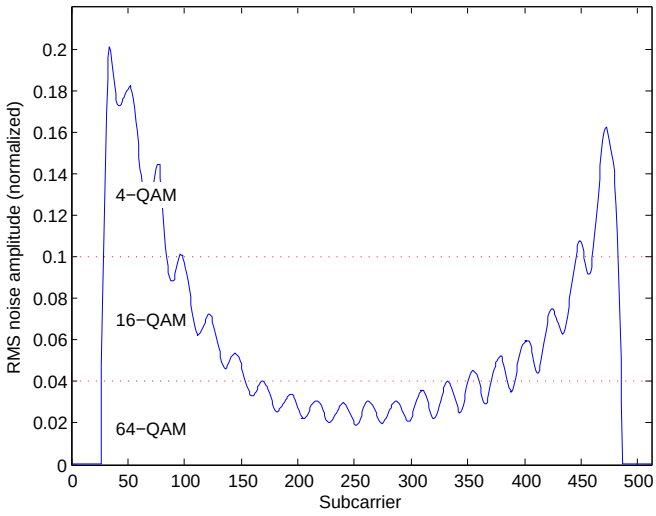

Figure 6.17: RMS noise measured on each OFDM subcarrier

The two dashed lines in the figure show the correspondence between subcarrier RMS noise, and alphabet size. These thresholds are based on a required maximum BER of 10^{-5}. In Figure 6.18, signal constellations for three representative subcarriers are shown. Subcarrier 50 (Figure 6.18(a)), with an SNR of approximately 15 dB can only support 4-QAM. Subcarrier 255 on the other hand (Figure 6.18(a)) has an SNR of 34 dB and can support 64-QAM.

Decision Directed After the channel coefficient vector is learned, the system switches to a decision directed mode so that it can adapt to slowly time varying channel conditions. In this mode, the output of the decision device is assumed to be error free, and this data replaces the known transmitted sequence that was used in training mode.

$$\mathbf{c}[n] = (1 - \alpha)\mathbf{c}[n-1] + \alpha(\hat{\mathbf{A}}/\tilde{\mathbf{A}}) \tag{6.12}$$

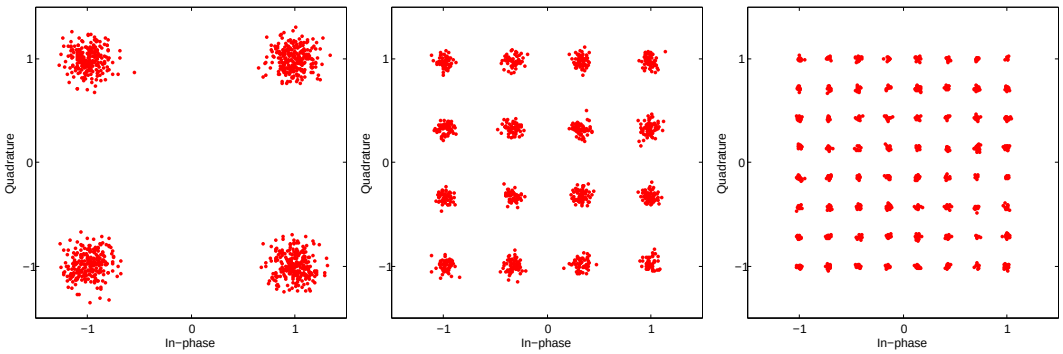

(a) Subcarrier 50, 4-QAM (b) Subcarrier 120, 16-QAM (c) Subcarrier 255, 64-QAM

Figure 6.18: OFDM subcarriers of differing constellation size

where $\hat{\mathbf{A}}$ is the estimate of the transmitted symbol appearing at the output of the detector.

Achievable Data Rate After bit allocation is completed, each OFDM subcarrier is assigned a constellation size based on its SNR. The number of bits transmitted during each OFDM frame is the sum of the bits conveyed on each subcarrier per frame,

$$b = \sum_{j=1}^{J} b_j. \tag{6.13}$$

Implemented on our laboratory test setup, and based on the RMS noise estimates shown in Figure 6.17, a block size of $b = 2098$ bits/frame was achieved. The OFDM frame transmission rate is given by

$$f = \frac{BW}{J + CP} = \frac{8.33\,\text{MHz}}{512 + 70} = 14,300\,\text{Hz} \tag{6.14}$$

where BW is the occupied bandwidth of the modulate signal, J is the number of symbols transmitted per OFDM frame (i.e. the number of subcarriers) and CP is the length of the cyclic prefix in symbols. The raw bit rate achieved by the OFDM

system is

$$R = b \cdot f = 2098 \text{ bits/frame} \cdot 14,300 \text{ frames/sec} \approx 30.0 \text{ Mbps}. \quad (6.15)$$

6.4 Summary

In this chapter, several equalizer based ultrasonic transceivers have been developed. When implemented in the laboratory, these transceivers provide data rates in the range of 2.68 Mbps to 30.0 Mbps. With this large spread in achievable data rates comes an equally large spread in transceiver complexity. In the next chapter, the hardware/software complexity of each transceiver introduced in this and the previous chapter will be discussed. With an understanding of the bandwidth-complexity tradeoffs found in each technique, practitioners can choose the transceiver design that best matches their application requirements.

7. Transceiver Hardware Implementation

In Chapters 5 and 6, several ultrasonic transceiver designs were presented, ranging widely in achievable bitrate and complexity. In this chapter, we investigate the implementation details associated with each transceiver so that the most appropriate design can be selected for a given application.

To provide a common basis for comparing the complexity of each transceiver, the same underlying hardware implementation (shown in Figure 7.1) will be assumed for each. Data enters a digital signal processor (DSP) on the transmitting side of the barrier. The data is processed and converted into a digital waveform that is then sent to a digital-to-analog converter (D/A). The analog waveform generated by the D/A passes through a reconstruction filter and a power amplifier before driving the transmitting ultrasonic transducer.

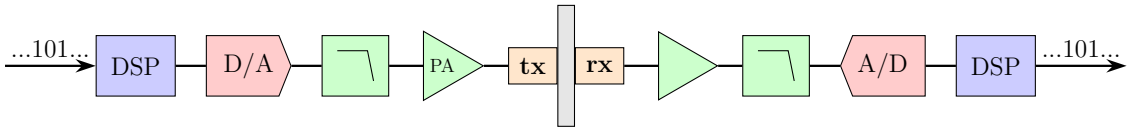

Figure 7.1: Hardware implementation common to all transceivers

Signals sensed by the receiving transducer are first amplified then filtered by an anti-aliasing filter before being digitized by an analog-to-digital converter (A/D). The digital waveform is then sent to a second DSP which recovers the transmitted data sequence and outputs it.

7.1 Transceiver complexity

Each of the transceiver designs presented in Chapters 5 and 6 will be mapped into the hardware implementation of Figure 7.1. In particular, the transcevier will be represented in a form that can be implemented on a digital signal processor or in FPGA fabric. The computational complexity of each transceiver is analyzed in terms of the number of multiply-accumulate (MAC) operations required by the transceiver per received symbol and per unit time.

When analyzing the complexity of each design alternative, we will assume that the upconversion and downconversion processes in Figure 7.2 are already implemented in the DSP. The quadrature upconversion function (Figure 7.2(a)) takes in-phase and quadrature baseband pulses (x_{Ib} and x_{Qb} respectively), upsamples them by a factor M and mixes them up to the center frequency of the channel. The upsampling operation matches the rate of incoming symbols (low megahertz range) to the D/A sample rate (tens of megahertz). The downconversion process (Figure 7.2(b)) performs the opposite function, mixing an incoming passband signal to baseband and decimating the resulting signal to a rate matching the symbol sampling rate.

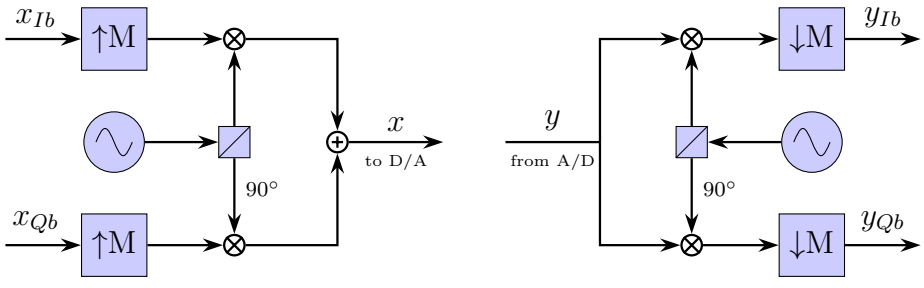

(a) Upconverter (b) Downconverter

Figure 7.2: Quadrature upconversion and downconversion processes

In the discussion the follows, we assume the following channel/transducer properties, in keeping with the laboratory test setup presented in Chapter 2.

Center frequency	7.75 MHz
3 dB bandwidth	2.75 MHz
10 dB bandwidth	6.20 MHz

7.1.1 Equalizer-free Transceivers

Figure 7.3 shows a block diagram of the equalizer-free transceiver discussed in Chapters 5. Incoming symbols enter a pulse shaper which generates amplitude modulated excitation pulses that drive the transmitting transducer. At the receiver, an envelope detector extracts the envelope of the received bandpass signal, and the detector samples this envelope at the system's symbol rate.

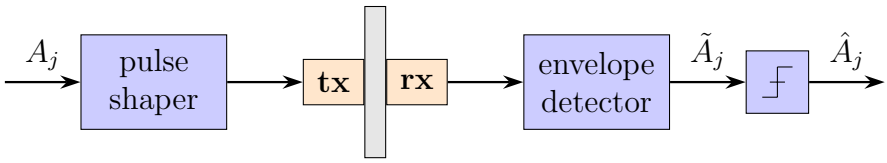

Figure 7.3: Block diagram of *Equalizer-free Transceiver*

Pulse Shaping The pulse shaper in a digital communication transmitter is generally implemented as an finite impulse response (FIR) filter. For this transceiver, however, a simpler approach can be taken. Recall that with the equalizer-free transceiver, the transmitted symbol period is much longer than the width of the pulse shaper's output pulse, i.e., neighboring transmitted pulses do not overlap. This allows us to implement the pulse shaper with a *lookup table* with N elements instead of an N tap FIR filter. For each symbol to be transmitted, the pulse generater produces

a sequence of N symbols. The length N is a function of the pulse duration and the pulse shaper's oversampling factor. Recall that the pulses generated with this transceiver are one-half cycle in length. If the pulse shaper uses a 4-to-1 oversampling factor (as we have done in this implementation), the value of N is

$$N = 2 \text{ samples/cycle} \times 0.5 \text{ cycle} \times 4\text{x oversampling} = 4 \text{ samples} \tag{7.1}$$

The maximum symbol rate supported by the equalizer-free transceiver is approximately 1.34M samples/second. This results in 5.35M samples per second at the output of the pulse generator. Modulating the amplitude of this pulse stream with the incoming symbol stream requires one multiply-accumulate per pulse shaper sample 5.35 MMACs/sec (million MACs per second) or 4 MACs per symbol .

Envelope Detector Consider the real bandpass signal $y(t)$ centered at f_c Hz with bandwidth BW Hz. Mixing the signal with an f_c Hz quadrature carrier results in a complex signal centered at DC, denoted $y_b(t)$. This signal can be expressed in either rectangular or polar form.

$$y_b(t) = y_{Ib}(t) + j\, y_{Qb}(t) = E^2(t)\, e^{j\phi(t)}$$

where $E^2(t) = |y_{Ib}(t) + j\, y_{Qb}(t)|^2 = y_{Ib}(t)^2 + y_{Qb}(t)^2$ is the *squared* envelope of the complex signal, and $\phi(t)$ is its instantaneous phase.

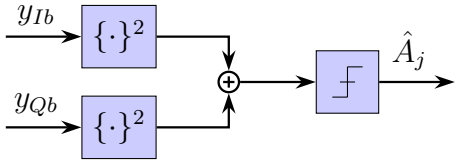

Figure 7.4: Envelope detector block diagram

Figure 7.4 shows the implementation of the envelope detector using the I and Q outputs of the quadrature downconverter (Figure 7.2(b)). The I and Q components of the signal $y_b[n]$, sampled at the transceiver's symbol rate, are squared and summed, producing $E^2[n] = x^2[n] + \hat{x}^2[n]$. Rather than calculate the square root of $E^2[n]$ and present that value to the detector, a more computationally efficient technique is to modify the detector's decision thresholds to operate on $E^2[n]$ directly, eliminating the square root operation entirely. The envelope detector requires 3 MAC operations per symbol (two squaring operations and one summation). Operating at the rate of 1.34M samples/second, the block requires 4.02 MMACs/sec.

Overall Complexity The complexity of the complete equalizer-free transceiver (pulse generator and envelope detector) is 7 MACs/symbol. When operating at the maximum supported symbol rate of 1.34M symbols/second, this equates to 9.38 MMACs/sec. With each symbol encoding 1 bit, the maximum raw bitrate is 1.34 Mbps.

7.1.2 Channel Model Based Transceivers

An implementation of the *channel model based transceiver* (presented in Chapter 6) is shown in Figure 7.5. This consists of a pulse shaper, envelope detector, and equalizing filter. The pulse shaper and envelope detector are identical to those implemented in the previous transceiver. The equalizer (not present in the previous design), consists of an FIR filter and a delay element. In this transceiver, the equalizer is derived directly from an estimated channel model. The complexity of the equalizer, therefore, is dependant on which form of the channel model: the *simplified* model or the *improved* model.

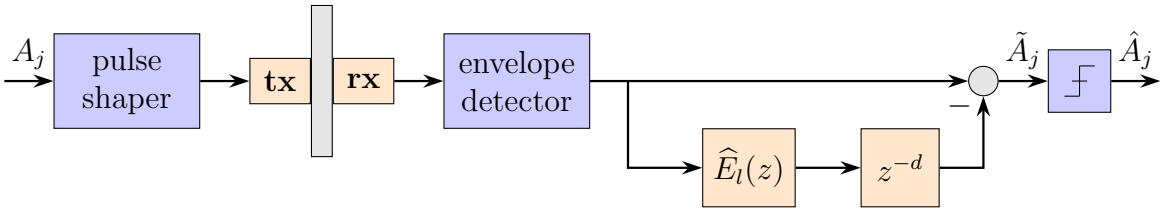

Figure 7.5: Block diagram of *Channel Model based Transceiver*

Simplified Channel Model Based Transceiver

A channel equalizer based on the *simplified* channel model was presented in Section 6.1.1. The assumption that the channel's impulse response is an exponentially decaying string of impulses lead the the following equalizer.

$$\widehat{H}_e(z) = 1 - \alpha\, z^{-r},$$

This equalizer requires exactly 1 MAC per input sample. The overall complexity of the transceiver (including the pulse shaper and envelope detector), is 8 MACs/symbol. At a symbol rate of 1.34M samples/second, this equates to 10.72 MMACs/sec. This transceiver encodes 2 bits/symbol, yielding a maximum bitrate of 2.68 Mbps.

Improved Channel Model Based Transceiver

When the improved channel model is employed in the transceiver, the equalizer takes the form

$$\begin{aligned}
\widehat{H}_e(z) &= 1 - \widehat{E}_l(z) z^{-r}, \\
\widehat{E}_l(z) &= \frac{b_E(1) + b_E(2)z^{-1} + \cdots + b_E(M_E+1)z^{-M_E}}{a_E(1) + a_E(2)z^{-1} + \cdots + a_E(N_E+1)z^{-N_E}}
\end{aligned}$$

i.e., $\widehat{E}_l(z)$ in Figure 7.5 is an infinite impulse response (IIR) filter. The number of multiply-accumulate operations needed per output from an IIR filter is equal to the combined order of the numerator and denominator ($M_E + N_E$). We have shown in Section 4.4.4 that for the ultrasonic lab setup, $M_E = 3$, $N_E = 2$. The complexity of the IIR equalization filter, therefore, is 5 MACs/symbol. The overall complexity of the transceiver (including the pulse shaper and envelope detector), is 12 MACs/symbol. The level of ISI suppression achieved with the improved transceiver allows symbol rates of 2M symbols/second to be supported. At this rate, the complexity of the improved transceiver is 24 MMACs/sec. This transceiver encodes 2 bits/symbol, yielding a maximum bitrate of 2.68 Mbps.

7.1.3 Linear Adaptive Equalizer Transceiver

Figure 7.6 shows the implementation of the linear equalizer based QAM transceiver presented in Section 6.2. Incoming complex symbols are pulse shaped using a root raised-cosine filter and upconverted to the channel's center frequency using the structure in Figure 7.2(a). At the receiver, the baseband signal is mixed down to baseband, sent through a matched filter and linear equalizer, then passed to the detector. We are interested in determining the complexity of the shaping and matched filters, and the equalizer.

Shaping and matched filters The QAM transceiver in Section 6.2 achieved a symbol rate of 2.5M symbols/sec using root raised-cosine pulse shaping. The shaping filter was implemented using an FIR structure, and spanned five symbols. Oversampling by a factor of two, this equates to a 20 tap filter. Implemented as a two path *polyphase filter* [65], this filter has a workload of 20 multiply-accumulate operations per *input* sample. The pulse shaper operates on complex symbols, requiring two identical real filters, one for the I path and one for the Q path. The overall workload of

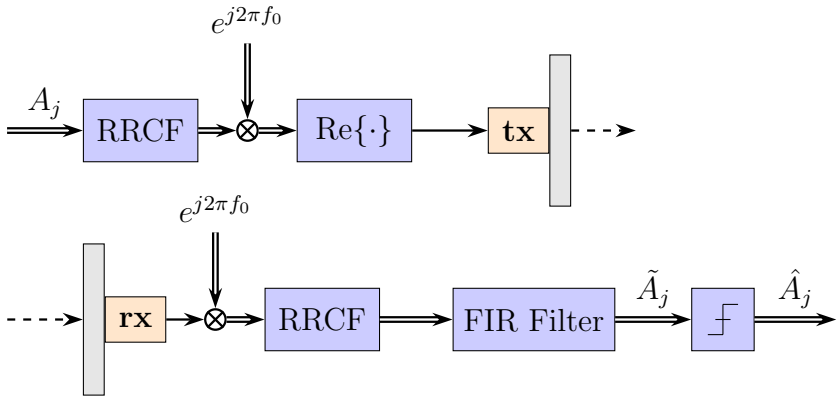

Figure 7.6: Block diagram of *Linear Equalizer based Transceiver*

the pulse shaper is then 40 MACs per input symbol. At 2.5M symbols/sec, this yields 100 MMACs/second. The matched filter at the receiver is implemented identically, requiring an additional 40 MACs per symbol.

Equalizer The equalizing filter used in the QAM transceiver started as a twenty-five tap FIR filter, After thresholding the taps to remove the negligibly small tap coefficients, only six taps remained. This results in a workload of 6 MACs per symbol, or 15M MMACs/second, for each of the I and Q paths.

Overall Complexity Between the pulse shaping filter, matched filter, and and equalizer, the linear QAM transceiver has a complexity of 92 MACs per symbol. At a symbol rate of 2.5M symbols/sec, this equates to 230M MACs/second. Encoding 6 bits/symbol (three on the in-phase carrier and three on the quadrature carrier), the achievable data rate of the QAM transceiver is 15 Mbps.

7.1.4 OFDM Transceiver

An implementation of the OFDM transceiver is shown in Figure 7.7. Incoming QAM symbols are sent onto an N-point inverse FFT, generating an N-point time

series. A cyclic prefix is concatenated with the sequence. The signal is mixed up to a carrier frequency and transmitted. At the receiver, the signal is mixed down to DC. The resulting complex baseband signal has its cyclic prefix stripped and is processed by an FFT that recovers (unequalized) transmitted symbol samples. The samples are equalized and sent to a detector, where the transmitted symbols are recovered.

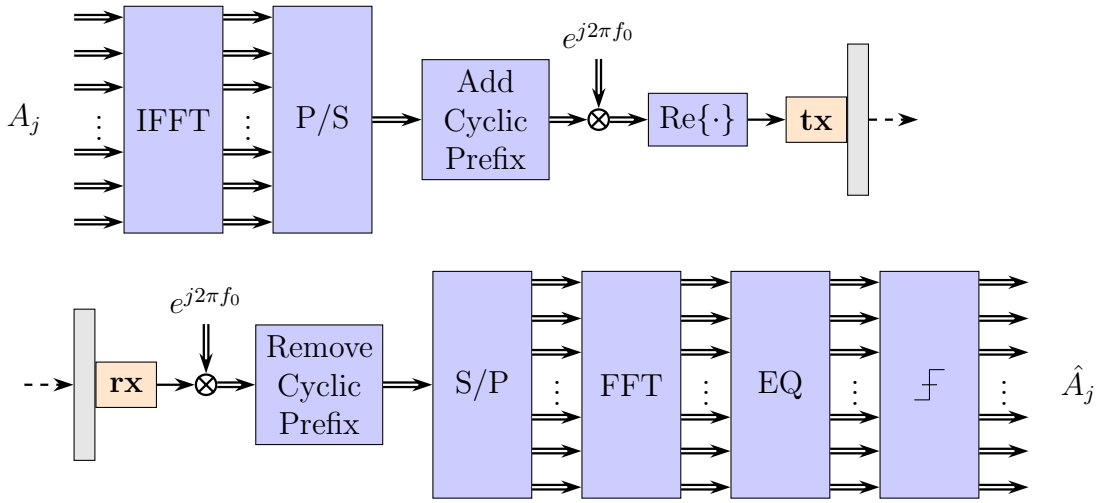

Figure 7.7: Block diagram of *OFDM Transceiver*

The complexity of the OFDM transceiver is primarily a function of the FFT blocks and the equalizer. The parallel/serial conversion and cyclic prefix addition/removal blocks contribute noting to the transceiver's complexity.

IFFT and FFT Stages The OFDM transceiver designed in Chapter 6 uses a 512-point FFT, generating 452 subcarriers. The remaining sixty subcarrier (thirty located near $F_s/2$ and thirty located at $-F_s/2$) are zero-valued to eliminate spectral content near the folding frequency. The complexity of the IFFT operation per OFDM frame is $N\log N$ multiply-accumulate operations, where $N = 512$. With each

OFDM frame transmitting 452 symbols, the complexity if the IFFT block is 4608 complex MACs/frame (9216 real MACs/frame) or 10.2 complex MACs/symbol (20.4 real MACs/symbol). The complexity of the FFT operation at the receiver is identical.

Equalizer In an OFDM transceiver, the width of each subcarrier can be made sufficiently small that the channel's magnitude and phased distortions over the subcarrier's bandwidth is approximately constant. The equalizer for that subcarrier, therefore is a scalar multiplier. The equalizer for each subcarrier then requires 452 complex MACs/frame (904 real MACs/frame) or 1 complex MACs/symbol (2 real MACs/symbol).

Overall Complexity Between IFFT, FFT, and equalizer stages, the OFDM transceiver has a complexity of 19,300 MACs/frame or 42.8 MACs/symbol. At the transceiver's maximum frame rate of 14,300 frames/sec, this equates to 276 MMACs/sec. The maximum throughput of the OFDM transceiver is 30 Mbps.

7.2 Comparison of Techniques

Table 7.1 shows a comparison of the computational requirements for each transceiver under consideration. The maximum symbol rate and the number of bits encoded per symbol are given, along with the maximum achievable bitrate. Each transceiver's complexity is reported *per symbol*, *per bit*, and *per second*. The latter value assumes that the transceiver is operating at its maximum data rate. Knowing complexity per bit allows us to compare transceivers relative to one another, while knowing complexity per second indicates the computational power needed to implement the transceiver.

The data in Table 7.1 shows that the equalizer-free transceiver requires the fewest computations per received symbol. Since the model-based transceivers can encode

Transceiver	Sym rate	Bit/sym	Bitrate	MACs/sym	MACs/bit	MMACs/sec
Equalizer-free	1.34 Msps	1 bit/sym	1.34 Mbps	7	7	9.38
Simplified model-based	1.34 Msps	2 bit/sym	2.68 Mbps	8	4	10.7
Improved model-based	2.00 Msps	3 bit/sym	6.00 Mbps	12	4	24.0
Linear equalized (QAM)	2.50 Msps	6 bit/sym	15.0 Mbps	92	15.3	230
OFDM based	6.46 Msps	4.64 bit/sym	30.0 Mbps	43	9.2	276

Table 7.1: Comparison of Transceiver Complexity

multiple bits per symbol, however, they achieve lower complexity *per bit* than the equalizer-free transceiver. Furthermore, the model-based transceivers achieve the lowest complexity per bit among all transceivers. The linear equalizer base QAM transceiver has the highest complexity of all transceivers presented. We have shown previously that its high complexity is due largely to the pulse shaping filters it uses. Finally, the OFDM transceiver exhibits a complexity per bit comparable to that of the equalizer free transceiver. Due to its greater bandwidth utilization, the OFDM transceiver offers a much higher data rate than all other transceivers.

When transmitting at data rates under approximately 6 Mbps, model based techniques appear to be the best choice as they provide low computational complexity. When high bitrates are required, the OFDM transceiver is most appropriate. Its complexity is approximately twice that of the model-based techniques, but is maximum bitrate is five times greater.

Concluding Remarks

In this thesis, we have presented techniques for achieving high bitrate communication across metallic barriers using ultrasonic signaling. A simulation model has been developed, and a procedure for tuning the model using experimental data has been presented. We have shown that this model accurately captures the echoing characteristics that make high bitrate communication in the ultrasonic channel a challenge.

Several transceiver designs have been developed and compared in terms of their computational complexity. The transceivers chosen in this study were intended to cover a wide range of data rate requirements. After comparing the computational requirements of the transceivers, we have concluded that two of these designs are particularly attractive. For low bitrate applications, model based transceivers provide a low complexity alternative. The OFDM transceiver, on the other hand, provides high data rate at the expense of greater computational complexity.

In recent years, ultrasonic through-metal communication techniques have been adapted to a variety of applications ranging greatly in bit rate requirements and power consumption constraints. This thesis provides tools to allow designers to implement the through-metal transceiver that is best matched to the requirements and constraints of their application.

Bibliography

[1] A. Seman, M. Donnelly, and S. Mastro, "Wireless systems development for distributed machinery monitoring and control," *American Society of Naval Engineers (ASNE) Intelligent Ships Symposium VII*, May 2007.

[2] C. Zacot, "Shipboard wireless sensor networks utilizing zigbee technology," Master's thesis, Naval Postgraduate School, Monterey, CA, 2006.

[3] T. Murphy, "Ultrasonic Digital Communication System for a Steel Wall Multipath Channel: Methods and Results," Master's thesis, Rensselaer Polytechnic Institute, 2006.

[4] G. J. Saulnier, H. A. Scarton, A. J. Gavens, D. A. Shoudy, T. L. Murphy, M. Wetzel, S. Bard, S. Roa-Prada, and P. Das, "P1g-4 through-wall communication of low-rate digital data using ultrasound," in *Ultrasonics Symposium, 2006. IEEE*, Oct. 2006, pp. 1385–1389.

[5] D. Shoudy, G. Saulnier, H. Scarton, P. Das, S. Roa-Prada, J. Ashdown, and A. Gavens, "P3f-5 an ultrasonic through-wall communication system with power harvesting," in *Ultrasonics Symposium, 2007. IEEE*, Oct. 2007, pp. 1848–1853.

[6] M. Kluge, T. Becker, J. Schalk, and T. Otterpohl, "Remote acoustic powering and data transmission for sensors inside of conductive envelopes," in *Sensors, 2008 IEEE*, Oct. 2008, pp. 41–44.

[7] D. Graham, J. Neasham, and B. Sharif, "High bit rate communication through metallic structures using electromagnetic acoustic transducers," in *OCEANS 2009-EUROPE, 2009. OCEANS '09.*, May 2009, pp. 1–6.

[8] P. Smalser, "Power transfer of piezoelectric generated energy," Dec. 30 1997, US Patent 5,703,474.

[9] Y. Hu, X. Zhang, J. Yang, and Q. Jiang, "Transmitting electric energy through a metal wall by acoustic waves using piezoelectric transducers," *Ultrasonics, Ferroelectrics and Frequency Control, IEEE Transactions on*, vol. 50, no. 7, pp. 773–781, July 2003.

[10] S. Sherrit, B. Doty, M. Badescu, X. Bao, Y. Bar-Cohen, J. Aldrich, and Z. Chang, "Studies of acoustic-electric feed-throughs for power transmission through structures." 2006.

[11] F. Lee and P. McLane, "Design of nonuniformly spaced tapped-delay-line equalizers for sparse multipath channels," *Communications, IEEE Transactions on*, vol. 52, no. 4, pp. 530–535, April 2004.

[12] I. Fevrier, S. Gelfand, and M. Fitz, "Reduced complexity decision feedback equalization for multipath channels with large delay spreads," *Communications, IEEE Transactions on*, vol. 47, no. 6, pp. 927–937, Jun 1999.

[13] S. Haykin, *Adaptive Filter Theory*, 4th ed. Prentice hall, 2001.

[14] T. Street, X. Nguyen, and F. Williams, "Wireless Communication Technologies on ex-USS Shadwell," *Naval Research Laboratory, Washington DC*, 2002.

[15] T. Brooks, K. B. Lee, and S. Chen, "IEEE 1451 Smart Wireless Machinery Monitoring and Control for Naval Vessels," in *Thirteenth International Ship Control Systems Symposium (SCSS)*, April 2003.

[16] "Panametrics-NDT ultrasonic transducers for nondestructive testing," *Olympus NDT*, p. 8, 2009.

[17] "Ultrasonic transducers technical notes," *Olympus NDT*, 2009.

[18] J. Proakis and M. Salehi, *Digital Communications*, 5th ed. McGraw-Hill New York, 2008.

[19] H. Seki, A. Granato, and R. Truell, "Diffraction effects in the ultrasonic field of a piston source and their importance in the accurate measurement of attenuation," *The Journal of the Acoustical Society of America*, vol. 28, no. 2, pp. 230–238, 1956.

[20] G. S. Smith, *An Introduction to Classical Electromagnetic Radiation*. Cambridge University Press, 1997.

[21] C. Dang, L. Schmerr Jr, and A. Sedov, "Modeling and measuring all the elements of an ultrasonic nondestructive evaluation system I: modeling foundations," *Research in Nondestructive Evaluation*, vol. 14, no. 3, pp. 141–176, 2002.

[22] L. Schmerr, A. Lopez-Sanchez, and R. Huang, "Complete ultrasonic transducer characterization and its use for models and measurements," *Ultrasonics*, vol. 44, pp. 753–757, 2006.

[23] W. Leach, "Controlled-source analogous circuits and SPICE models for piezoelectric transducers," *IEEE Transactions on Ultrasonics, Ferroelectrics, and Frequency Control*, vol. 41, no. 1, pp. 60–66, 1994.

[24] I. Hallaj and R. Cleveland, "FDTD simulation of finite-amplitude pressure and temperature fields for biomedical ultrasound," *JOURNAL-ACOUSTICAL SOCIETY OF AMERICA*, vol. 105, pp. 7–12, 1999.

[25] D. Kilfoyle and A. Baggeroer, "The state of the art in underwater acoustic telemetry," *IEEE Journal of Oceanic Engineering*, vol. 25, no. 1, pp. 4–27, 2000.

[26] M. Chitre, S. Shahabudeen, and M. Stojanovic, "Underwater acoustic communications and networking: Recent advances and future challenges," *The State of Technology in 2008*, vol. 42, no. 1, pp. 103–114, 2008.

[27] N. Priyantha, A. Chakraborty, and H. Balakrishnan, "The cricket location-support system," in *Proceedings of the 6th annual international conference on Mobile computing and networking*. ACM New York, NY, USA, 2000, pp. 32–43.

[28] C. Lopes and P. Aguiar, "Acoustic modems for ubiquitous computing," *Pervasive Computing, IEEE*, vol. 2, no. 3, pp. 62–71, July-Sept. 2003.

[29] R. Welle, "Ultrasonic data communication system," Nov. 9 1999, US Patent 5,982,297.

[30] ——, "Ultrasonic power sensory system," Oct. 3 2000, US Patent 6,127,942.

[31] R. Payton, "System for acoustically passing electrical signals through a hull," Sept. 23 2003, US Patent 6,625,084.

[32] Z. tao Yang, S. hua Guo, Y. tai Hu, and J. shi Yang, "Modeling of power transmission through an elastic wall by piezoelectric transducers and acoustic waves," in *Piezoelectricity, Acoustic Waves, and Device Applications, 2008. SPAWDA 2008. Symposium on*, Dec. 2008, pp. 93–97.

[33] W. Na and T. Kundu, "A combination of PZT and EMAT transducers for interface inspection," *The Journal of the Acoustical Society of America*, vol. 111, p. 2128, 2002.

[34] W. Mason, "Electromechanical transducers and wave filters," 1948.

[35] R. Krimholtz, D. Leedom, and G. Matthaei, "New equivalent circuits for elementary piezoelectric transducers," *Electronics Letters*, vol. 6, p. 398, 1970.

[36] M. Redwood, "Transient performance of a piezoelectric transducer," *The Journal of the Acoustical Society of America*, vol. 33, p. 527, 1961.

[37] S. Morris and C. Hutchens, "Implementation of mason's model on circuit analysis programs," *Ultrasonics, Ferroelectrics and Frequency Control, IEEE Transactions on*, vol. 33, no. 3, pp. 295–298, May 1986.

[38] A. Puttmer, P. Hauptmann, R. Lucklum, O. Krause, and B. Henning, "Spice model for lossy piezoceramic transducers," *Ultrasonics, Ferroelectrics and Frequency Control, IEEE Transactions on*, vol. 44, no. 1, pp. 60–66, Jan 1997.

[39] R. Cobbold, *Foundations of biomedical ultrasound*. Oxford University Press, USA, 2006.

[40] A. Arnau, *Piezoelectric transducers and applications*. Springer Verlag, 2008.

[41] J. van Deventer, T. Lofqvist, and J. Delsing, "Pspice simulation of ultrasonic systems," *Ultrasonics, Ferroelectrics and Frequency Control, IEEE Transactions on*, vol. 47, no. 4, pp. 1014–1024, Jul 2000.

[42] C. Dang, L. Schmerr Jr, and A. Sedov, "Modeling and Measuring All the Elements of an Ultrasonic Nondestructive Evaluation System II: Model-Based Measurements," *Research in Nondestructive Evaluation*, vol. 14, no. 4, pp. 177–201, 2002.

[43] L. Capineri, L. Masotti, M. Rinieri, and S. Rocchi, "Ultrasonic transducers as a black-box: equivalent circuit synthesis and matching network design," *Ultrasonics, Ferroelectrics and Frequency Control, IEEE Transactions on*, vol. 40, no. 6, pp. 694–703, Nov 1993.

[44] G. Jacovitti and G. Scarano, "Discrete time techniques for time delay estimation," *Signal Processing, IEEE Transactions on*, vol. 41, no. 2, pp. 525–533, Feb 1993.

[45] A. Grennberg and M. Sandell, "Estimation of subsample time delay differences in narrowband ultrasonic echoes using the hilbert transform correlation," *Ultrasonics, Ferroelectrics and Frequency Control, IEEE Transactions on*, vol. 41, no. 5, pp. 588–595, Sep 1994.

[46] R. Demirli and J. Saniie, "Model-based estimation of ultrasonic echoes. Part I: Analysis and algorithms," *Ultrasonics, Ferroelectrics and Frequency Control, IEEE Transactions on*, vol. 48, no. 3, pp. 787–802, May 2001.

[47] Y. Lu, R. Demirli, and J. Saniie, "3E-3 A Comparative Study of Echo Estimation Techniques for Ultrasonic NDE Applications," in *IEEE Ultrasonics Symposium, 2006*, 2006, pp. 436–439.

[48] B. Widrow, *Adaptive Filters I: Fundamentals*. Electronics Laboratories Stanford University, 1966.

[49] B. Sklar, *Digital Communications: Fundamentals and Applications*, 2nd ed. Prentice-Hall Englewood Cliffs, NJ, 2001.

[50] M. Austin, "Decision-feedback equalization for digital communication over dispersive channels." 1967.

[51] D. George, R. Bowen, and J. Storey, "An adaptive decision feedback equalizer," *Communication Technology, IEEE Transactions on*, vol. 19, no. 3, pp. 281–293, June 1971.

[52] S. Altekar and N. Beaulieu, "Upper bounds to the error probability of decision feedback equalization," *Information Theory, IEEE Transactions on*, vol. 39, no. 1, pp. 145–156, Jan 1993.

[53] R. Kumar, "Convergence of a decision-directed adaptive equalizer," in *Decision and Control, 1983. The 22nd IEEE Conference on*, vol. 22, dec. 1983, pp. 1319 –1324.

[54] R. Johnson, P. Schniter, T. Endres, J. Behm, D. Brown, and R. Casas, "Blind equalization using the constant modulus criterion: A review," *Proceedings of the IEEE*, vol. 86, no. 10, pp. 1927–1950, 1998.

[55] A. Sayed, *Fundamentals of Adaptive Filtering*. Wiley-IEEE Press, 2003.

[56] K. Yee, "Numerical solution of initial boundary value problems involving maxwell's equations in isotropic media," *Antennas and Propagation, IEEE Transactions on*, vol. 14, no. 3, pp. 302 –307, may 1966.

[57] M. Cizek and J. Rozman, "Acoustic wave equation simulation using FDTD," april 2007, pp. 1 –4.

[58] K. Steiglitz and L. McBride, "A technique for the identification of linear systems," *Automatic Control, IEEE Transactions on*, vol. 10, no. 4, pp. 461–464, Oct 1965.

[59] R. Fourer, D. M. Gay, and B. Kernighan, *AMPL: A Modeling Language for Mathematical Programming*. Duxbury Press, 2002.

[60] *Optimization Toolbox 5 Users Guide*, The MathWorks, Inc., 2010.

[61] A. Rontogiannis and K. Berberidis, "Efficient decision feedback equalization for sparse wireless channels," *Wireless Communications, IEEE Transactions on*, vol. 2, no. 3, pp. 570–581, May 2003.

[62] V. Srivastava, C. Ho, P. Fung, and S. Sun, "Robust MMSE channel estimation in OFDM systems with practical timing synchronization," in *2004 IEEE Wireless Communications and Networking Conference, 2004. WCNC*, vol. 2, 2004.

[63] S. Coleri, M. Ergen, A. Puri, and A. Bahai, "Channel estimation techniques based on pilot arrangement in OFDM systems," *IEEE Transactions on Broadcasting*, vol. 48, no. 3, pp. 223–229, 2002.

[64] H. Arslan and S. Reddy, "Noise power and SNR estimation for OFDM based wireless communication systems," in *Proc. of 3rd IASTED International Conference on Wireless and Optical Communications (WOC), Banff, Alberta, Canada*, 2003.

[65] F. J. Harris, *Multirate Signal Processing for Communication Systems*. Prentice Hall, 2004.